# Model-independent WIMP searches at the International Linear Collider

Diplomarbeit

Christoph Bartels

Institut für Experimentalphysik
Universität Hamburg

Hamburg,
Februar 2007

Gutachter: Dr. Jenny List
Prof. Dr. Peter Schleper

**Abstract**

In this diploma thesis an analysis on model-independent WIMP searches at the proposed International Linear Collider (ILC) is presented. The ILC is an $e^+e^-$ collider with a targeted centre of mass energy of 500 GeV, which will provide polarised beams. The sensitivity on a $3\sigma$ observation is investigated in WIMP pair production processes with the associated emission of initial state radiation (ISR), $e^+e^- \to \chi\chi\gamma$. Mass resolutions are given for some selected WIMP candidates. At the current stage of the analysis only statistical errors are taken into account. The basis of this study is a model-independent signal cross section derived from cosmological observations, valid across a broad range of models containing WIMPs. The formulation of the cross section allows for different couplings of the WIMPs to the initial leptons. The calculations on the sensitivity and the mass resolution are made for three different polarisation configurations, unpolarised beams ($P_{e^-} = 0.0; P_{e^+} = 0.0$), 80% electron polarisation ($P_{e^-} = 0.8; P_{e^+} = 0.0$) and additional 60% positron polarisation ($P_{e^-} = 0.8; P_{e^+} = 0.6$). A centre of mass energy of 500 GeV is assumed throughout, while the integrated luminosities $\mathcal{L}$ are set to $\mathcal{L} = 500\,\mathrm{fb}^{-1}$ for the sensitivity calculation and $\mathcal{L} = 167\,\mathrm{fb}^{-1}$ for the tests on the mass resolution. With unpolarised beams a $3\sigma$ observation should be possible for spin 1 WIMPs with masses from 90 to 225 GeV. Spin $\frac{1}{2}$ WIMPs are observable between 120 and 215 GeV. The masses can be resolved on the percentage level. Given expedient couplings and fully polarised beams, the sensitivity on a signal is increased by factors from 5 to 10, and the mass resolution enhanced significantly.

**Zusammenfassung**

In der vorliegenden Diplomarbeit wird eine modellunabhängige WIMP-Suche am geplanten International Linear Collider (ILC) vorgestellt. Der ILC ist ein $e^+e^-$ Beschleuniger mit einer angestrebten Schwerpunktsenergie von 500 GeV, der desweiteren polarisierte Elektronen und Positronen bietet. Die Sensitivität auf eine $3\sigma$-Beobachtung wird anhand des Prozesses $e^+e^- \to \chi\chi\gamma$, der WIMP Paarproduktion mit assoziierter Emission von initial state radiation (ISR) untersucht. Weiterhin werden Massenauflösungen für einige ausgewählte WIMP Kandidaten angegeben. Im derzeitigen Stand der Analyse werden nur statistische Fehler berücksichtigt. Grundlage dieser Studie ist ein auf kosmologischen Beobachtungen beruhender, und über einen grossen Bereich spezifischer Modelle gültiger, modellunabhängiger Signalwirkungsquerschnitt. Aufgrund der Modellunabhängigkeit sind die Kopplungen der WIMPs an die initialen Leptonen frei wählbar. Die Sensitivitäten und Massenauflösungen werden für drei verschiedene Polarisationseinstellungen berechnet: unpolarisierte Strahlen ($P_{e^-} = 0.0; P_{e^+} = 0.0$), 80%-ige Polarisation der Elektronen ($P_{e^-} = 0.8; P_{e^+} = 0.0$) und zusätzliche 60%-ige Positronenpolarisation ($P_{e^-} = 0.8; P_{e^+} = 0.6$). Die Schwerpunktsenergie ist durchweg auf 500 GeV angenommen, während die integrierten Luminositäten $\mathcal{L}$ auf $\mathcal{L} = 500\,\mathrm{fb}^{-1}$ in der Sensitivitätsberechnung, bzw. auf $\mathcal{L} = 167\,\mathrm{fb}^{-1}$ für die Massenauflösung gesetzt werden. Mit unpolarisierten $e^+$ und $e^-$ sollte eine $3\sigma$ Beobachtung für Spin 1 WIMPs mit Massen zwischen 90 und 225 GeV möglich sein. Für Spin $\frac{1}{2}$ WIMP erstreckt sich dieser Bereich von 120 bis 215 GeV. Die Massen können auf dem Prozentniveau aufgelöst werden. Entsprechende günstige Kopplungen vorausgesetzt kann durch maximale Polarisation der Elektronen und Positronen die Sensitivität um Faktoren zwischen 5 und 10 erhöht, und die Massenauflösung signifikant verbessert werden.

# Contents

# Chapter 1

# Introduction

Shortly after the beginning of modern cosmology with the works of Edwin Hubble on cosmological redshifts of galaxies in the late 1920's, another important cosmological observation has been made. Investigations on the dynamics of the Coma cluster of galaxies by Fritz Zwicky in the 1930's, showed that the mass to light ratio of the cluster is about 250 in solar units, making a compelling case for the existence of large quantities of non-luminous matter or Dark Matter (DM). These findings are confirmed by the measurement of rotation curves for thousands of galaxies. Early measurements of the rotation of galaxies have been conducted by Vesto Slipher in 1914, but the first accurate determination of rotation velocities at the galactic edges was made by Vera Rubin and Kent Ford in 1970. The observation is that stars in the outskirts of galaxies move much too fast around the galactic centre to be gravitationally bound to it if it were for the luminous matter alone. In recent times the analysis of the Cosmic Microwave Background (CMB) with the COBE[1] (Cosmic Background Explorer) and WMAP (Wilkinson Microwave Anisotropy Probe) space probes give the most accurate measurement of the Dark Matter density in the universe. In the $\Lambda$CDM[2] model the best fit to the CMB data requires that non-baryonic Dark Matter accounts for about 21% of the cosmological energy density. Ordinary matter contributes only 4%, while the remaining 75% are due to a mysterious energy form, so-called Dark Energy (the $\Lambda$ in $\Lambda$CDM). A particularly favoured interpretation of the Dark Matter component of the cosmological energy density is, that it consists of new heavy particles with weak interactions, so called WIMPs (Weakly Interacting Massive Particles).
The known elementary particles and their interactions are described very successfully with the Standard Model of particle physics (SM). The SM has been confirmed in many high precision measurements and its predictive power manifested for example in the prediction and subsequent discovery of the heavy gauge boson $Z^0$ with the Gargamelle experiment at CERN [1], or of the top quark at Fermilab [2]. Despite its success the SM suffers from certain shortcomings. The SM CP-violation for example is not able to explain the large matter/antimatter asymmetry observed in the universe, and the theory does not provide a WIMP candidate that could account for the measured DM energy density. The only Dark Matter candidate within the SM is the neutrino. But due to the tight limits on the neutrino masses, they can only be responsible for a small fraction of the observed DM density. Natural WIMP candidates are however found in SM extensions with new conserved quantum numbers. Such extensions are e.g. supersymmetry with conserved R-parity, resulting in the neutralino $\tilde{\chi}_1^0$ or the gravitino $\tilde{G}$ as the Lightest Supersymmetric Particle (LSP) or Kaluza-Klein-Theories with conserved KK-parity.

[1] Nobel prize in physics 2006.
[2] This model implies a non-zero cosmological constant $\Lambda$ and non-relativistic, hence cold, Dark Matter (CDM).

Several experiments and surveys are currently dedicated to the direct or indirect proof of Dark Matter, e.g. cosmological observations of weak lensing effects from DM [3], low energy recoil experiments with Ge and Si detectors (Edelweiss and CDMS [4]) and high energy searches at colliders.
In this thesis a model-independent analysis on WIMP searches at the proposed International Linear Collider (ILC) is presented. The (ILC) is planned to be the next $e^+e^-$ collider with a centre of mass energy of 500 GeV, upgradeable to 1 TeV. Furthermore the ILC provides beam polarisation of up to 80% for electrons and 60% for positrons. It is designed to measure the electro-weak sector of the SM with high precision and to be sensitive to new physics beyond the standard model, if for example supersymmetry is realised in nature. The goal of this thesis is to give limits for a discovery of WIMPs at the ILC and to determine the achievable mass resolution if a DM signal is actually found. Also addressed are the influence and possible benefits from beam polarisation on the limits and the resolution. The study is made with a full detector simulation of the Large Detector Concept (LDC) and a Particle Flow based event reconstruction. In contrast to analyses within the specific models mentioned above, a model-independent approach is taken, which will be introduced in the next chapter. In chapter 3 a technical overview of the ILC and the Large Detector Concept is given, followed by a description of the event simulation and an evaluation of the current reconstruction performance in chapter 4. In chapter 5 the obtained observation limits and mass resolutions are presented. This thesis concludes with a summary and outlook in chapter 6.

# Chapter 2

# Theoretical Context

In this chapter the cosmological observations that indicate the existence of Dark Matter are described in more detail (sec. 2.1). The next sections 2.2 and 2.3 summarise a few Dark Matter candidates and introduce the WIMP hypotheses for Dark Matter as a thermal relic of the early universe. Sections 2.4 to 2.6 focus on the model-independent approach to WIMP searches at linear colliders this analysis is based on. Finally in section 2.7 the statistical methods used in this work are presented.

## 2.1 Observational Evidence for Dark Matter

Observational evidence for Dark Matter is found in the rotation curves of galaxies, in the velocity distributions of galaxy clusters and in the Cosmic Microwave Background (CMB). These observations are addressed in this section.
Galactic rotation curves describe the track speed $v$ of stars around the galaxy as a function of their radial distance $r$ from the galactic centre. The track speeds are measured with the doppler shift of the light emitted from the moving stars. For velocities much smaller than the speed of light, $v \ll c$, the velocity component parallel to the line of sight $v_{||}$ is connected to the observed wavelength shift through

$$v_{||} = c\frac{\lambda_{\text{obs}} - \lambda_{\text{rest}}}{\lambda_{\text{rest}}}, \tag{2.1}$$

where $\lambda_{\text{rest}}$ is the wavelength in the rest frame of the light source (the star) and $\lambda_{\text{obs}}$ is the observed wavelength. If the galactic plane of a galaxy looked at is parallel to the line of sight, so that one sees it from the side, the light from the stars in it will be shifted to the blue where they are advancing or to the red where they are receding from us due to their movement around the galaxy. If the distance $d$ to the galaxy is known a star's radial distance $r$ from the centre is related to the corresponding angular distance $\theta$ through

$$r = \theta d. \tag{2.2}$$

In most galaxies the luminosity and hence the luminous mass is concentrated in a comparatively small region at the centre, the bulge. For stars with mass $m$ in the galactic outskirts at distance $r$ the galaxy can be approximated by a point mass $M$ sitting in its centre. Equating gravitational and centrifugal forces gives

$$G\frac{Mm}{r^2} = \frac{mv^2}{r} \quad \text{or} \quad v = \sqrt{\frac{GM}{r}}. \tag{2.3}$$

From this simple consideration $v \sim r^{-1/2}$ is expected. Measurements however show $v \approx const$ indicating that the Mass $M$ inside the galaxies increases proportional to the distance $r$ from the centre, $M \sim r$, even in the dim regions at the edge. This invisible mass forms a dark halo surrounding the galaxies. The radius of the dark halo of our galaxy, the Milky Way (MW), can be estimated by looking at the velocities of the small satellite galaxies of the MW such as the Magellanic clouds. The halo stretches out to at least 75 kiloparsecs. Using Eq. (2.3) with $v = 220\,\mathrm{km\,s^{-1}}$ and our galaxy's luminosity in the B band of $L_{\mathrm{MW,B}} = 2.3 \times 10^{10} L_{\odot,\mathrm{B}}$, the mass-to-light ratio of the Milky Way is estimated from this method to about

$$\left\langle \frac{M}{L} \right\rangle_{\mathrm{MW}} \approx 40 \frac{M_\odot}{L_\odot}. \tag{2.4}$$

$M_\odot$ and $L_\odot$ are the solar mass and luminosity.
Another compelling evidence for the existence of Dark Matter in the universe was found by Fritz Zwicky in the 1930's with his study of the Coma cluster of galaxies. The mass of the Coma cluster can be estimated with the use of the virial theorem applied to systems in steady state, with a constant moment of inertia $I$. In this case the theorem is [5]

$$0 = W + 2K \quad \text{with} \quad W = -\alpha \tfrac{GM^2}{r_h} \quad \text{and} \quad K = \frac{1}{2} M \left\langle v^2 \right\rangle. \tag{2.5}$$

$W$ is the potential energy of the cluster, $M$ is the total mass of all galaxies in the cluster, $r_h$ is the radius of a sphere centred on the cluster's centre of mass, containing a mass of $M/2$ and $\alpha$ is a numerical constant found to be $\approx 0.4$ for clusters. $K$ is the total kinetic energy of the galaxies in the centre of mass system with $\left\langle v^2 \right\rangle = \frac{1}{M} \sum_i m_i v_i^2$, and $v_i$ and $m_i$ being the velocities and masses of cluster galaxy $i$. Eq. (2.5) states that the kinetic energy of a self-gravitating system is $-\frac{1}{2}$ times its potential energy. With Eq. (2.5) the cluster mass can be estimated with

$$M = \frac{\left\langle v^2 \right\rangle r_h}{\alpha G}. \tag{2.6}$$

Under the assumption that the velocity dispersion of the cluster's galaxies is isotropic, the three-dimensional mean square velocity $\left\langle v^2 \right\rangle$ is three times the one-dimensional square velocity dispersion $\sigma_r^2$ along the line of sight. The velocity dispersion is found to be

$$\sigma_r = \left\langle (v_r - \left\langle v_r^2 \right\rangle) \right\rangle^{1/2} = 880\,\mathrm{km\,s^{-1}}. \tag{2.7}$$

The half mass radius $r_h$ is estimated by assuming that the mass to light ratio is constant with radius, and so $r_h$ contains half the luminosity of the cluster. The observed luminosity distribution indicates

$$r_h \approx 1.5\mathrm{Mpc}. \tag{2.8}$$

With (2.6) evaluated for the Coma cluster, its mass is estimated to $M_{\mathrm{Coma}} \approx 2 \times 10^{15} M_\odot$ in solar units. This makes the mass-to-light ratio

$$\left\langle \frac{M}{L} \right\rangle_{\mathrm{Coma}} \approx 250 \frac{M_\odot}{L_\odot}, \tag{2.9}$$

using $L_{\mathrm{Coma,B}} = 8 \times 10^{12} L_{\odot,\mathrm{B}}$ for the Coma cluster's luminosity. A third indirect method of determining the amount of Dark Matter is the analysis of the Cosmic Microwave Background (CMB). The CMB, first observed by Arno Penzias and Robert Wilson in 1965, is an isotropic radiation field from the early universe. According to the standard model of cosmology, the universe began in an extremely hot and dense phase, the Big Bang. At $t \approx 0.1$ s and temperatures of $3 \times 10^{10}$ K, almost all baryonic matter was in the form of free neutrons and protons. With the expansion of the universe the temperature dropped to $T \approx 10^9$ K at roughly $t = 300$ s. During this period the neutrons and protons fused to deuterium and helium in a process called Big Bang Nucleosynthesis (BBN). After the BBN, nearly all baryons were in the form of free protons and helium nuclei. Still, the temperature of the universe was much too high for protons and electrons to combine to electric neutral hydrogen[1]. The temperature dropped below the recombination temperature of $T_{\mathrm{rec}} = 3740$ K about 300,000 years after the Big Bang. Before that time the universe was opaque, the photons were coupled to the electrons in thermal equilibrium or said differently their rate $\Gamma$ of scattering from electrons was larger than the expansion rate $H^2$ of the universe. After that point in time the photons could travel freely through the universe, gradually cooling down with the expansion of the universe. These photons are today observed as the CMB. The spectrum of the CMB is that of an almost ideal isotropic blackbody with an equivalent temperature of 2.725 K [6]. Temperature fluctuations are with $\frac{\delta T}{T} = 1.1 \times 10^{-5}$ extremely small. These fluctuations however present an interesting possibility to learn about the early universe, since they present an image of the density fluctuations at the time of recombination. Because of the coupling between photons and electrons before recombination, hotter regions in the CMB correspond to denser regions in the universe at $t \approx 300,000$ years. The recent analysis of the angular spectrum of the fluctuations measured with high precision with the WMAP (Wilkinson Microwave Anisotropy Probe)[7] yielded the currently most accurate determination of the normalised cosmological Dark Matter energy density to $\Omega_{\mathrm{DM}} h^2 = 0.111 \pm 0.006$ [7, 8] where $\Omega_{\mathrm{DM}} = \varepsilon_{\mathrm{DM}} / \varepsilon_{\mathrm{crit}}$ is the ratio of the current Dark Matter energy density $\varepsilon_{\mathrm{DM}}$ and the critical energy density $\varepsilon_{\mathrm{crit}}$. The parameter $h$ is defined as $h = H_0/100$. With a value of $h = 0.73^{+0.03}_{-0.04}$ and the observational result that the energy density in the universe is equal to the critical energy density $\varepsilon_{\mathrm{crit}}$ it follows that about 20.8% of the energy density in the universe is due to Dark Matter, while "ordinary" baryonic matter only makes up 4% of the critical density.

## 2.2 Dark Matter Candidates

Several interpretations of the nature of Dark Matter have been given over the years since its discovery. The invisible matter component was thought to be non-luminous baryonic matter in the form of interstellar and intergalactic gases or condensed objects like planets or brown dwarfs[3]. The amount of baryonic matter is however constrained to only 4% of the cosmological energy density by the CMB and the observed amounts of light elements in primordial gas clouds together with the BBN theory. As a consequence these gases and planets can only contribute a small fraction to $\Omega_{\mathrm{DM}}$. Another intensively discussed candidate are neutrinos with a non-zero rest mass. Although the measured neutrino oscillations show that neutrinos in fact do have a non-zero rest mass [9], the constraints on $\Omega_\nu h^2 < 0.0018$ [10] give an upper limit of 3‰ on their

[1] Although misleading, this process is called "recombination".

[2] $H$ is the time dependent Hubble parameter with units of $\mathrm{km\,s^{-1}\,Mpc^{-1}}$. $H$ relates the recession speed $v$ of a distant galaxy to its distance $d$ by Hubble's law: $v = Hd$. $H_0$ denotes the parameter's today's value.

[3] Brown dwarfs are star like objects with masses slightly below the mass needed to start hydrogen fusion.

contribution to the cosmological energy density[4].
The most favoured DM candidates are new heavy particles with cross sections of approximately weak strength, so called WIMPS (Weakly Interacting Massive Particles). Due to their large masses cosmological relic WIMPS should be non-relativistic, why they are often referred to as cold Dark Matter. A very interesting feature of the WIMP hypotheses is that any extension of the standard model with new conserved quantum numbers delivers a natural WIMP candidate. A prominent SM extension is supersymmetry (SUSY) which postulates a bosonic superpartner to every SM fermion and vice versa. Because of this pairing of fermions and bosons, the superpartners have a spin difference of $\frac{1}{2}$ to their SM partners. With conserved R-parity[5] in SUSY, the Lightest Supersymmetric Particle (LSP) is a stable WIMP candidate. In the minimal extension of the SM, the so-called minimal supersymmetric standard model (MSSM), the LSP is often the neutralino $\tilde{\chi}_1^0$ or the gravitino $\tilde{G}$. The neutralino $\tilde{\chi}_1^0$ is the lightest mass eigenstate of the neutral Binos, Winos and Higgsinos ($\tilde{W}^0$, $\tilde{B}^0$, $\tilde{H}_d^0$ and $\tilde{H}_u^0$) which are the superpartners to the electro-weak gauge boson and Higgs eigenstates $W^0$, $B^0$, $H_d^0$ and $H_u^0$ [6]. Current MSSM neutralino searches give a lower limit on the mass with $m_{\tilde{\chi}_1^0} > 46$ GeV with 95% confidence [8].

## 2.3 Dark Matter as a Thermal Relic

The standard assumption for the observed DM relic density is, that the WIMPs are a thermal relic of the early universe. The argument goes as follows. It is assumed that the WIMPs were in thermal equilibrium with the SM particles after the time of baryogenesis. Annihilation of a WIMP pair into standard model particles $X$, $\chi\bar{\chi} \to X\bar{X}$ and the inverse process $X\bar{X} \to \chi\bar{\chi}$ happened with equal rates. The number density $n$ of the DM particles with mass $m_\chi$ is then governed by the Boltzmann law:

$$n \sim e^{-m_\chi/kT}. \tag{2.10}$$

Here $k$ is the Boltzmann constant. The DM particle abundance is frozen at time $t_f = 1/H_f$ when the thermal WIMP number density is $n_f$ and [11]

$$\langle \sigma v \rangle \, n_f t_f \sim 1. \tag{2.11}$$

Here $\sigma$ is the total cross section for annihilation of a pair of WIMPs into standard model particles, $v$ the relative velocity between two WIMPs in their centre of mass system and $\langle \ldots \rangle$ denotes thermal averaging. Eq. (2.11) says that the annihilation rate is equal to the expansion rate $H^{-1}$ of the universe. At $t \gg t_f$ the annihilation rate is surpassed by the expansion rate and annihilation is essentially eliminated, the WIMPs "freeze out". After freeze-out, the co-moving[7] WIMP number density remains unchanged. Their present relic density is given by [8]

$$\Omega_\chi h^2 \simeq \text{const} \frac{T_0^3}{M_{\text{Pl}}^3 \langle \sigma v \rangle} \simeq \frac{0.1\text{pb} \cdot c}{\langle \sigma v \rangle}, \tag{2.12}$$

with the current CMB equivalent temperature $T_0$ and the Planck mass $M_{\text{Pl}}$. From Eq. (2.12) one can see that the thermal averaged annihilation cross section can be derived from the observed

[4] Yet further candidates are primordial black holes. These black holes must have come into existence before the BBN era, otherwise they would contribute to $\Omega_{\text{baryon}}$.

[5] R-parity is defined by the multiplicative quantum number $P_R := (-1)^{3(B-L)+2S}$, where $B$ and $L$ are the baryon and lepton numbers, $S$ is the spin.

[6] The electro-weak eigenstates of the gauge bosons are $W^{1,2}, W^0$ and $B^0$. $W^1$ and $W^2$ combine to the mass eigenstates $W^\pm$. $Z^0$ and $\gamma$ are a composition of $W^0$ and $B^0$.

[7] Co-moving coordinates are attached to observers who are at rest relative to the CMB and the surrounding cosmic "fluid" of galaxies. These coordinates therefore expand with the universe.

relic density. Figure 2.1 shows the co-moving DM number density as a function of time for different values of the thermal averaged cross section $\langle \sigma v \rangle$. When this average increases, the remaining relic density is lowered.

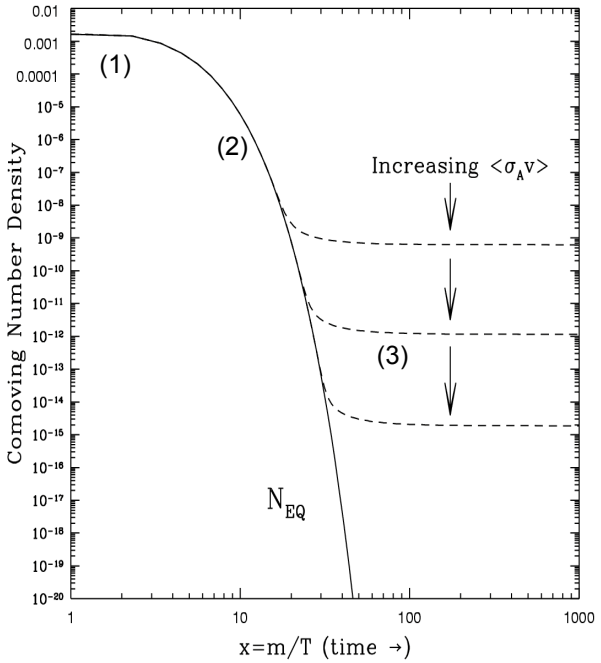


Figure 2.1: Cosmological evolution of the co-moving WIMP density. The solid line is the equilibrium abundance, the dashed lines are the abundances after freeze-out for different values of $\langle \sigma v \rangle$. From [12].

## 2.4 A Cross Section for WIMP Pair Production with Initial State Radiation

In this section a model-independent WIMP production cross section in $e^+e^-$ collisions in association with the emission of initial state radiation (ISR) is presented. The derivation of this cross section follows [13]. The predictions of the resulting production cross section are valid for any SM extension containing WIMPs, such as supersymmetry (SUSY), universal extra dimensions, little Higgs theories, etc.

For model-independence only very few assumptions on the properties of the WIMPs and their interactions are made. So it is assumed that all existing Dark Matter is due to a single new particle[8] $\chi$, kept stable by a new conserved quantum number, e.g. R-parity conservation in SUSY. A pair of these WIMP candidates can annihilate directly into Standard Model particles:

$$\chi\chi \to X_i \bar{X}_i, \tag{2.13}$$

[8] $\chi$ and $\bar{\chi}$ are considered identical in the following sections.

where $X_i = l, q, g, \nu ...$ can be any SM particle. An important restriction to the WIMP interactions is, that co-annihilation between WIMPs and other particles is explicitly excluded, for example the $\tilde{\chi}_1^0 \tilde{\tau}$ co-annihilation is not described within this model. Given these assumptions, the spin averaged WIMP pair annihilation cross section

$$\sigma_{\text{an}} = \sum_i \sigma_i, \tag{2.14}$$

is completely determined by the observed DM relic density (sec. 2.3). In Eq. (2.14) the sum extends over all annihilation processes $i$ in (2.13). Each cross section $\sigma_i$ in (2.14) can be expanded to:

$$\sigma_i v = \sum_{J=0}^{\infty} \sigma_i^{(J)} v^{2J} \quad \text{or} \quad \sigma_i = \sum_{J=0}^{\infty} \sigma_i^{(J)} v^{2J-1}, \tag{2.15}$$

where $i$ denotes the annihilation channel, $v$ is the relative velocity[9] of the colliding $\chi$'s. Here $\sigma^{(0)}$ receives a contribution from $s$-wave annihilation ($J = 0$) and $\sigma^{(1)}$ receives contributions from $s$- and $p$-wave ($J = 1$) annihilations, and so on. Since the cosmological Dark Matter is non-relativistic ($v_\chi \ll 1$), their relative velocity is obtained from the classical addition of velocities, so $v = 2v_\chi$ and $v \ll 1$. For low $v$ the lowest non-vanishing term in (2.15) characterised by the angular momentum $J_0$ will dominate. Neglecting all other terms changes Equations (2.15) to

$$\sigma_i v = \sigma_i^{(J_0)} v^{2J_0} \quad \text{and} \quad \sigma_i = \sigma_i^{(J_0)} v^{2J_0 - 1}, \tag{2.16}$$

and by inserting (2.16) in (2.14) the annihilation cross section $\sigma_{\text{an}}$ becomes

$$\sigma_{\text{an}} = \sum_i \sigma_i^{(J_0)} v^{2J_0 - 1}. \tag{2.17}$$

If the WIMP interactions are invariant under time reversal the cross sections of the processes $\chi\chi \to X_i \bar{X}_i$ are related to the cross sections of the inverse reactions by the principle of detailed balancing:

$$\frac{\sigma(\chi\chi \to X_i \bar{X}_i)}{\sigma(X_i \bar{X}_i \to \chi\chi)} = 2 \frac{v_X^2 (2S_X + 1)^2}{v_\chi^2 (2S_\chi + 1)^2}, \tag{2.18}$$

where the cross sections are averaged over spins. With $\sigma_i = \sigma(\chi\chi \to X_i \bar{X}_i)$ and considering the non-relativistic approximation $v = 2v_\chi$ in the centre of mass frame, the combination of Eq. (2.16) and (2.18) gives

$$\sigma(X_i \bar{X}_i \to \chi\chi) = 2^{2(J_0 - 1)} \kappa_i \sigma_{\text{an}} \frac{v_\chi^{2J_0 + 1}}{v_X^2} \frac{(2S_\chi + 1)^2}{(2S_X + 1)^2}, \tag{2.19}$$

introducing the spin averaged "annihilation fraction"[10] $\kappa_i = \frac{\sigma_i^{(J_0)}}{\sigma_{\text{an}}}$, that gives the fraction of WIMP pair annihilations into channel $i$. The square centre of mass energy can be expressed by

$$s = (2E_\chi)^2 = 4\gamma_\chi^2 M_\chi^2 \quad \Leftrightarrow \quad v_\chi^2 = 1 - \frac{4M_\chi^2}{s}, \tag{2.20}$$

[9] $c = 1$ in this section.
[10] Note that $\sum_i \kappa_i = 1$.

with $\gamma_\chi = (1 - v_\chi^2)^{-1/2}$. For relativistic initial state particles $X_i$ ($M_X \ll M_\chi$) their velocities hold $v_X \approx 1$, which also follows from $\gamma_X M_X = \gamma_\chi M_\chi$. Then (2.20) in (2.19) gives

$$\sigma(X_i \bar{X}_i \to \chi\chi) = 2^{2(J_0-1)} \kappa_i \sigma_{\rm an} \frac{(2S_\chi + 1)^2}{(2S_X + 1)^2} \left(1 - \frac{4M_\chi^2}{s}\right)^{1/2+J_0} . \tag{2.21}$$

Because of the weak interaction of WIMPs with ordinary matter, events described by the differential cross section (2.21) with only two $\chi$s in the final state cannot be detected in a collider experiment. The emission of an ISR photon would provide for a detectable process (Fig. 2.2). In general there is no model-independent relation between the rates of the processes $e^+e^- \to 2\chi$ and $e^+e^- \to 2\chi + \gamma$. An exception exists if the emitted photon is nearly collinear with the incoming electron or positron. In this case the differential cross section for the WIMP pair production in association with an ISR photon factorises to

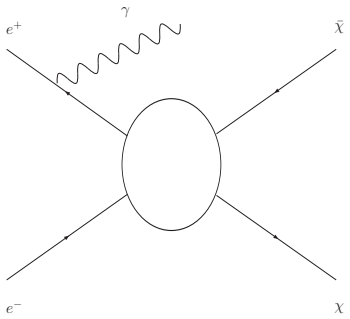


Figure 2.2: Pseudo Feynman diagram for the process $e^+e^- \to \chi\bar{\chi}\gamma$ with the emission of ISR. The ellipse expresses the model-independence of the production cross section.

$$\frac{d\sigma(e^+e^- \to 2\chi + \gamma)}{dx d\cos\Theta} \approx \mathcal{F}(x, \cos\Theta)\hat{\sigma}(e^+e^- \to 2\chi), \tag{2.22}$$

where $\Theta$ is the angle of the ISR photon with the incoming electron beam and $x = 2E_\gamma/\sqrt{s}$, with the photon energy $E_\gamma$. In Eq. (2.22) $\hat{\sigma}$ is the WIMP pair production cross section (2.21) evaluated at the reduced centre of mass energy $\hat{s} = (1 - x)s$. The universal collinear factor $\mathcal{F}$ in (2.22) is given by

$$\mathcal{F}(x, \cos\Theta) = \frac{\alpha}{\pi} \frac{1 + (1 - x)^2}{x} \frac{1}{\sin\Theta^2}. \tag{2.23}$$

The final result of [13] yields from the combination of Equations (2.21), (2.22) and (2.23) with the electron spin $S_e = \frac{1}{2}$ and the electron annihilation fraction $\kappa_e$:

$$\frac{d\sigma}{dx d\cos\Theta} \approx \frac{\alpha\kappa_e\sigma_{\rm an}}{16\pi} \frac{1 + (1 - x)^2}{x \sin\Theta^2} 2^{2J_0}(2S_\chi + 1)^2 \left(1 - \frac{4M_\chi^2}{(1 - x)s}\right)^{1/2+J_0} . \tag{2.24}$$

In this cross section the free parameters are the WIMP mass $M_\chi$, the spin $S_\chi$ and the angular momentum $J_0$ which characterises the WIMP candidate as a $s$- or $p$-annihilator ($J_0 = 0$ or 1). The cosmological constraints on $\sigma_{\rm an}$ are shown in the left plot of Fig. 2.3. The right plot is a comparison between the cross sections $d\sigma/dE_\gamma$ for the process $e^+e^- \to \chi_1^0\chi_1^0\gamma$ within the minimal supersymmetric standard model (MSSM) and this model-independent approach. The

MSSM parameters are chosen to provide the correct neutralino relic density. Explicitly the parameters take the following values at the weak scale: $M_1 = 168$ GeV, $M_2 = 2M_1$, $\tan\beta = 10$, $\mu = 225$ GeV and $m_{\tilde{l}_R} = 177$ GeV. The remaining mass parameters are fixed to 1 TeV. The plots are obtained for $\sqrt{s} = 500$ GeV, and the emitted photons have to comply with $\sin\Theta > 0.1$. Their transversal momenta are restrained to $p_{T,\gamma} > 7.5$ GeV. No cuts have been applied to eliminate central photons, because collinear emission naturally dominates the signal [13]. The compliance between both graphs is quite well, especially at the endpoint of the spectrum. At smaller photon energies the model-independent cross section is by a factor of two larger. This is due to the fact that the relative motion of the WIMPs becomes relativistic in this regime, and the non-relativistic approximations made in the derivation of Eq. (2.24) break down.

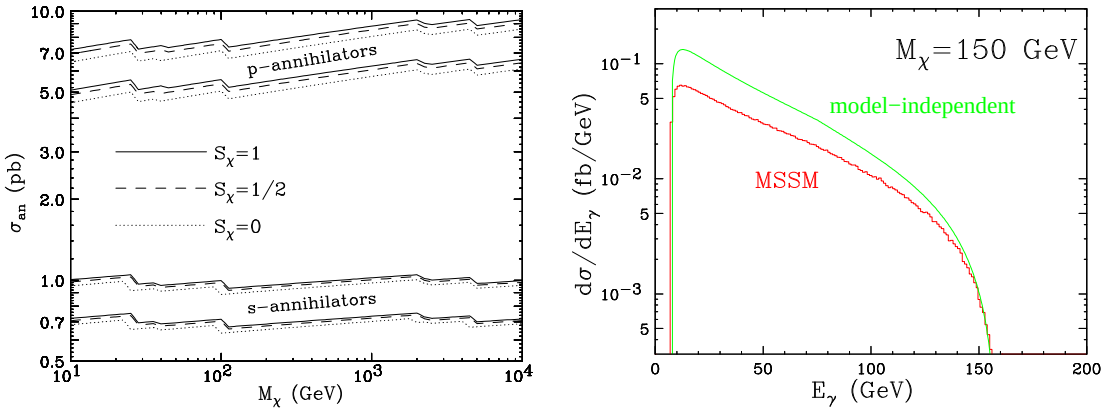


Figure 2.3: Left: Cosmological constraints on $\sigma_{\rm an}$ as a function of the WIMP mass on $2\sigma$ level. Right: Comparison between the photon spectra from the process $e^+e^- \to 2\chi_1^0\gamma$ in MSSM and from the prediction of Eq. (2.24) for a 150 GeV WIMP. Both pictures taken from [13].

## 2.5 Event Topologies

### Signal

In view of the event signature, the theoretical WIMP production cross section Eq. (2.24) of chapter 2.4 describes a fairly simple process (see Fig. 2.2). Of the three final state particles only the emitted ISR photon can be observed in an experiment, since the produced WIMPs are invisible to the detector due to their weak interaction with matter. Because of the expected large masses of the DM particles a considerable amount of energy will be missing, even in case of non-relativistic particles. The endpoint of the photon spectrum is defined by the WIMP masses through:

$$E_{\gamma,\max} = \frac{E_{\rm beam}^2 - M_\chi^2}{E_{\rm beam}}, \tag{2.25}$$

where $E_{\gamma,\max}$ is the maximum photon energy, $E_{\rm beam}$ is the energy of the electron or positron beam and $M_\chi$ is the mass of the WIMP.

## Irreducible Backgrounds

The main irreducible backgrounds are the electroweak processes $e^+e^- \to \nu\bar{\nu}\gamma$ and $e^+e^- \to \nu\bar{\nu}\nu\bar{\nu}\gamma$. Similar to the WIMPs, the neutrinos do not interact with the matter of the detector and therefore cannot be seen in a collider experiment. Figures 2.4 and 2.5 show some of the tree level Feynman diagrams contributing to these processes. The emitted photon reduces the centre of mass energy so that real instead of virtual exchange bosons can be produced. At energies well above 100 GeV the reaction $e^+e^- \to \nu\bar{\nu}\gamma$ is dominated by the $t$-channel $W$ exchange and has a rather large cross section in the range of pb [13]. Table 2.1 lists some values of the integrated cross section $\sigma$ at different centre of mass energies, together with the signal cross section $\sigma_{\text{an}}$ for 50 GeV $p$-annihilator WIMPs with spin 1 and $\kappa_e = 1$.

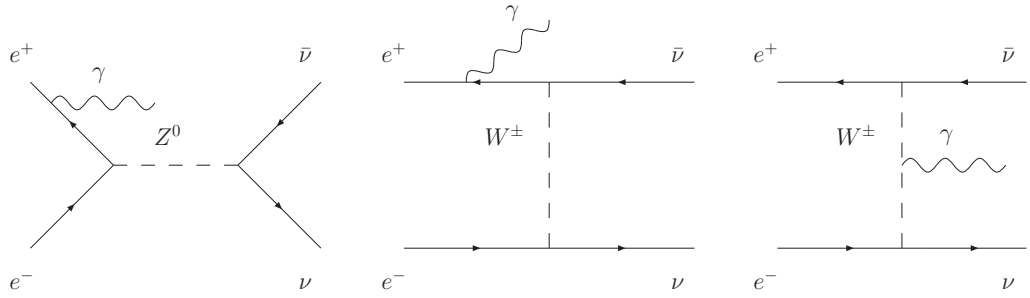


Figure 2.4: Tree level diagrams of the process $e^+e^- \to \nu\bar{\nu}\gamma$.

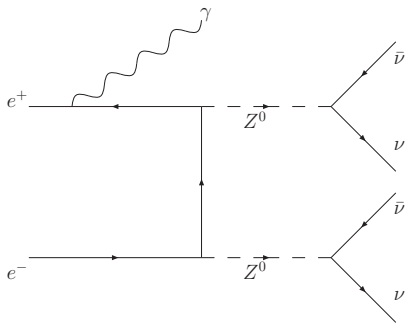


Figure 2.5: Tree level diagram of the process $e^+e^- \to \nu\bar{\nu}\nu\bar{\nu}\gamma$.

| $\sqrt{s}$ [GeV] | 50 | 75 | 100 | 125 | 150 | 200 | 500 |
|---|---|---|---|---|---|---|---|
| $\sigma$ [pb] | 0.029 | 0.163 | 38.7 | 14.82 | 7.05 | 3.44 | 2.32 |
| $\sigma_{\text{sig}}$ [pb] | 0 | 0 | 0 | 0.02 | 0.07 | 0.21 | 0.61 |

Table 2.1: Integrated cross sections for the processes $e^+e^- \to \nu\bar{\nu}\gamma$ and $e^+e^- \to \chi\chi\gamma$ at some centre of mass energies $\sqrt{s}$. The signal cross section $\sigma_{\text{sig}}$ is for 50 GeV $p$-annihilator WIMPs with spin 1 and $\kappa_e = 1$. Values of $\sigma$ calculated with `NUNUGPV` [14]. The photon's energy is constrained to 8 GeV $< E_\gamma <$ 250 GeV and its angle with the beam line has to be between 15° and 165°.

For simulation of a signal, in this analysis the $\nu\bar{\nu}\gamma$ background is weighted according to the WIMP pair production cross section, as described in sec. 5.1. The $\nu\bar{\nu}\nu\bar{\nu}\gamma$ background is not taken into account in this analysis. The matrix element $\mathcal{M}$ for this process is $\propto G_F^2$, its cross section $\propto |\mathcal{M}|^2 \sim G_F^4$ and is therefore smaller than the neutrino pair production, whose cross section is only $\propto G_F^2$.

### Reducible Backgrounds

Although there are numerous final states of $e^+e^-$ collisions, most of them can easily be excluded as background to the investigated signal process because of the simplicity of the signal signature. Any event that has other final state particles than photons is excluded from the analysis. There are however a few SM processes that can be mistaken as signal like events when not all of the reaction products are measured and identified.

The main reducible backgrounds are the SM processes

- **Electron-positron-annihilation into two photons $e^+e^- \to \gamma\gamma$:**
  This process is indistinguishable from the signal process if only one of the final state photons is detected. In the laboratory frame of the ILC which is identical to the centre of mass frame, the photons have opposite momenta and equal energies. An angular cut that ensures that both photons enter the ECAL (sec. 3.2.2) in combination with an exclusion cut on events with two photons of opposite and equal momenta reduces this background.
- **Radiative Bhabha scattering $e^+e^- \to e^+e^-\gamma$:**
  Fig. 2.6 depicts some Feynman diagrams of the first order electroweak corrections to Bhabha scattering. Two cases can cause confusion of signal and background events. At small angles with the beam-pipe one of the leptons might deposit energy in the electromagnetic calorimeter (see sec. 3.2.2), but leave no track in the tracking system and is thus interpreted as a photon. This can be prevented by imposing an angular cut on the detected photons to exclude regions not covered by the tracking system. Or, the leptons are too forward and leave the detector through the beam-pipe. These events can be rejected by a lower cut on $p_{T,\gamma} = E_\gamma \sin\Theta$ [13].
- **Radiative muon pair production $e^+e^- \to \mu^+\mu^-\gamma$:**
  This process is in first order described by the diagrams on the left of Fig. 2.6 with the outgoing electrons and positrons replaced by muons.

Due to the obvious rejection possibilities, reducible backgrounds are not considered at the current stage of analysis.

## 2.6 Beam Polarisation

The proposed ILC offers the possibility of up to 80% polarised electron and up to 60% polarised positron beams. The polarisations $P_{e^-}$ and $P_{e^+}$ are defined as:

$$P_{e^-} = \frac{I_R - I_L}{I_R + I_L} \qquad P_{e^+} = \frac{I_L - I_R}{I_R + I_L}, \tag{2.26}$$

where $I_R$ and $I_L$ are the intensities of right-handed (spin parallel to momentum $\vec{p}$) and left-handed (spin anti-parallel to $\vec{p}$) electrons or positrons. $P_{e^-} = 1$ means a 100% righthanded $e^-$

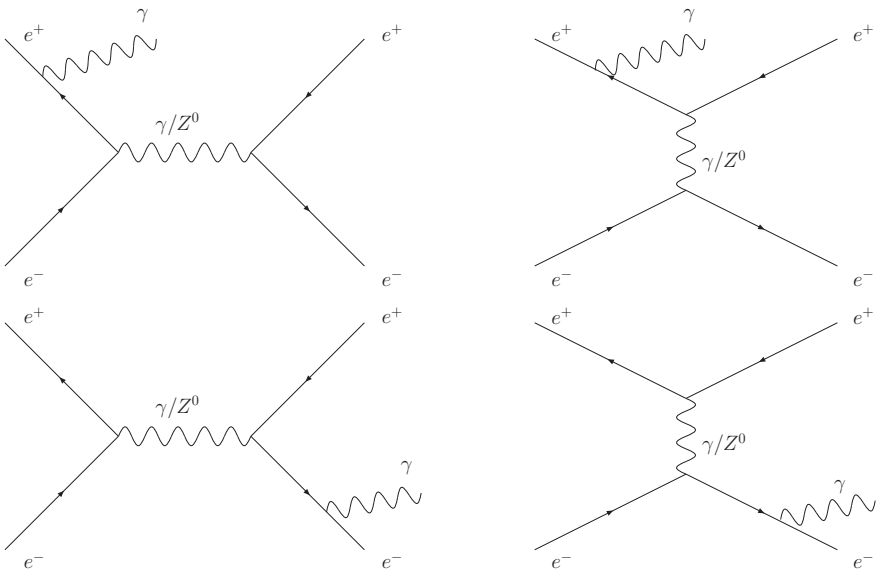


Figure 2.6: First order QED corrections to Bhabha scattering. Only diagrams that include a final state photon are shown.

polarisation and $P_{e^+} = 1$ means 100% left-handed $e^+$ polarisation. The final state neutrinos of the irreducible $e^+e^- \to \nu\bar{\nu}\gamma$ background couple only to left-handed electrons and right-handed positrons. A positive polarisation of the beams therefore reduces the number of these events. Neglecting the contribution of the $Z^0$ exchange, the cross section of the background process scales with $\kappa_{\mathrm{bg}} := (1 - P_{e^+})(1 - P_{e^-})$. The model-independent approach of section 2.4 however does not restrict the WIMPs to couple the same way to the incoming electrons and positrons as the SM neutrinos. If for example the WIMPs couple to right-handed electrons only, polarisation of the electron beam reduces the background while amplifying the signal and hence increasing the signal to background ratio.
In case of polarisation the spin averaged annihilation fraction $\kappa_e$ in equation (2.24) has to be replaced with

$$\begin{aligned}\kappa_e^{pol} = &\frac{1}{4}(1 + P_{e^-})[(1 + P_{e^+})\kappa(e_-^R e_+^L) + (1 - P_{e^+})\kappa(e_-^R e_+^R)] \\ &+\frac{1}{4}(1 - P_{e^-})[(1 + P_{e^+})\kappa(e_-^L e_+^L) + (1 - P_{e^+})\kappa(e_-^L e_+^R)]\end{aligned} \tag{2.27}$$

Here the spin dependent annihilation fraction $\kappa(e_-^R e_+^L)$ describes the strength of the WIMP couplings to right-handed electrons and left-handed positrons. The other $\kappa$'s have to be interpreted in the same manner. Note that $1/4 \sum_{i,j=R,L} \kappa(e_-^i e_+^j) = \kappa_e$. In Figure 2.7 the individual $\kappa$'s are illustrated with the relative orientations of the spins and the momenta of the incoming leptons, the SM neutrino couplings correspond to the upper left diagram.

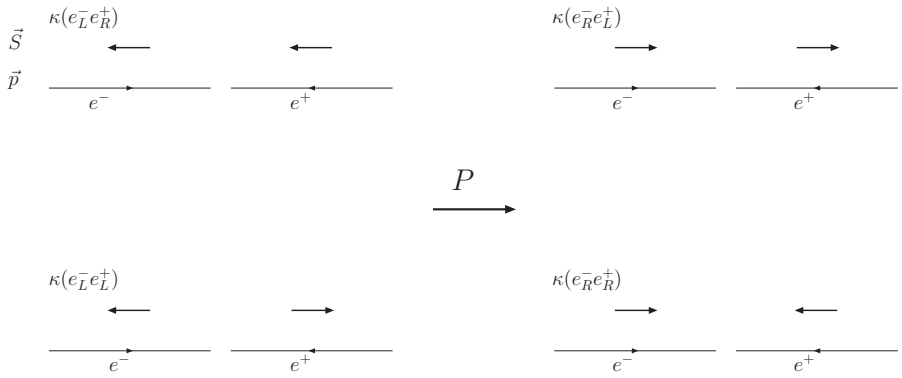


Figure 2.7: Definition of spin-dependent annihilation fractions. Top: Helicity conserving couplings. Bottom: Helicity non-conserving couplings. The figures on the right are obtained by a parity transformation $P$ on the figures on the left.

## 2.7 Statistical Methods

Two different statistical methods are used in this study to calculate limits for $3\sigma$ observations and mass resolutions. A short description of these methods is the topic of the following paragraphs.

### 2.7.1 Fractional Event Counting

The aim in a sensitivity study for a collider experiment is to decide with what statistical certainty one of the following hypotheses is true or can be excluded:

- (A) The data consists of background and signal.
- (B) The data consists of background only.

In most cases data will be available in form of histograms, ordered by some kind of discriminating variable, for example a particle mass or energy. To decide between hypothesis (A) and (B), signal and background predictions $s$ and $b$ must be available. It is assumed that these predictions exist in form of histograms, where the expected rates in histogram bin $i$ are denoted by $s_i$ and $b_i$. The predictions may be obtained from Monte Carlo studies with large statistics. The total signal rate is defined as $r = \sum_i s_i$ and the signal efficiency per bin as

$$\epsilon_i = \frac{s_i}{r}. \tag{2.28}$$

From $s_i$ and $b_i$ event weights $w_i$ are computed. With the data of an experiment a weighted sum or test statistic $X$ is calculated from the candidates observed,

$$X = \sum_l w_{i(l)}, \tag{2.29}$$

where $l$ denotes the candidate and $i(l)$ the bin the candidate belongs to. The definition of the weights is not unique, but they have to be such that $X$ is monotonically increasing from hypothesis (A) to (B). In a series of experiments the value of the test statistic $X$ would fluctuate according to a probability density function (p.d.f.) $P_b(X)$ or $P_{sb}(X)$ corresponding to the

background only and signal plus background hypotheses (Fig. 2.8). For a specific data set a statement on the probability of (A) or (B) can be given in terms of the confidence levels $CL_{sb}$ and $CL_b$:

$$CL_{sb}(W) = \int_0^W P_{sb}(X)dX, \quad CL_b(W) = \int_0^W P_b(X)dX. \tag{2.30}$$

Here $W$ is the value of $X$ evaluated for the data set. $CL_{sb}$ is the probability of a downward fluctuation of $X$ to at least $W$ if a signal exists. If a data deficit exists, $CL_{sb}$ is smaller than $1/2$, and one says that hypothesis (A) is ruled out with a probability $1 - CL_{sb}$. The confidence level $CL_b$ on the other hand, is the probability of an upward fluctuation of the background to at least $W$. The background only hypothesis is said to be excluded with probability $CL_b$.

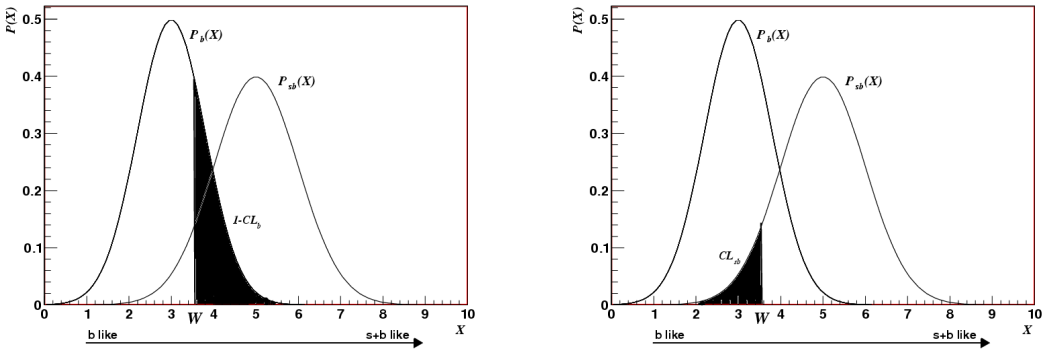


Figure 2.8: Probability density functions for a test statistic $X$. The confidence levels $CL_b$ and $CL_{sb}$ for a measurement $W$ are indicated by the filled areas.

The form of the weights $w_i$ can be optimised for optimal discrimination between the background only and the signal plus background hypotheses. Several criteria exist. These are for example:

- If the data consists of background only, one would want the mean confidence level of interpreting the data as signal and background to be low,

$$< CL_{sb} >_b = \int_0^\infty CL_{sb}(X)P_b dX, \tag{2.31}$$

  or, complementary, if the data consists of signal plus background the mean confidence level of interpreting the data as background should be high,

$$< CL_b >_{sb} = \int_0^\infty CL_b P_{sb}(X)dX. \tag{2.32}$$

  Both mean confidence levels tell how well an experiment would do on average, because a small $< CL_{sb} >_b$ means that a signal can be excluded with a high probability if the data consists of background only, while a high $< CL_b >_{sb}$ indicates that the background only hypothesis can be ruled out when a signal exists.

- One could optimise the chance to find a signal that exceeds the background prediction by a given number of standard deviations. This means minimising the probability

$$E\left[CL_{sb}\right]_b = \int_{-\infty}^{X_{cut}} P_{sb}(X)dX \tag{2.33}$$

to a cut value $X_{cut} = \sum_i w_i b_i + K\sigma_b = \langle X \rangle_b + K\sigma_b$ where $\langle X \rangle_b$ is the expectation value of $X$ for hypothesis (B) and K the wanted number of standard deviations. With $K = 0$ one maximises the chance that the total weight of signal and background events exceeds the median background level. This choice is optimal for signal detection.

In the high rate limit where the p.d.f. are gaussian, the functional form of the weights $w_i$ is found to be in all cases [15]:

$$w_i = \frac{\mathcal{R}\epsilon_i}{R\epsilon_i + b_i}, \tag{2.34}$$

where $\mathcal{R}$ is a normalisation constant that is used to adjust the maximum weight to 1, but that also could be dropped. The parameter $R$ has to be tuned to fulfil one of the optimisation criteria above. In general $R$ is proportional to the total signal rate $r$. The first criterion can be satisfied with $R = \mathcal{R} = r/2$, resulting in

$$w_i = \frac{s_i}{s_i + 2b_i}. \tag{2.35}$$

In case of small statistics an often used test statistics is the likelihood ratio

$$X = \prod_i \frac{e^{-(s_i+b_i)}(s_i+b_i)^{d_i}}{d_i!} \Big/ \frac{e^{-b_i} b_i^{d_i}}{d_i!}. \tag{2.36}$$

Here $d_i$ is the number of observed candidates in channel $i$. By taking the logarithm and neglecting constant factors, one sees that this is equivalent to a sum of weights $w_i$ defined as

$$w_i = \ln\left(1 + \frac{s_i}{b_i}\right). \tag{2.37}$$

A comparison of the power expansion in terms of $s_i/b_i$ of Eq. (2.37) and twice the expansion of (2.35) shows that both agree in the first two terms, so that they will be very similar in most cases. In addition to the mean confidence level $< CL_{sb} >_b$, the mean confidence level $< CL_b >_b$ of interpreting the data as background only from a background only source is another important figure of merit for optimising an analysis. Ideally this confidence level is 1/2. When evaluating signal exclusion limits in a single experiment, it has become convenient to give them in terms of the modified frequentist confidence level

$$CL_s = \frac{CL_{sb}}{CL_b}, \tag{2.38}$$

and exclude the existence of a signal with confidence $1 - CL_s$. This definition is useful in case of small signal rates over known background. If for example a strong downward fluctuation is observed such that even the background only hypothesis is called into question, the signal hypothesis would be excluded at high confidence although the experiment is not sensitive to it. Since $0 < CL_b < 1$, the modified frequentist confidence level $CL_s$ is always greater than $CL_{sb}$ and the resulting exclusion limits are conservative. The mean confidence level $\langle CL_s \rangle_b$ is

therefore a measure of an experiments capability to exclude small signals.
Usually $3\sigma$ observations are reported in terms of $\langle CL_b \rangle_{sb}$. In a series of experiments with data from a signal plus background source, the signal hypothesis would be accepted[11] on $3\sigma$ level if $1 - \langle CL_b \rangle_{sb} \leq 0.3$. In this analysis however $\langle CL_s \rangle_b$ as implemented in the `TLimit`-class of the **ROOT**-framework [16] was used instead. This approximation is fully acceptable in view of the other simplifications made in the analysis at its current state. The weights used by `TLimit` are the likelihood weights of Eq. (2.37).

### Calculation of Confidence Levels

After the choice of the test statistic the probability density functions and confidence levels have to be calculated. In case of poisson distributed signal plus background rates, the joint probability of finding $d_1$ candidates in bin 1, $d_2$ in bin 2 and so on is

$$P\left(\{d_1, d_2, \cdots\}\right) = \prod_{i=1}^{n} \frac{e^{-(s_i+b_i)}(s_i+b_i)^{d_i}}{d_i!}. \tag{2.39}$$

With a test statistic $W = X(\{d_i\}) = \sum_i d_i w_i$ evaluated for the observed set of candidates $\{d_i\}$, the confidence level $CL_{sb}(W)$ for excluding the possibility of simultaneous presence of signal and background is

$$CL_{sb}(W) = P(X \leq W), \tag{2.40}$$

which can be written with Eq. (2.39) as

$$P(X \leq W) = \sum_{X(\{d_{i'}\}) \leq W} \prod_{i=1}^{n} \frac{e^{-(s_i+b_i)}(s_i+b_i)^{d'_i}}{d'_i!}. \tag{2.41}$$

The sum runs over all sets of $\{d'_i\}$ with a test statistic less than or equal to the observed one. This sum can be evaluated with a Monte Carlo. Another efficient approximate method of calculating this sum is presented in [17], and is explained here.
The p.d.f. for the test statistic $X$ for a set of channels is calculated, and then iteratively combined with additional channels by convoluting with the p.d.f. of their test statistics. For a single channel the p.d.f. can be represented as a list of possible outcomes

$$(X_i^j, p_i^j). \tag{2.42}$$

$X_i^j$ is the test statistic for the $i^{th}$ channel with $j$ events, and $p_i^j$ is the poisson probability of having $j$ events in this channel if the expected rate is $(s_i + b_i)$. For two channels $i$ and $i'$ the joint outcome can be represented by

$$(X_i^j + X_{i'}^{j'}, p_i^j p_{i'}^{j'}). \tag{2.43}$$

From the list obtained by iteratively combining all channels together one can calculate the confidence level by adding up probabilities associated with test statistics less than or equal to that observed. For $n$ channels, each with $m$ different possible outcomes about $\mathcal{O}(n^m)$ terms have to be calculated and added. To limit the computation effort, a binning procedure is conducted at each combination step. First the list is sorted by the value of the test statistics. Then bins are introduced and filled with the possible outcomes of the test statistic $X$. Each bin is then

[11] More exactly: the signal hypothesis would not be rejected.

assigned a new probability by summing up the probabilities of all the outcomes in it. This way one obtains a new p.d.f. represented by a new list

$$(X_j, p_j), \tag{2.44}$$

where a representative $X$ value[12] of the $j^{th}$ bin is associated with a accumulated possibility $p_j$. This procedure is repeated iteratively until all channels are combined. Since the list is formally infinitely long at each step, it is truncated when the total probability sum of the outcomes exceeds a fixed quantity. Furthermore the choice of the binning should be linked to the probabilities; fine bins should cover small probabilities, wider bins larger probabilities. When the p.d.f. $(X_j^b, p_j^b)$ and $(X_j^{sb}, p_j^{sb})$ for the background and signal plus background hypotheses are obtained, the confidence level $CL_{sb}$ can be calculated with

$$CL_{sb} = \sum_{X_j^{sb} \leq W} p_j^{sb}, \tag{2.45}$$

where the sum extends over all list entries with $X_j^{sb}$ smaller than the observed value $W$. Also the expected confidence level $< CL_{sb} >_b$ and $< CL_s >$ can be computed with

$$< CL_{sb} >_b = \sum_{i=1}^{N_{blist}} \left[ p_i^b \sum_{X_j^{sb} \leq X_i^b} p_j^{sb} \right] \quad \text{and} \quad < CL_s >_b = \sum_{i=1}^{N_{blist}} \left[ p_i^b \frac{\sum\limits_{X_j^{sb} \leq X_i^b} p_j^{sb}}{\sum\limits_{j=1} p_j^b} \right]. \tag{2.46}$$

Here $N_{blist}$ is the number of entries in the table of the p.d.f. for the background only hypothesis. This algorithm is used in this analysis and is implemented in the **ROOT**-class `TLimit`.

### 2.7.2 Method of Least Squares

The method of least squares is used for parameter estimation, especially for the mass measurement. Given is a set of measurements $y(x_i)$ for which gaussian errors are assumed, and an assumption $y(x|\lambda)$ of the functional relation between $y$ and $x$ depending on a parameter $\lambda$. The task is to find the value of the parameter $\lambda$ for which the data is described best by the function $y(x|\lambda)$. This problem can be solved with the maximum likelihood method [18]. With the gaussian errors assumed each measurement $y(x_i)$ is distributed around the parameterised value $y(x_i|\lambda)$ according to

$$f(y(x_i)|\lambda) \sim \exp\left( -\frac{(y(x_i) - y(x_i|\lambda))^2}{2\sigma^2} \right). \tag{2.47}$$

The likelihood function is then defined as

$$L(\lambda) = \prod_i f(y(x_i|\lambda)). \tag{2.48}$$

The best choice for the parameter $\lambda$ will maximise the Likelihood function and thus its logarithm. So solving

$$\frac{d \ln L(\lambda)}{d\lambda} = 0 \;\Leftrightarrow\; \frac{d}{d\lambda}\left( -\frac{1}{2} \sum_i \frac{(y(x_i) - y(x_i|\lambda))^2}{\sigma^2} \right) = 0 \tag{2.49}$$

[12] e.g. the bin center.

delivers the best estimate $\hat{\lambda}$. Maximising $\ln L$ is equivalent to minimising the "chi squared" function $\chi^2 := \sum_i \frac{(y(x_i)-y(x_i|\lambda))^2}{\sigma^2}$. When minimising $\chi^2$, this method is called "method of least squares". Usually the boundaries for a $1\sigma$ deviation of the parameter $\lambda$ from the estimate $\hat{\lambda}$ are defined by the parameter values where $\chi^2$ deviates by one from the minimum $\chi^2_{min}$. When the likelihood is gaussian-shaped, this definition conforms to the conventional standard deviation of the gauss distribution. A modified version of this method is used to decide whether two data sets are drawn from the same underlying distribution or not, or, more precisely, whether both data sets can be consistent with a single distribution function. Both data sets are considered to exist in form of histograms with equal bin sizes and as a function of the same parameter. The number of entries in bin $i$ are denoted by $n_i$ and $m_i$, and the total of number of entries are $N = \sum_i n_i$ and $M = \sum_i m_i$ respectively. The variances in each bin are estimated with the poisson variances, so $\sigma_{n_i} = \sqrt{n_i}$. The $\chi^2$ function is then

$$\chi^2 = \sum_i \frac{(n_i - m_i)^2}{\sigma^2_{n_i} + \sigma^2_{m_i}} = \sum_i \frac{(n_i - m_i)^2}{n_i + m_i}. \tag{2.50}$$

If $M \neq N$ the histograms have to be normalised to each other:

$$\chi^2 = \sum_i \frac{(\sqrt{M/N} n_i - \sqrt{N/M} m_i)^2}{n_i + m_i}. \tag{2.51}$$

In case of weighted histograms a simple modification has to be applied [19]. Now the sum of weights in bin $i$ of histogram 1 and 2 are $w_{1,i}$ and $w_{2,i}$. Furthermore the total weights are $W_1 = \sum_i w_{1,i}$ and $W_2 = \sum_i w_{2,i}$. If both distributions are consistent one can say that there exist probabilities $p_i$ such that the expectation values in bin $i$ of histogram 1 (or 2) are given by $W_1 p_i$ (or $W_2 p_i$). The weights $w_{1,i}$ are random variables approximated with a normal distribution $\mathcal{N}(W_1 p_i; \sigma^2_{1,i})$. The maximum likelihood estimator for $p_i$ is

$$\hat{p_i} = \frac{w_{1,i} W_1 / s^2_{1,i} + w_{2,i} W_2 / s^2_{2,i}}{W_1^2 / s^2_{1,i} + W_1^2 / s^2_{1,i}}. \tag{2.52}$$

Here $s^2_{1,i}$ is the sum of squares of weights in bin $i$ that is an estimator for the variance $\sigma^2_{1,i}$. The $\chi^2$ function becomes now:

$$\chi^2 = \sum_i \frac{(w_{1,i} - W_1 \hat{p_i})^2}{s^2_{1,i}} + \sum_i \frac{(w_{2,i} - W_2 \hat{p_i})^2}{s^2_{2,i}}. = \sum_i \frac{(W_1 w_{2,i} - W_2 w_{1,i})^2}{W_1^2 s^2_{2,i} + W_2^2 s^2_{1,i}} \tag{2.53}$$

When a distribution is compared with a series of other distributions that depend on a parameter $\lambda$, the $\chi^2$ value can be plotted as a function of $\lambda$. The definitions of the best fit $\hat{\lambda}$ and its error are the same as for the parameter estimation with the method of least squares.

# Chapter 3

# The International Linear Collider

The International Linear Collider (ILC) is planned to be the next generation experiment in high energy physics. In contrast to the Large Hadron Collider (LHC) where protons collide from autumn 2007 onward, the ILC will be an $e^+e^-$ machine. In storage rings, such as the LHC, the achievable centre of mass energy is limited by the energy loss of the charged particles due to synchrotron radiation. The loss $\Delta E$ per circulation is

$$\Delta E \sim \left(\frac{E_0}{m_0 c^2}\right)^4 \frac{1}{R}, \tag{3.1}$$

where $E_0$ and $m_0$ are the particle's energy and rest mass and $R$ is the radius of the storage ring. For electrons the radiation loss in a storage ring with radius $R_0$ is about $10^{13}$ times higher than for protons at the same energy. Therefore the ILC will be a linear collider, which does not suffer from this problem. In linear colliders, the centre of mass energy is eventually limited by the length of the acceleration line and the gradients of the cavities. The ILC is designed for reaching centre of mass energies of 500 GeV, about one order of magnitude lower than the 14 TeV of the LHC[1]. However without the strong QCD background that the LHC has to deal with, the ILC allows high precision measurements of the electro-weak physics sector, and so the ILC will be complementary to the LHC, hopefully giving insight to new physics beyond the standard model (BSM). As a linear collider the ILC consists of two linac arms aligned face-to-face and each about 11.4 km in length (see Fig. 3.1). Electrons and positrons are accelerated in these linacs and led to two interaction regions in the middle of the accelerator where the reaction products are collected with two detectors.

## 3.1 The Accelerator

The baseline layout of the main linac is shown in Fig. 3.1 [20]. Polarised electrons are created by illuminating a GaAs/GaAsP gas cathode with a Ti:Sapphire drive laser. The electrons from this source are accelerated and injected at 5 GeV into the $e^-$ damping ring (DR), to reduce beam emittance. Emittance reduction is achieved by radiation damping, i.e. alternating the emission of synchrotron radiation in bending fields and acceleration in RF cavities [21]. The damping rings circumference is approximately 6.7 km. After leaving the damping ring, the electrons are transported to the low energy side of the electron linac, in which they are accelerated to 250 GeV. One possibility for positron production is an undulator based source. At electron energies

[1] In the $pp$ collisions at the LHC only the $qq$ or $gg$ centre of mass energy is effectively available.

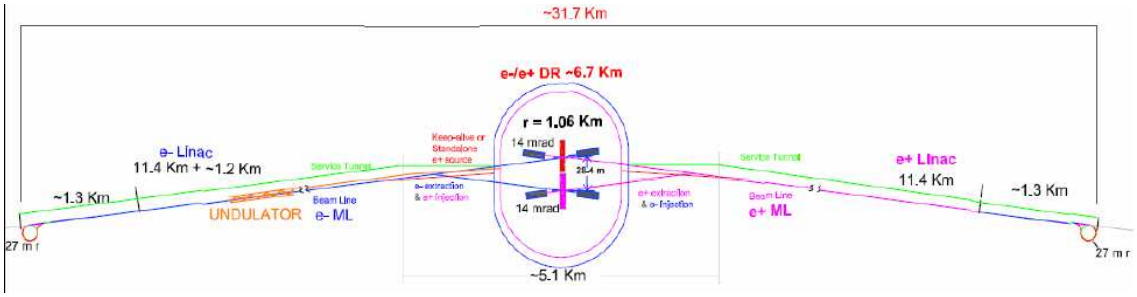


Figure 3.1: ILC baseline layout.

of about 150 GeV the electrons pass a 100 m long helical undulator, which provides circularly polarised photons. These photons produce electron positron pairs in an Ti-alloy target. The polarised positrons from this process are collected and put in the positron damping ring, and after that injected into the main linac. On average 1.5 positrons per electron are produced.
The electron and positron sources are designed for beam polarisations of $P_{e^-} = 80\%$ for the electron and $P_{e^+} = 60\%$ for the positron beam.
For threshold scans, the overall design allows for the centre of mass energy $E_{\mathrm{CM}}$ to be tuned from 90 to 500 GeV, or even up to $E_{\mathrm{CM}} = 1$ TeV if the option of an energy upgrade is made use of after the first years of running. Table 3.1 lists the parameter bounds as stated in [20]. Within these bounds five reference points are defined:

- **Nominal set:** Serves as reference to the other sets.
- **Low bunch charge:** Reduction in bunch charge by a factor of two.
- **Large $\sigma_y^*$:** Increased vertical beam size.
- **Low Power:** Reduced number of bunches $n_b$ by a factor of two.
- **High Luminosity:** smaller IP beam size and shorter bunches.

The first four sets give a luminosity of $L = 2 \times 10^{34}\mathrm{cm}^{-2}\mathrm{s}^{-1}$, while the high luminosity option has $L = 5 \times 10^{34}\mathrm{cm}^{-2}\mathrm{s}^{-1}$.
The interaction between the highly collimated high energy electron and positron bunches leads to two coupled effects, disruption and "beam strahlung" [22]. The leptons from one bunch (electron or positron) see the electromagnetic field from the collected charge of the oncoming bunches. The disruption effect is associated with the bending of the trajectory of the particle under the influence of this electromagnetic field and the beam strahlung effect is associated with the radiation loss of the particle energies induced by the bending of the trajectory. Typical disruption angles at the ILC will be in the order of 10 mrad. The beam strahlung photons are very collinear and have predominantly small energies at the MeV scale. These effects are not taken into account in this study.

## 3.2 The Detector

There are currently four detector designs in development. The SiD (Silicon Detector) uses a silicon tracker, while the other three layouts, GLD (Global Large Detector), LDC (Large Detector Concept) and the $4^{th}$ concept gather the tracking information with a TPC (Time

| parameter | | minimal | nominal | maximal | |
|---|---|---|---|---|---|
| Bunch charge | N | 1 | 2 | 2 | $\times 10^{10}$ |
| Number of bunches | $n_b$ | 1330 | 2820 | 5640 | |
| Linac bunch interval | $t_b$ | 154 | 308 | 461 | ns |
| Bunch length | $\sigma_z$ | 150 | 300 | 500 | $\mu$m |
| Beam size at IP | $(\sigma_x^*;\sigma_y^*)$ | | (553;5) | | nm |

Table 3.1: ILC baseline parameters.

Projection Chamber). Further differences between the four concepts comprise the strength of the magnetic field and the calorimeter technology. The detector model LDC01Sc of the LDC layout, which is simulated for this analysis, will be described in short in the next paragraphs. The depiction will focus on the tracking and calorimetric systems. A three dimensional sketch of the LDC can be seen in Figure 3.2.

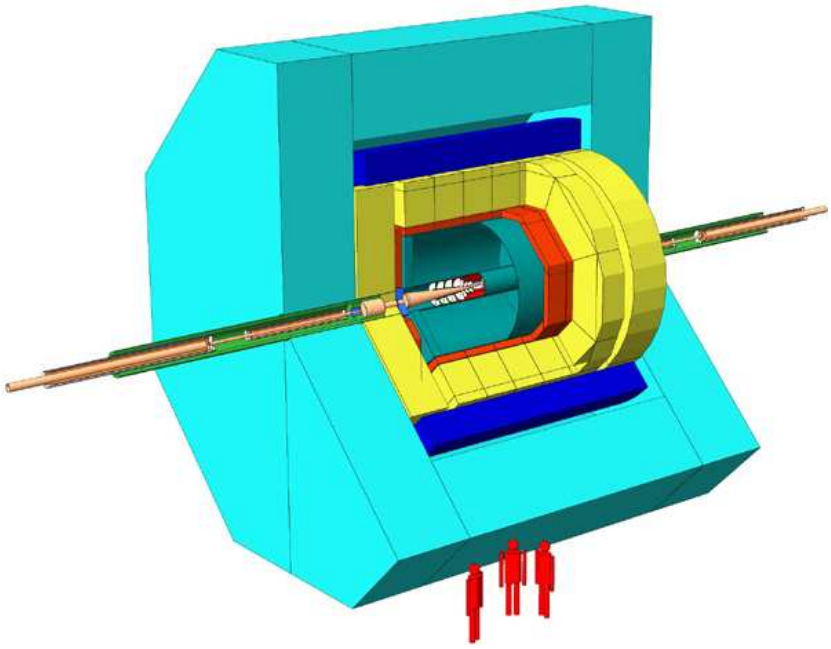

Figure 3.2: Three dimensional drawing of the Large Detector Concept

The detector design is optimised to make reconstruction of every particle in an event, both charged and neutral, possible [23]. For this kind of full event reconstruction spatial separation of particles is more important than the precise measurement of the particles' parameters. This need is especially reflected in the design of the calorimetric systems where the spatial resolution is achieved with a very high granularity.
The LDC01Sc detector consists of the following subsystems [23] (see Fig. 3.3 and 3.4):

- a pixel vertex detector (VTX) as the innermost subsystem around the interaction point (IP).
- a system of silicon strips (SIT) bridging the gap between the VTX and the TPC. In

the forward direction pixilated silicon discs (FTD) extend the tracking coverage to small angles.

- a large gas filled time projection chamber (TPC), the main tracking device.
- a Si-W electromagnetic calorimeter (ECAL) with cell sizes of $5 \times 5$ mm$^2$.
- a Fe-scintillator hadronic calorimeter (HCAL) with cell sizes of $3 \times 3$ cm$^2$.
- a large volume superconducting coil designed for creating a longitudinal B-field of 4 Tesla.
- an iron yoke, returning the magnetic flux. It also serves as a muon detector through the instrumentation with a number of layers of tracking detectors.

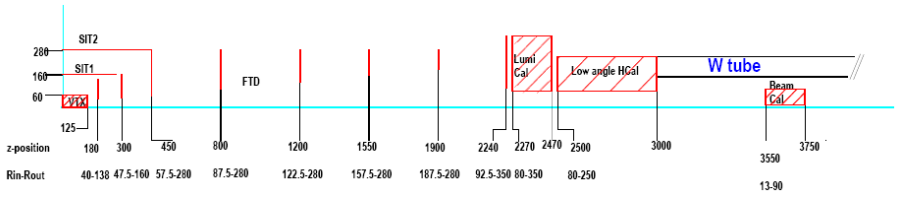


Figure 3.3: Schematic drawing of the innermost detector region. Distances are given in millimetres.

### 3.2.1 The Tracking System

The main component of the tracking system is the TPC. The TPC is a large gas[2] filled cylindrical volume immersed in the magnetic field of the superconducting coil. Charged particles entering the TPC follow a curved path due to the B-field and ionise the gas along their trail. An electric field applied to the TPC endplates accelerates the primary electrons towards the endplates. In front of the TPC endplates the signal is amplified by GEMs (Gas Electron Multipliers) or Micromegas and the charge is then collected on pads mounted on the endplates. In combination with the timing information which is precise to 2 ns, the tracks of the charged particles can be reconstructed from the collected charges. The momentum resolution aimed at in the TPC is $\delta(1/p_t) \approx 10^{-4}/(\mathrm{GeV/c})$. The combined tracking system of TPC, VTX and SIT provides track reconstruction down to polar angles of $\cos\Theta = 0.91$ ($\Theta = 24°$). This angular region is fully covered by all 5 VTX layers and both of the SIT layers (Fig. 3.5). For smaller angles with $0.97 < \cos\Theta < 0.993$ ($6.8° < \Theta < 14°$) tracks are only reconstructed in the FTD (Forward Track Detector). The intermediate region is partially covered by each of these detectors. The track reconstruction efficiency of the full system is better than 99% for polar angles with $\cos\Theta < 0.9$, decreasing to 92% at $\cos\Theta = 0.95$ where track reconstruction becomes dependent on pattern recognition in the FTD. The TPC alone provides track reconstruction efficiencies of 98% down to angles given by $\cos\Theta = 0.91$.

### 3.2.2 The Calorimeter System

The calorimetric system of the LDC is fully dispersed in the coil and has an electromagnetic (ECAL) and a hadronic (HCAL) component. Electromagnetic particles, electrons and photons

[2]Several gas mixtures are under investigation, e.g. Ar(93%)$CH_4$(5%)$CO_2$(2%), so-called "TDR"gas.

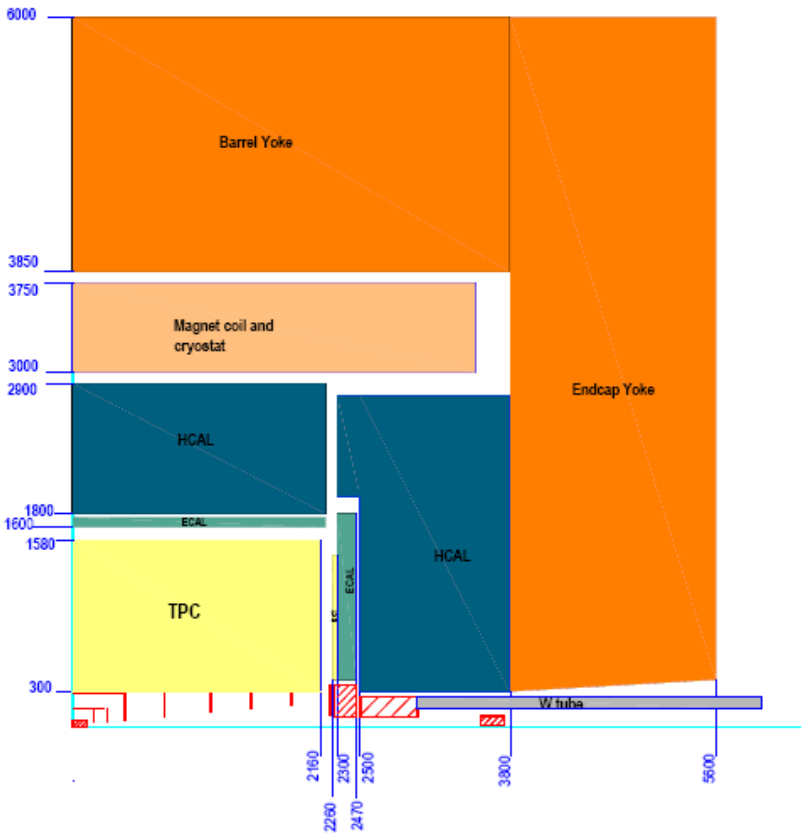


Figure 3.4: Schematic drawing of the LDC01Sc detector. Distances are given in millimetres.

are detected in the ECAL, hadronic showers are measured in the HCAL. A schematic drawing of the calorimetric system is given in Fig. 3.6.

**ECAL**

The ECAL is optimised for the measurement of photons and electrons, and for the separation of photon showers from hadronic showers. Following the cylindrical symmetry imposed by the beams, the ECAL has as an approximation an octagonal shape. It is divided up into a barrel region around the IP and two endcaps. Including endcaps the ECAL covers polar angles with $|\cos\Theta| < 0.99$. Because of the large ratio of interaction to radiation lengths tungsten has been chosen for the absorbing material. The choice for the active detector are silicon diodes. Absorber and active material are arranged in alternating layers of tungsten plates and silicon strip detectors with a very fine segmentation of $5 \times 5$ mm$^2$. In the current design of the LDC01 model the inner 20 absorber layers have a thickness of 2.1 mm followed by 10 layers with 4.2 mm, while the LDC00 consists of 30 layers with 1.4 mm and 10 layers with 4.2 mm. Fig. 3.7(a) shows the fractional energy resolution for both the models LDC01 and LDC00. The results are based on simulated photons with $\Theta = \pi/2$, using the GEANT 4.8.0 [24] and Mokka 5.5 [25] software. In case of the LDC01 an energy resolution of $14.4\%/\sqrt{E(GeV)} + 0.5\%$ is observed. The raw detector response (i.e. the sum of the deposited energy) as a function of the polar angle

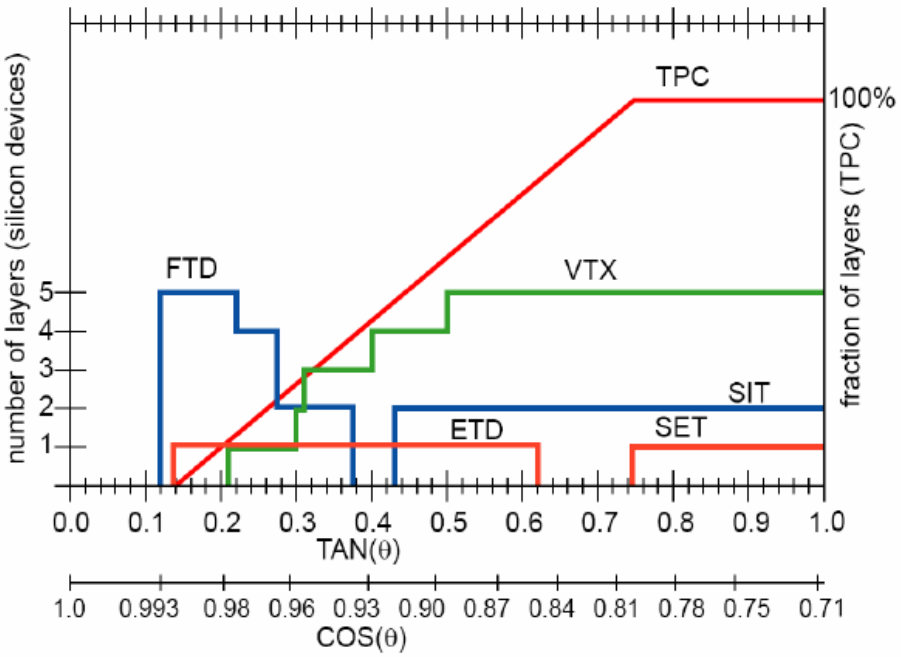


Figure 3.5: The acceptance of the tracker subsystem as function of the polar angle $\Theta$. The acceptance is given in terms of the number of effective layers, or in case of the TPC, as the fraction of effective layers. The total number of layers in the TPC is 200.

$\Theta$ has been simulated for 10 GeV photons. The response is highly uniform for $|\cos\Theta| < 0.75$. At $\cos\Theta = 0.8$, in the transition region between barrel and endcaps, the response drops about 10% and recovers in the endcap region ($\cos\Theta > 0.8$) to a level of 5% below the barrel region (see Fig. 3.7(b)). The spatial resolution for photons has been estimated to $0.9\,\mathrm{mm}/\sqrt{(E/\mathrm{GeV})}$ and the angular resolution to $55\,\mathrm{mrad}/\sqrt{(E/\mathrm{GeV})}$.

### HCAL

The ECAL is enveloped in the second calorimetric system, the HCAL. The HCAL is designed to measure the energy of charged and neutral hadrons. It also should fully contain the hadronic showers, and have a high enough granularity to resolve the showers' substructures. Like the ECAL the HCAL consists of a barrel and two endcap regions. Two different designs are currently under investigation. The first one is a scintillator tile HCAL, the second a gaseous digital HCAL. Here the first option is described. The absorber material in both cases is iron (stainless steel), but the active medium of the tile HCAL is made of $3 \times 3\,\mathrm{cm}^2$ scintillator tiles. The scintillator tiles are read out with silicon photo-sensors (SiPMs). The HCAL has only one basic layer structure, consisting of 20 mm thick absorber plates and 6.5 mm gaps in which the scintillator plates are inserted. The barrel has a maximum of 38 layers, the maximum number of layers for the endcap is 53. The goal for the achievable energy resolution for single hadronic showers in the combined electromagnetic and hadronic calorimetric system is $\sigma_E/E \approx 35\%/\sqrt{E/(\mathrm{GeV})}$.

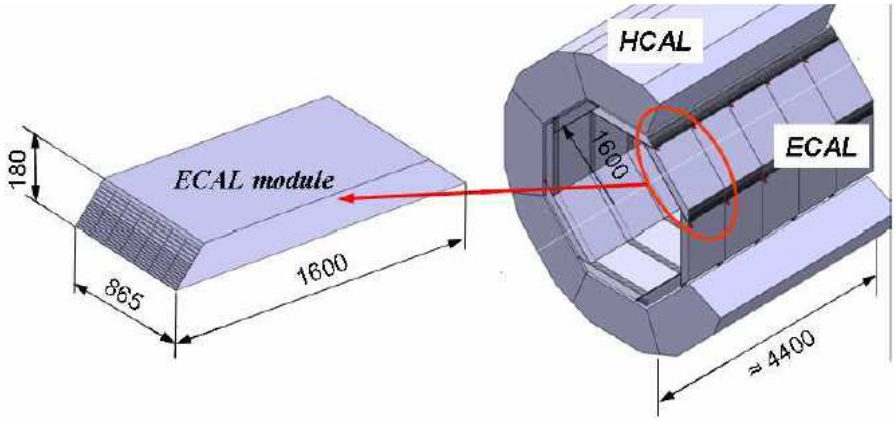


Figure 3.6: Structure of the calorimetric system. Distances are given in millimetres.

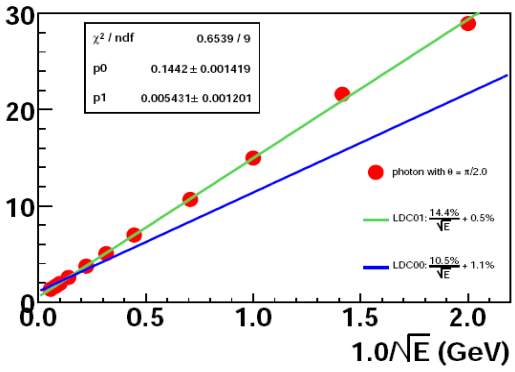


(a) Fractional energy resolution for the LDC01 and LDC00, simulated for photons with $\Theta = \pi/2$.

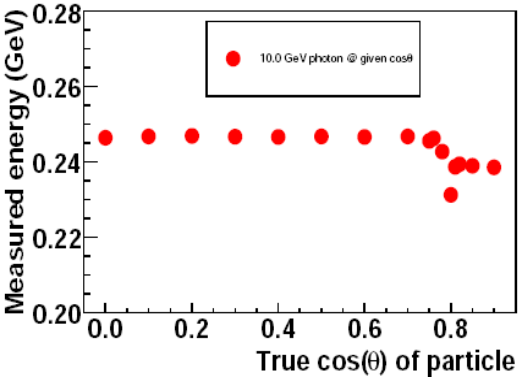


(b) Raw detector response (in arbitrary units) as function of polar angle for 10 GeV photons.

Figure 3.7: Fractional energy resolution and raw detector response for the ECAL of the LDC01Sc.

# Chapter 4

# Simulation and Reconstruction

In chapter 2.4 the theoretical description of a model-independent WIMP pair production cross section with the emission of ISR was given. In this analysis the signal is simulated by weighting the main irreducible background process, the neutrino pair production with a hard scattering photon (see sec. 2.5). The generated background sample contains two additional ISR photons. The weighting procedure (sec. 5.1) allows to cover the whole WIMP parameter space of couplings to the initial state leptons, masses, spins etc. with only one Monte Carlo production, reducing computation time spent for detector simulation considerably.
Sections 4.1 and 4.2 address the generation of the $\nu\bar{\nu}\gamma(\gamma\gamma)$ background and the simulation of the detector response to the background events. After section 4.3, describing the event reconstruction, the performance of the current reconstruction software is evaluated in section 4.4.

## 4.1 Background Generation

For the generation of the $e^+e^- \rightarrow \nu\bar{\nu}\gamma(\gamma\gamma)$ background events the Monte Carlo generator `NUNUGPV` [14] was used. This program has been developed for the LEP2 experiments where the centre of mass energy $\sqrt{s} \leq 209$ GeV exceeds the $W$-pair production threshold at $\sqrt{s} = 160$ GeV. As already stated in section 2.5 the $t$-channel $W$ exchange contributes substantially to the hard scattering neutrino production at high energies, and is therefore taken into account by `NUNUGPV`. In addition to the tree level diagrams responsible for the hard scattering photon in Fig. 2.4, `NUNUGPV` evaluates the electroweak corrections in Fig. 4.1 and topologically equal diagrams which provide for the additional ISR photons. These QED corrections are taken into account by convoluting the photon spectrum with $p_t$-dependent structure functions.
With `NUNUGPV` a sample of background events for unpolarised electrons and positrons with two additional ISR photons is generated. The cuts imposed on the hard scattering photon $\gamma_{\text{obs}}$ on generator level are listed in Table 4.1. Figure 4.2 shows the energy and $\cos\Theta$ distributions of the hard scattering photon and both of the ISR photons for the generated sample.
The ISR emission reduces the effective centre of mass energy $\sqrt{s}$. Its spectrum is plotted in Fig. 4.3. Events with $\sqrt{s} > 490$ GeV dominate the sample. This can be compared with the ISR spectra in Figure 4.2, where emission energies of less than a few GeV are the most likely. The restriction on hard scattering photons with an angle of more than 15° with the beamline is done for two reasons. First of all, the photon emission is strongly peaked in forward direction (see right column in Fig 4.2). Photons with angles of less than $\approx 8°$ (or $\cos\Theta > 0.99$) are below the calorimetric acceptance as described in section 3.2.2. So exclusion of low angle photons keeps

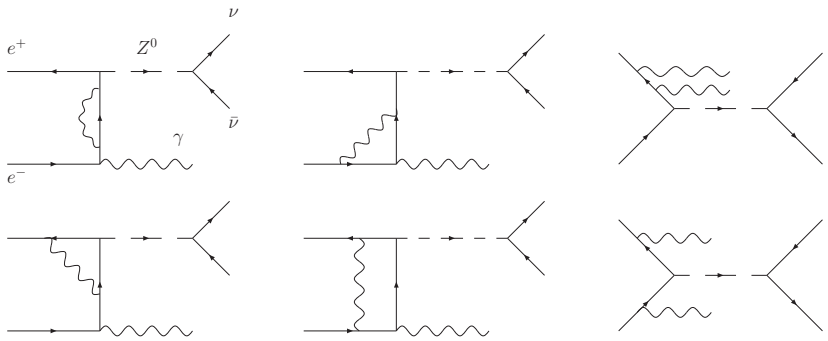


Figure 4.1: Electroweak corrections to $e^+e^- \to \nu\bar{\nu}\gamma$ (only diagrams including a $Z^0$ boson).

the total number of events low without loosing photons in the sensitive region of the detector. Second to this, the observed particles should pass the tracking system to make a differentiation between charged particles and photons possible. To allow for track reconstruction efficiencies of more than 92% the angle should comply with $\Theta > 20°$ ($\cos\Theta < 0.95$, see sec. 3.2.1). The cut is chosen to 15° because generated photons with angles slightly less than 20° might be reconstructed with angles of more than 20°. The same argument holds for the lower cut on the energy, for in the later analysis only reconstructed photon candidates with energies of more than 10 GeV will be accepted. The upper cut on the photon energy is given by kinematics. The cuts result in an integrated cross section of $\sigma_{\text{bg}} = 2.42$ pb. With this cross section an integrated luminosity of $\mathcal{L} = 500$ fb$^{-1}$ corresponds to $1.21 \times 10^6$ events.

| process<br>ISR | $e^-e^+ \to \nu\bar{\nu}\gamma(\gamma\gamma)$<br>taken into account |
|---|---|
| Number of events | $1.2 \times 10^6$ |
| $(P_{e^-}/P_{e^+})$ | (0.0/0.0) |
| $\sqrt{s}$ | 500 GeV |
| $E_{\gamma,\text{obs}}$ | 8 GeV $< E <$ 250 GeV |
| $\Theta_{\gamma,\text{obs}}$ | $15° < \Theta < 165°$ |
| $\sigma_{\text{bg}}$ | 2.42 pb |
| Int. luminosity $\mathcal{L}$ | 500 fb$^{-1}$ |

Table 4.1: `NUNUGPV` generation parameters. Constraints refer to the hard scattering photon $\gamma_{\text{obs}}$ in the laboratory frame.

## 4.2 Detector Simulation

This study is done with a full simulation of the current baseline detector model LDC01Sc of the Large Detector Concept (LDC) (section 3.2). The magnetic field has a strength of 4 Tesla. For simulation of the detector response to the generated events the Mokka 6.1 software package [25] was used. Mokka is a GEANT4 [24] based simulation tool for future linear colliders. Given a detector geometry it calculates the passage of particles through the detector and returns the detector response to the energy deposited in the individual subsystems of the detector. Because of the huge computational resources needed for this simulation it was carried out on the LHC

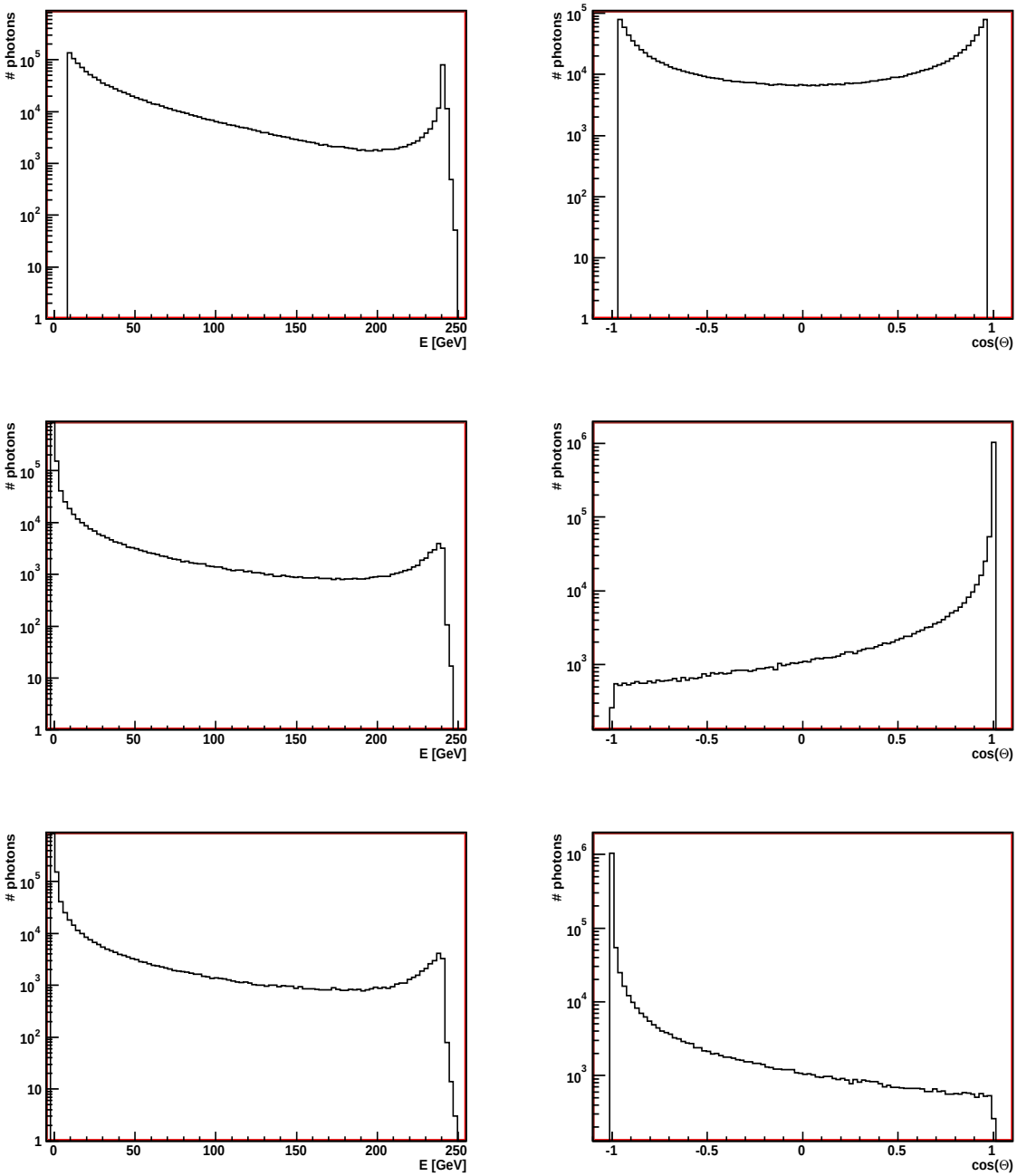


Figure 4.2: Generator spectra. The left column is (top to bottom) the energy distribution $i$) of the hard scattering photon $\gamma_{\text{obs}}$, $ii$) the ISR photon emitted from the incoming electron and $iii$) the ISR photon emitted from the incoming positron. The right column are the corresponding $\cos\Theta$ distributions.

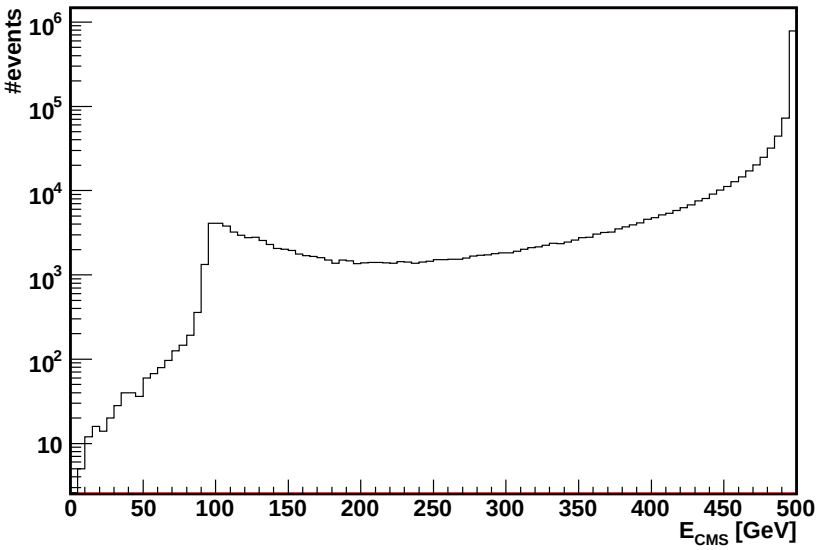


Figure 4.3: Spectrum of the reduced centre of mass energy. The reduction is due to ISR emission.

Computing Grid (LCG) [26].
As described in section 3.2.2 the ECAL consists of two different sampling structures composed of alternating layers of absorber plates (tungsten with thickness of 2.1 mm or 4.2 mm respectively) and silicon diodes for read-out. The layers themselves are segmented into $5 \times 5$ mm$^2$ cells. A particle passing through a cell deposits a fraction of its kinetic energy in both layers. This energy deposition is called the physical energy. While the energy in the absorber is lost, the energy deposited in the silicon, the so called the visible energy, is converted to an electrical signal. The signal is proportional[1] to the visible energy. The physical, kinetic energy $E_{\mathrm{phys},i}$ in cell $i$ is then related to the visible energy $E_{\mathrm{vis},i}$ by

$$E_{\mathrm{phys},i} = c_k E_{\mathrm{vis},i} \qquad k = 1, 2 \tag{4.1}$$

where $c_k$ is a calibration constant that can be obtained from simulation, and $k$ indices the two different sampling structures. Because the tungsten layer in sampling structure 2 is two times thicker than in structure 1, the calibration constant $c_2$ is roughly two times[2] $c_1$. If the energy deposited from one particle is spread over many cells, the physical energy can be reconstructed with

$$c_1 \sum_i E^1_{\mathrm{vis},i} + c_2 \sum_i E^2_{\mathrm{vis},i} = E_{\mathrm{physical}}$$

The high indices indicate the two different ECAL structures and the sums extend over all cells in each structure the particle has deposited energy in. For the HCAL only one calibration constant $c$ is needed since it only consists of one sampling structure. This energy calibration is done

[1] The proportionality holds only approximately in the absence of e.g. saturation effects etc.

[2] $c_2$ is not exactly two times $c_1$ because the ratio of thicknesses of the full layers *including* the active material is not equal to 2.

together with the digitisation within the Marlin framework (Modular Analysis and Reconstruction framework for Linear colliders) [27]. Digitisation is the process that simulates the read-out electronics and converts the visible energy to the number of activated ADC channels. The digitisation and calibration algorithm provided by Marlin is called `MokkaCaloDigi`. Table 4.2 lists the calibration constants for the calorimeters and the threshold energies for hits to be digitised. When this analysis was conducted the calibration constants for Mokka 6.1 were not available, so the constants used were those derived for Mokka 5.4. Because changes in the simulation model also change the calibration constants, these values are not optimal for Mokka 6.1 and a worsened reconstruction performance has to be expected. The influence of the inappropriate calibration constants is compensated for manually later in the analysis (sec. 4.4.3).

| `MokkaCaloDigi` | |
|---|---|
| ECAL calibration coeff. | $c_1 = 50.6653$; $c_2 = 88.7552$ |
| HCAL calibration coeff. | $c = 23.25853$ |
| Threshold for ECAL hits | $1 \times 10^{-4}$ GeV |
| Threshold for HCAL hits | $4 \times 10^{-4}$ GeV |

Table 4.2: Calibration constants and digitisation parameters in Mokka 5.4. The calibration constants apply after digitisation. They are roughly proportional to those explained in the text.

## 4.3 Event Reconstruction

Besides digitisation algorithms Marlin offers algorithms for event reconstruction. The event reconstruction in Marlin is an implementation of the Particle Flow Concept, that both exploits and requires the high granularity of the calorimetric system. Event reconstruction with Particle Flow is a combination of clustering, tracking and particle identification. The tracking algorithm will not be explained here, because it is of minor relevance to this analysis. The Marlin clustering algorithm `TrackwiseClustering` sorts the calorimeter hits by their distance to the interaction point (IP) [28]. The hits closest to the IP are taken as seeds for proto clusters. Going outward the algorithm tries to assign other hits to a proto cluster. The $i^{th}$ hit is assigned if the length $d(ij)$ of the arc defined in Figure 4.4 is less than a cut value $d_{\text{cut}}$ for any hit $j$ of the proto cluster with a distance $R$ from hit $i$ less than a cut value $R_{\text{cut}}$. If hit $i$ cannot be assigned, the procedure is repeated iteratively with hits in the proto cluster that have distances from hit $i$ less than $n \cdot R_{\text{cut}}$ until $d(ij) < d_{\text{cut}}$ or the number of iterations $n$ exceeds a limit $n_{\text{Iter}}$.
The proto cluster is finally accepted as a cluster if the number of hits exceeds a minimal number $N_{\text{min}}$ (see Table 4.3 for parameter values). After tracking and clustering, the `Wolf` algorithm identifies the particles. For this it connects clusters and tracks if the distance of closest approach falls below a certain value $s_{\text{max}}$. If a track and a cluster can be connected the particle candidate responsible for them is identified as a charged particle. A second criterion is then the fraction of energy deposited in the ECAL compared to the HCAL. If this fraction exceeds 95% the particle is identified as an electron (positron) if a track exists and as a photon if not. If less energy is found in the ECAL, or more in the HCAL respectively, the particle is tagged a pion or a kaon (neutral, or charged if a track could be matched). Muons are identified with the trackers incorporated in the iron yoke. In parallel to this full event reconstruction a reconstruction based on cheater algorithms is made. These cheater algorithms perform clustering and tracking using information from the Monte Carlo truth. The energy distribution of the particles reconstructed from these clusters represents the intrinsic energy resolution of the detector.

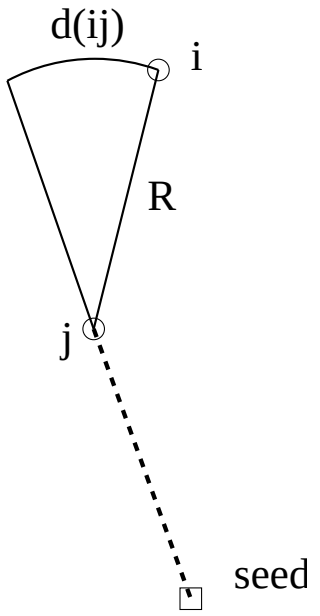


Figure 4.4: Definition of variables between hits $i$ and $j$ for the clustering method explained in the text.

## 4.4 Reconstruction Performance

Any result from a real measurement or a physics study has to be seen in the light of the detector's capability to deliver an image as close to the reality as possible of the actual physics happened. The spectrum of the hard scattering photons on generator level is shown in Figure 4.5(a) as function of the generated energy $E_{\gamma,\text{generated}}$. For this plot only photons with an angle of more than 20° with the beamline are counted. The peak of the radiative return of the $Z^0$ is clearly visible at about 240 GeV. The great abundance of photons at the low end of the distribution stems from the $t$-channel $W$ exchange. The plot in Figure 4.5(b) is the distribution of reconstructed photon candidates with angles to the beamline of more than 20°. If more than one candidate is reconstructed in this region, the candidate with the highest reconstructed energy $E_{\gamma,\text{reconstructed}}$ is selected. The first noticeable feature of the reconstructed spectrum is the missing $Z^0$ peak. Secondly, many photons are reconstructed at energies well above 250 GeV, even up to $\approx$ 300 GeV. For comparison Figures 4.5(c) and 4.5(d) are the spectrum obtained with the cheaters and an overlay of the distributions of full and cheated reconstruction. At energies around the $Z^0$ peak the full reconstruction finds less photon candidates than the cheated reconstruction. Secondly the peak of the radiative return is shifted to $\approx$ 255 GeV with the cheated reconstruction. A further investigation of the differences between these three spectra requires a connection between the photons on generator level and the photon candidates after reconstruction.

### 4.4.1 Matching of Generated and Reconstructed Photon Events

The matching between generated photons and reconstructed candidates is done by placing a cone around the direction vector of the reconstructed photon candidate. If the direction vector of a generated photon is inside this cone it is considered as matched. Two important criteria

| TrackwiseClustering | |
|---|---|
| $d_{\text{cut}}$ [mm] | 25 |
| $R_{\text{cut}}$ [mm] | 10 |
| $n_{\text{Iter}}$ | 5 |
| $N_{\text{min}}$ | 10 |
| **Wolf** | |
| B-Field [T] | 4 |
| EM Fraction | 0.95 |
| $s_{\text{max}}$ [mm] | 50 |

Table 4.3: MarlinReco reconstruction parameters. `TrackwiseClustering` parameters for ECAL only.

for matching generated to reconstructed photons are the purity $p$ and the efficiency $\epsilon$. In order to establish an unique match, $p$ and $\epsilon$ are given by:

$$p = \frac{\#\ unique\ matches}{\#\ accepted\ photons}$$

$$\epsilon = \frac{\#\ unique\ matches}{\#\ reconstructed\ photons}$$

A reconstructed photon is *accepted* when it can be matched to at least one generated photon and it is matched *uniquely* when exactly one generated photon is found in the cone. Efficiency and purity are not independent. A smaller cone opening angle increases the purity while decreasing the efficiency.
Fig. 4.6 is a purity vs. efficiency plot for a series of opening angles, starting in the lower right with $\Theta_{\text{cone}} = 0.15$ radians down to $\Theta_{\text{cone}} = 0.005$ radians in the upper left in steps of 0.005 radians. The values of $p$ and $\epsilon$ are calculated for the photons with the highest reconstructed energy in each event. Both efficiency and purity are very high over the whole range of opening angles. This is as expected from the fact that each event contains only up to three photons, when also the two ISR photons are most probable to leave the detector through the beampipe. There is an unexpected backbending in the lower right of the plot. The reason for this is that the probability of having more than one generated photon in the cone increases with larger opening angles, which in turn lowers the number of *unique* matches. From this plot an opening angle of 0.05 radians was chosen as a working point, indicated in the plot with an arrow.

### 4.4.2 Cluster Splitting

Electromagnetic particles like electrons and photons that enter the calorimeter seed an electromagnetic shower. These showers proceed through the calorimeter by a succession of $e^+e^-$ pair production and the emission of bremsstrahlung. A typical form of an electromagnetic shower can be seen in the event display in Figure 4.7. If the clustering algorithm fails to collect all energy depositions of an electromagnetic shower from one unique particle, the energy cloud can be split up in several clusters, which are then in turn identified as individual particles.
With an established matching between the reconstructed candidates and the generated photons the average number of additionally reconstructed photons in the proximity of the candidate can be plotted as a function of the generated photon's energy. A photon candidate is regarded to be in the proximity of a reconstructed and matched photon, if its direction vector lies in a cone with an opening angle of 0.1 radians around the direction of the latter photon. The result is

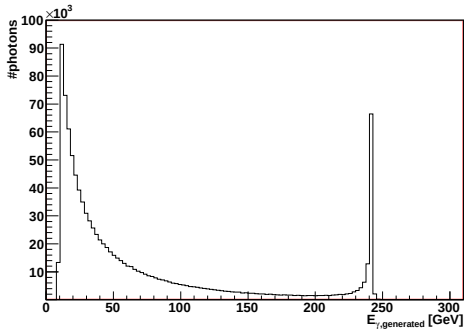


(a) Energy of hard scattering photon $\gamma_{\text{obs}}$ with $20° < \Theta < 160°$ (generator level).

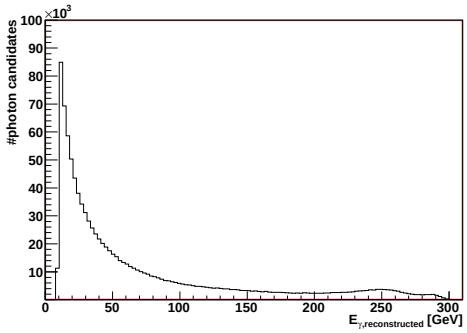


(b) Energy of most energetic photon candidates with $20° < \Theta < 160°$ (reconstruction level).

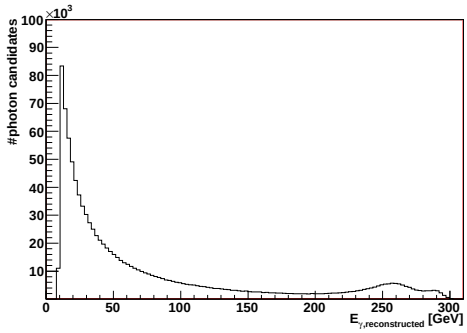


(c) Energy of most energetic cheated photon candidates with $20° < \Theta < 160°$ (cheater level).

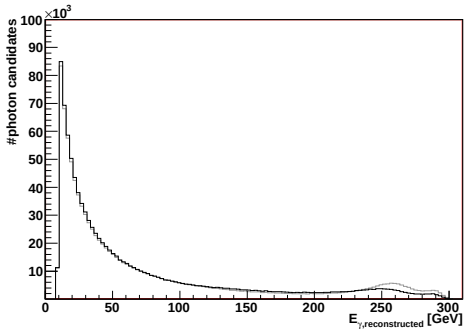


(d) Overlay of full reconstruction (black) and cheated reconstruction (grey) spectra.

Figure 4.5: Generated and reconstructed energy distributions. The photon (candidates) are restrained to $20° < \Theta < 160°$.

shown in the profile histogram in Figure 4.8(a). The average number increases from $\approx 1$ at 10 GeV to about 2 at 240 GeV, resulting in a loss of high energy photons. Photons from the $Z^0$ return are disappearing, and the height of the peak is lowered. By summing up the energies of the additionally reconstructed photons, combined photons can be constructed (see spectrum in Figure 4.8(b)). The spectrum of these combined photons is compared to that of the photon reconstruction with the cheater algorithms. The overlay and the relative difference of these two spectra in Figures 4.8(c) and 4.8(d) show that the combination of the splitted photons retrieves the cheater spectrum with great accuracy. At very high energies the distributions differ slightly more, but the relative deviation for energies of less than 250 GeV is on the level of a few percent ($\leq 5\%$). This result justifies the choice of the angle that defines the proximity. With the procedure described, the combined photon candidates inherit the assigned generated photons from the matched reconstructed photons.

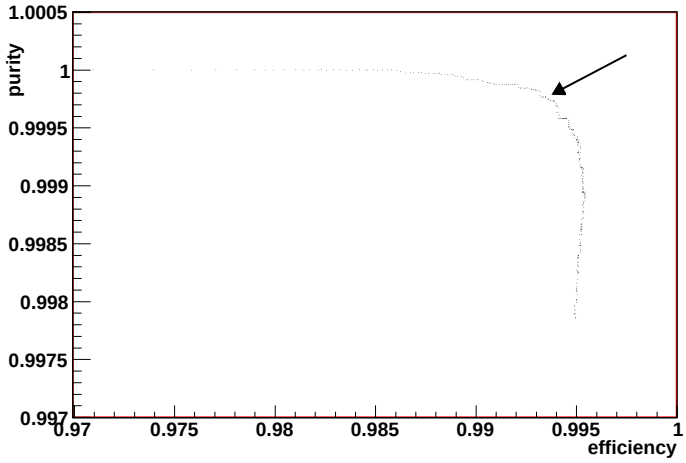


Figure 4.6: Purity vs. efficiency plot for matching generated to reconstructed photon candidates. The arrow indicates the chosen cone opening angle for the matching procedure.

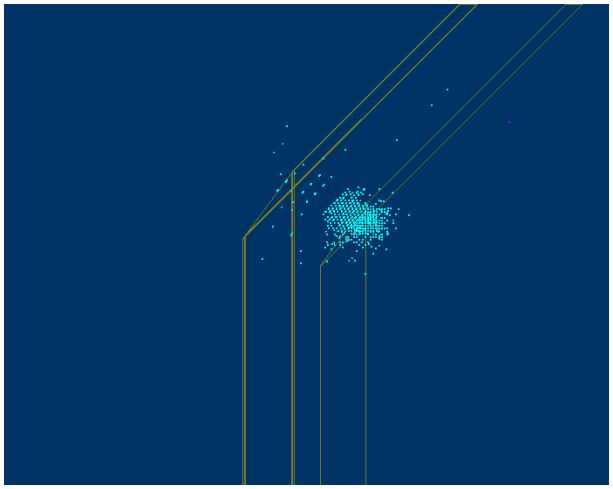

Figure 4.7: Event display of a single photon event. The cluster is mostly confined in the ECAL. Some cells in the HCAL are also hit (centre upper left).

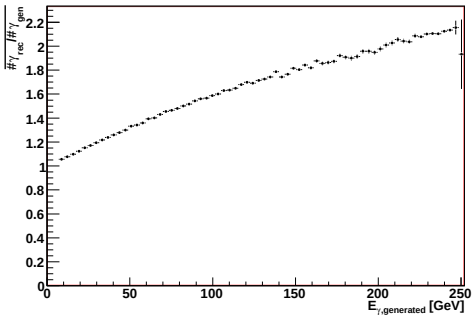


(a) Number of reconstructed photon candidates per generated photon as a function of generated energy.

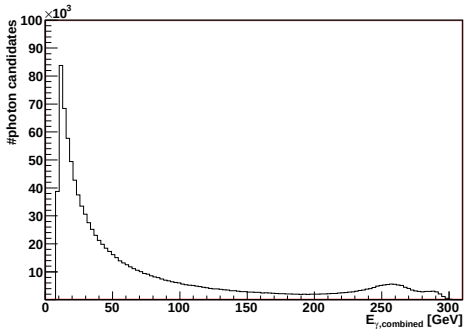


(b) Energy distribution of "combined" photons.

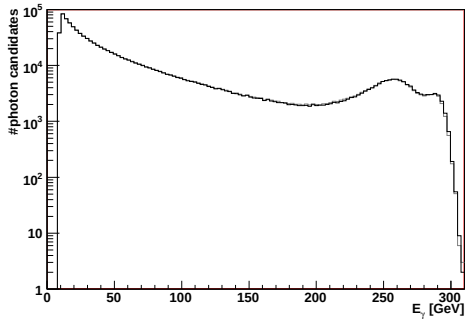


(c) Overlay of combined (grey) and cheated (black) photon candidates.

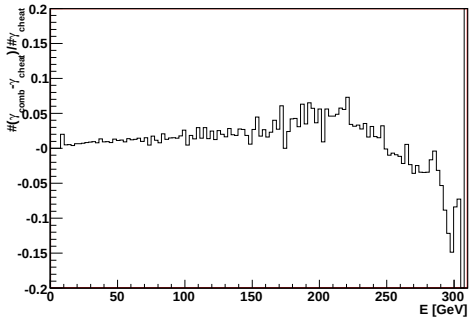


(d) Relative differences of combined and cheated photon candidates.

Figure 4.8: Plots for the combination procedure.

### 4.4.3 Energy Calibration

The energy distribution of the combined photons in Figure 4.8(b) represents almost the best reconstruction result available with the current reconstruction software, since it is very close to the results of the cheated reconstruction. As stated in sec. 4.2 the detector simulation was calibrated for the version 5.4 of the Mokka software. Figures 4.9(a) and 4.9(b) display the mean ratio of the reconstructed energy $E_{\mathrm{rec}}$ of the combined photon candidates and the energy $E_{\mathrm{gen}}$ of the matched generated photons as a function of the generated energy and $\cos\Theta$. At 20 GeV the mean reconstructed energies are about 15% higher than the generated energies, at 240 GeV the difference between reconstructed and generated energy is still 5%. The angular dependency of the ratio $E_{\mathrm{rec}}/E_{\mathrm{gen}}$ in the barrel region ($|\cos\Theta| < 0.8$) is related to the fact that only one calibration constant is used for the full angular regions covered by each sampling structure (sec. 4.2). When particles enter the calorimeter with an angle of less than 90° they have to travel through more absorber material as if they enter the calorimeter perpendicular

to its surface. This changes the ratio of physical and visible energy. Since this is a pure geometrical effect it should be straight forward to account for it in the future. In the $\cos\Theta$ plot the transition region between barrel and endcap is visible as a steep step at $|\cos\Theta| \approx 0.8$. This step corresponds to the drop in Fig. 3.7(b) which is undisturbed by geometrical effects[3]. Using the first plot the combined energies were manually calibrated by multiplying the reconstructed energies of the combined photon candidates with the mean inverse ratio $(E_{\mathrm{rec}}/E_{\mathrm{gen}})^{-1}$ evaluated for the generated photons that could be matched to the candidates. Figures 4.9(c) and 4.9(d) show the mean energy ratio $E_{\mathrm{rec}}/E_{\mathrm{gen}}$ as function of generated energy and $\cos\Theta$ after calibration. The ratio in Figure 4.9(c) is now close to constant at 1. The remaining difference of $\approx 1\%$ between reconstructed and generated energies is probably due to the remaining angular dependency (Fig. 4.9(d)) in combination with the energy and $\cos\Theta$ distributions of the events under consideration. In the energy spectrum of the combined photons (Fig. 4.9(e)) the centre of the $Z^0$ peak is now at about 240 GeV. This shift is also visible in Figure 4.9(f) which is an overlay of the combined distributions before and after calibration.

### 4.4.4 Energy Resolution

After the photon combination and manual calibration, the spectrum in Figure 4.9(e) is still differing from the generator spectrum considerably. The loss of photons at energies around the $Z^0$ peak is not as dramatic as with the full reconstruction, but the width of the now anticipational $Z^0$ resonance is of the order of $> 20$ GeV. This width is mainly governed by the energy resolution of the detector, since the natural width of the $Z^0$ resonance is with $\Gamma = 2.495$ GeV [8] one order of magnitude smaller. The detector's overall energy resolution is a convolution of contributions from the response behaviour of the active material, the amplification systems, and the read-out systems. Assuming a gaussian resolution for each contribution, the overall energy resolution is again gaussian.
To estimate the resolution for a set of fixed generated energies ranging from 50 to 240 GeV, a window with a width of 5 GeV is put around each energy point. All photons from the cheated reconstruction, for which the photon energy on generator level is within this window, are then histogramed as a function of their reconstructed energies and fitted with a gaussian. The connection between cheated reconstruction and generator information is taken from a list stored by the cheater algorithm. Two example histograms for 50 and 190 GeV are displayed in Figures 4.10(a) and 4.10(b) for calibrated candidates. Finally the resolution is calculated from the mean $\mu_E$ and the variance $\sigma_E^2$ of the fit with $\frac{\sigma_E}{\mu_E}$ and plotted as a function of $1/\sqrt{E}$, since the resolution can be approximated by the expression

$$\frac{\sigma_E}{\mu_E} \simeq \frac{\alpha}{\sqrt{E}} + b.$$

For the LDC01Sc $\alpha = 14.4\%$ and $b = 0.5\%$ are the design goals for photons with energies between 1 and 100 GeV and $\Theta = \pi/2$ ([23] and sec. 3.2.2). Figures 4.10(c), 4.10(d) and 4.10(e) show the energy resolution before manual calibration averaged over the full detector, the barrel ($|\cos\Theta| < 0.5$) and endcaps ($0.8 < |\cos\Theta| < 1$). Due to a missing factor of 2 the plotted values of the resolutions have to be doubled. The overall resolution is with $\approx 16\%$ about the same as in the barrel alone ($\frac{\sigma_E}{\mu_E} \geq 14\%$) , while the resolution in the endcaps is with 10% a little better. Responsible for the increased resolution in barrel and endcaps is the angular dependency of the ratio of reconstructed and generated energy $E_{\mathrm{rec}}/E_{\mathrm{gen}}$ (Fig. 4.9(d)), a geometrical effect[4], in combination with the cuts in $\cos\Theta$ to separate barrel and endcaps. When averaging over the

[3] Fig. 3.7(b) is obtained from the raw detector response, without digitisation.
[4] i.e. independent of the energy of the generated photons.

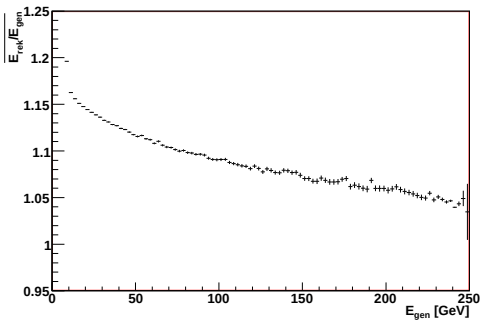


(a) Mean ratio of combined energy to generated energy as function of generated energy.

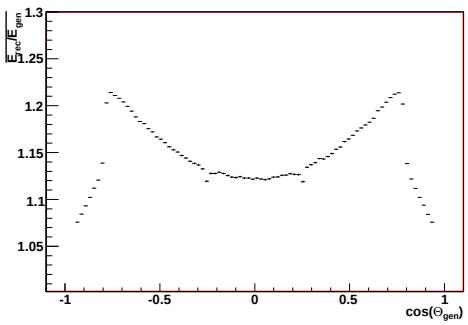


(b) Mean ratio of combined energy to generated energy as function of generated $\cos\Theta$.

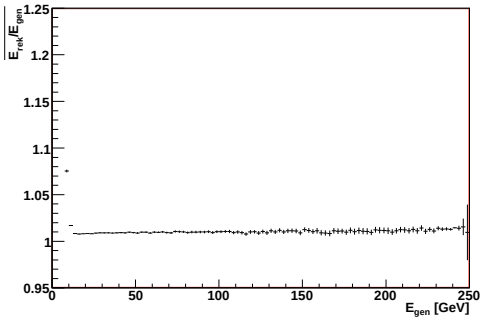


(c) Calibrated ratio of combined energy to generated energy as function of generated energy.

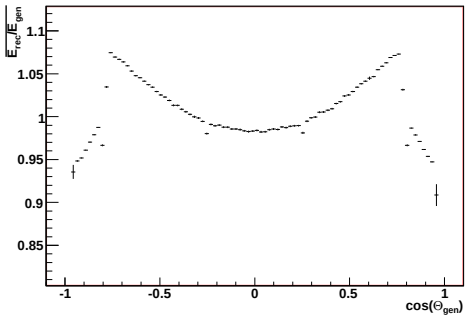


(d) Calibrated ratio of combined energy to generated energy as function of generated $\cos\Theta$.

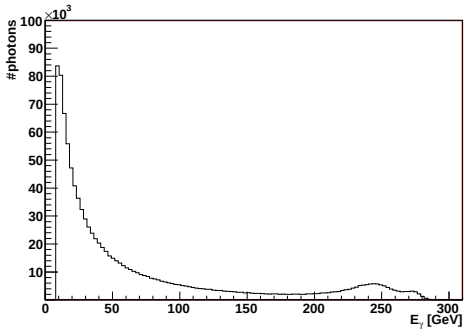


(e) Energy distribution of combined and calibrated photon candidates.

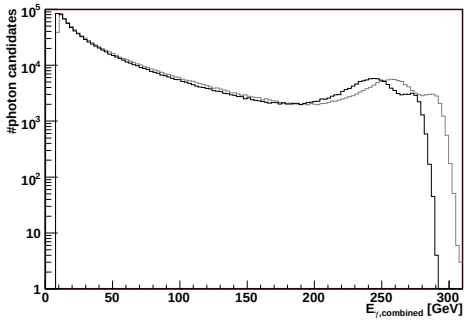


(f) Overlay of distributions of combined photon candidates with (black) and without (grey) calibration.

Figure 4.9: Plots for calibration procedure.

full detector, the mean reconstructed energies deviate from the generated energies on a larger scale. The resolution after calibration for the full detector is shown in Figure 4.10(f). For energies between 50 and 250 GeV ($0.14 > 1/\sqrt{E(\mathrm{GeV})} > 0.063$) the resolution is roughly at a constant value of about 12%, which is by a factor of $\approx 6$ worse than the design aim indicated by the solid line at the bottom. The so obtained energy resolution has to be judged with care. A strong limitation to conclusions drawn from it is that the generated photons do not have a fixed angle $\Theta$, but they are distributed according to the $\nu\bar{\nu}\gamma$ background. In general it is not expected to have the same resolution at all angles. Furthermore the method of looking at an energy window instead of using a fixed energy worsens the resolution at low energies. For example at 50 GeV ($1/\sqrt{E} = 0.14$) the relative window size is 5 %, half of the observed energy resolution. At energies above 200 GeV ($1/\sqrt{E} = 0.07$) however the relative half width is less than 1.25 %.
Nevertheless the observed energy resolution at high energies should be a good estimate of the energy resolution obtained from a more thorough test. At 240 GeV the width of the $Z^0$ peak with $\frac{\sigma_E}{\mu_E} = 0.12$ is expected to be about 28.8 GeV, not in very good accordance with the observation but in the same magnitude of $> 20$ GeV. An extrapolation of the design goal to energies of more than 200 GeV gives an expected width of about 3.4 GeV from the detector resolution alone. For a better estimate of the energy resolution, a large number of photons should be simulated at fixed energy and $\Theta$. After a series of tests at different fixed energies the energy resolution $\frac{\sigma_E}{\mu_E}$ can be plotted at different angles as function of the simulated energies.

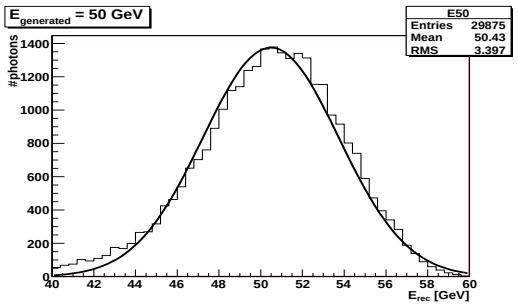


(a) Cheated reconstructed energy distribution for generated photons with 45 GeV $< E <$ 55 GeV.

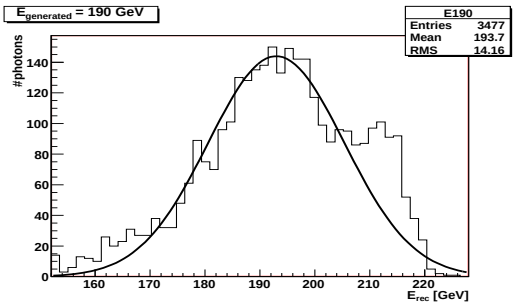


(b) Cheated reconstructed energy distribution for generated photons with 185 GeV $< E <$ 195 GeV.

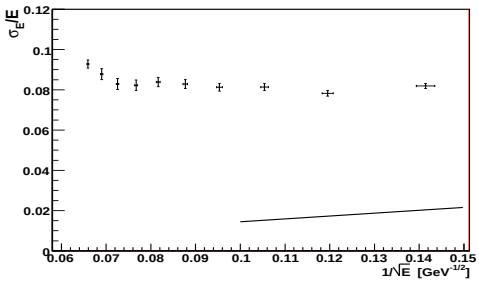


(c) Energy resolution of LDC01Sc averaged over the full detector without manual calibration. The solid line indicates the design goal for photons with energies between 1 and 100 Gev and $\Theta = \pi/2$. Plotted are the mean value of $\frac{\sigma_E}{E}$ and its error.

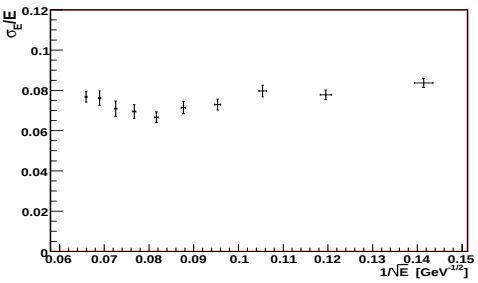


(d) Energy resolution of LDC01Sc averaged over the barrel region ($|\cos\Theta| < 0.5$) without manual calibration.

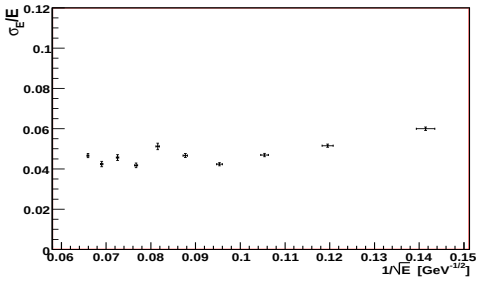


(e) Energy resolution of LDC01Sc averaged over the endcap regions ($0.8 < |\cos\Theta| < 1$) without manual calibration.

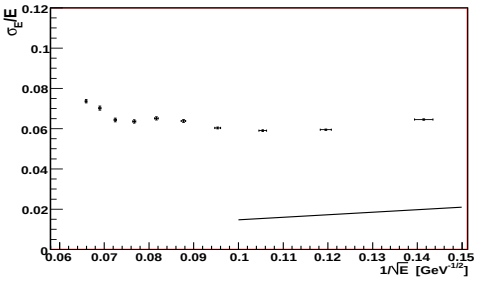


(f) Energy resolution of LDC01Sc averaged over the full detector after manual calibration. The solid line indicates the design goal for photons with energies between 1 and 100 Gev and $\Theta = \pi/2$.

Figure 4.10: Energy resolutions before and after calibration, averaged over the full detector, barrel and endcaps.

# Chapter 5

# The Analysis

In this chapter the results of this thesis are presented. In sections 5.1 and 5.2 the weighting procedure and the event selection are described. After addressing effects from signal migration in section 5.3, section 5.4 discusses the sensitivity of the ILC on the discovery of a signal, based on an event sample corresponding to an integrated luminosity of 500 $\text{fb}^{-1}$ (sec. 4.1). The cross section is probed in terms of the annihilation fraction $\kappa_e$ and as a function of the WIMP mass $M_\chi$ for spin 1 and spin 1/2 WIMPs. Exploiting the freedom of the model-independent approach, these calculations are made for three different couplings of the WIMPs to the incoming electrons and positrons. The impacts of the choice of the coupling on the sensitivity are studied for three combinations of beam polarisations: unpolarised beams, 80% electron polarisation only ($P_{e^-} = 0.8, P_{e^+} = 0.0$) and 80% electron with additional 60% positron polarisation ($P_{e^-} = 0.8, P_{e^+} = 0.6$). Section 5.5 then gives the results of the tests on the mass resolution for specific WIMP candidates with cross section parameters accessed in the reach study. For all results only statistical errors are taken into account.

## 5.1 The Weighting Procedure

After full background reconstruction the signal is simulated by assigning a weight $w_{\text{event}}$ according to the ratio of WIMP production and background cross sections to the combined and calibrated photon candidates (sec. 4.4). Weighting has the advantage that any signal hypothesis within the WIMP cross section parameter space can be tested without new Monte Carlo generation and detector simulation. Since the WIMP production cross section is given in leading order and thus includes the emission of just one photon, only one combined photon candidate is weighted in each event (sec. 5.2). The selected photon candidate is usually, but not always the photon reconstructed from the generated hard scattering photon. This ambiguity is wanted, because in a real experiment the distinction between the ISR and the hard scattering photon is not possible either.
When the combined photon candidate is picked, its weight is calculated from the hard scattering photon on generator level. In contrast to the signal process, the background contains up to two additional ISR photons. To establish comparable situations, these photons have to be removed from the events by evaluating the weights in the centre of mass frame of the intermediate leptons (i.e. the electrons and positrons after the ISR emission). The four vector $k'$ of the hard scattering photon in the new reference system of the intermediate leptons is obtained by applying a Lorentz transformation $\Lambda$ to the photon four vector $k$ in the laboratory system:

$$k'^{\mu} = \Lambda^{\mu}_{\nu} k^{\nu}, \tag{5.1}$$

or in matrix notation with the photon energy $E$:

$$\begin{pmatrix} E' \\ \vec{E}' \end{pmatrix} = \begin{pmatrix} \gamma & -\frac{\vec{v}^T}{c}\gamma \\ -\frac{\vec{v}}{c}\gamma & I + \frac{\vec{v}\vec{v}^T}{v^2}(\gamma - 1) \end{pmatrix} \begin{pmatrix} E \\ \vec{E} \end{pmatrix}. \tag{5.2}$$

The vector $\vec{v}$ is the velocity of the centre of mass of the intermediate leptons. With the four vectors $p_{e^-}$ and $p_{e^+}$ of the initial electron and positron and $p_{\gamma_{e^-}}$ and $p_{\gamma_{e^+}}$ of the ISR photons emitted from them, $\vec{v}$ is the spatial component divided by the time component of

$$\left(p_{e^-} + p_{e^+} - p_{\gamma_{e^-}} - p_{\gamma_{e^+}}\right). \tag{5.3}$$

The square reduced centre of mass energy $s'$ is given by

$$s' = \left(p_{e^-} + p_{e^+} - p_{\gamma_{e^-}} - p_{\gamma_{e^+}}\right)^2. \tag{5.4}$$

The form of the weights is determined by the following consideration. The numbers of hard scattering photon events $N_{\mathrm{bg}}$ and signal events $N_{\mathrm{sig}}$ with a dimensionless normalised energy $x = 2E_\gamma/\sqrt{s}$ between $x$ and $x + \Delta x$ and an angle between $\Theta$ and $\Theta + \Delta\Theta$ is

$$N_{\mathrm{bg}} = \mathcal{L}\frac{d^2\sigma_{\mathrm{bg}}}{dx d\Theta}\Delta x \Delta\Theta \tag{5.5}$$

$$N_{\mathrm{sig}} = \mathcal{L}\frac{d^2\sigma_{\mathrm{sig}}}{dx d\Theta}\Delta x \Delta\Theta, \tag{5.6}$$

with the integrated luminosity $\mathcal{L}$. The full number $N$ of events in this range is then:

$$N = N_{\mathrm{bg}} + N_{\mathrm{sig}} = N_{\mathrm{bg}}\left(1 + \frac{N_{\mathrm{sig}}}{N_{\mathrm{bg}}}\right) = N_{\mathrm{bg}}\left(1 + \frac{S}{B}\right). \tag{5.7}$$

$$\text{with} \quad S := \frac{d^2\sigma_{\mathrm{sig}}}{dx d\Theta} \tag{5.8}$$

$$\text{and} \quad B := \frac{d^2\sigma_{\mathrm{bg}}}{dx d\Theta}. \tag{5.9}$$

Each selected combined photon candidate therefore gets a weight $w_{\mathrm{event}}$ defined as:

$$w_{\mathrm{event}} = 1 + \frac{S}{B}, \tag{5.10}$$

evaluated with the variables $x' = E'/\sqrt{s'}$, $\cos\Theta'$ and $s'$ of the hard scattering photon on generator level. The signal-like part of each event is then $w_{\mathrm{event}} - 1$. The signal cross section is taken from the theoretical prediction Eq. (2.24) of section 2.4 (Fig. 5.1). The background cross section is obtained by filling a two dimensional histogram according to the $x' = 2E'_\gamma/\sqrt{s'}$ and $\cos\Theta'$ distributions of the generated hard scattering photons, and normalising it to the integrated cross section $\sigma_{\mathrm{bg}}$ calculated by the event generator (Fig. 5.2). In case of polarised beams the spin averaged annihilation fraction $\kappa_e$ in the signal cross section $S = S(\kappa_e)$ has to be replaced with $\kappa_e^{\mathrm{pol}}$ of Eq. (2.27) (see sec. 2.6) and the background cross section scales

approximately with $\kappa_{\rm bg} = (1 - P_{e^-})(1 - P_{e^+})$ (sec. 2.6), so $B(\kappa_{\rm bg}) = \kappa_{\rm bg} B$. The number of events $N^{\rm pol}$ in $(x, x + \Delta x)$ and $(\Theta, \Theta + \Delta\Theta)$ is now

$$N^{\rm pol} = N_{\rm bg}^{\rm pol} + N_{\rm sig}^{\rm pol} = N_{\rm bg}^{\rm pol} \left(1 + \frac{S(\kappa_e^{\rm pol})}{B(\kappa_{\rm bg})}\right) = N_{\rm bg} \kappa_{\rm bg} \left(1 + \frac{S(\kappa_e^{\rm pol})}{\kappa_{\rm bg} B}\right), \tag{5.11}$$

changing the weight $w_{\rm event}$ to

$$w_{\rm event}^{\rm pol} = \kappa_{\rm bg} \left(1 + \frac{S(\kappa_e^{\rm pol})}{\kappa_{\rm bg} B}\right) \tag{5.12}$$

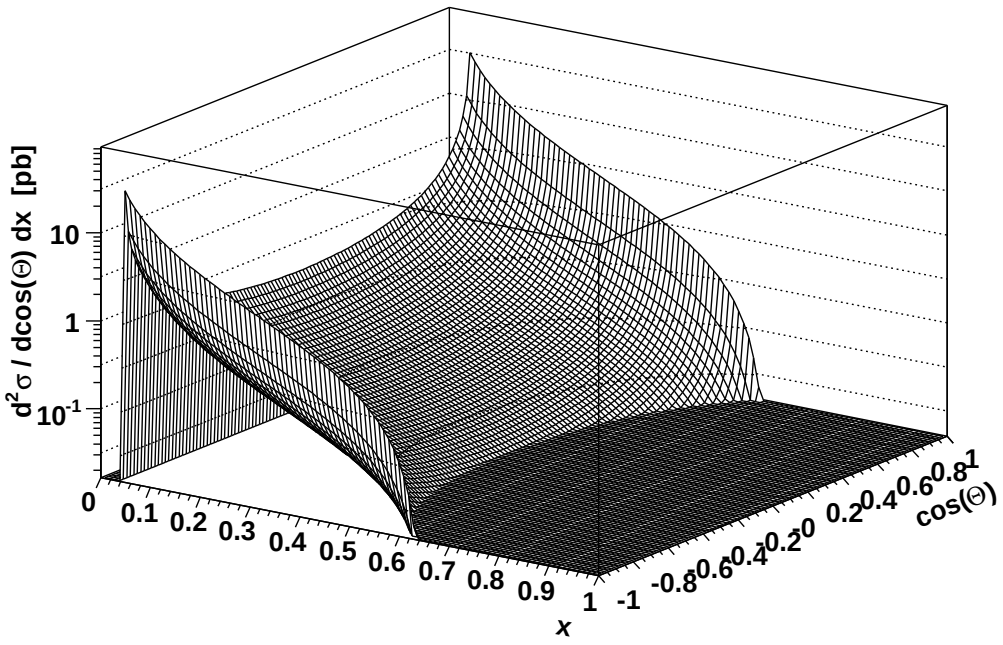


Figure 5.1: Differential cross section for the emission of the ISR photon in the process $e^+e^- \to \chi\chi\gamma$. The parameters are: $M_\chi = 150$ GeV, $S = 1$, $J = 1$ and $\kappa_e = 1$. The photon is restrained by: $E_{\gamma,\rm ISR} > 10$ GeV and $\sin\Theta_\gamma > 0.1$.

## 5.2 The Selection

This section gives a brief summary of the cuts applied on the background event sample during the analysis. The cuts can be classified in three groups. The first group of cuts are performed on generator level (see sec. 4.1) These cuts are intended to reduce the amount of data. The generator cuts are:

1. The energy of the hard scattering photon $\gamma_{\rm obs}$ has to comply with 8 GeV $< E_{\gamma_{\rm obs}} <$ 250 GeV. The upper cut follows from kinematics.

2. The angle of the hard scattering photon with the beamline is restrained to $15^\circ < \Theta < 165^\circ$.

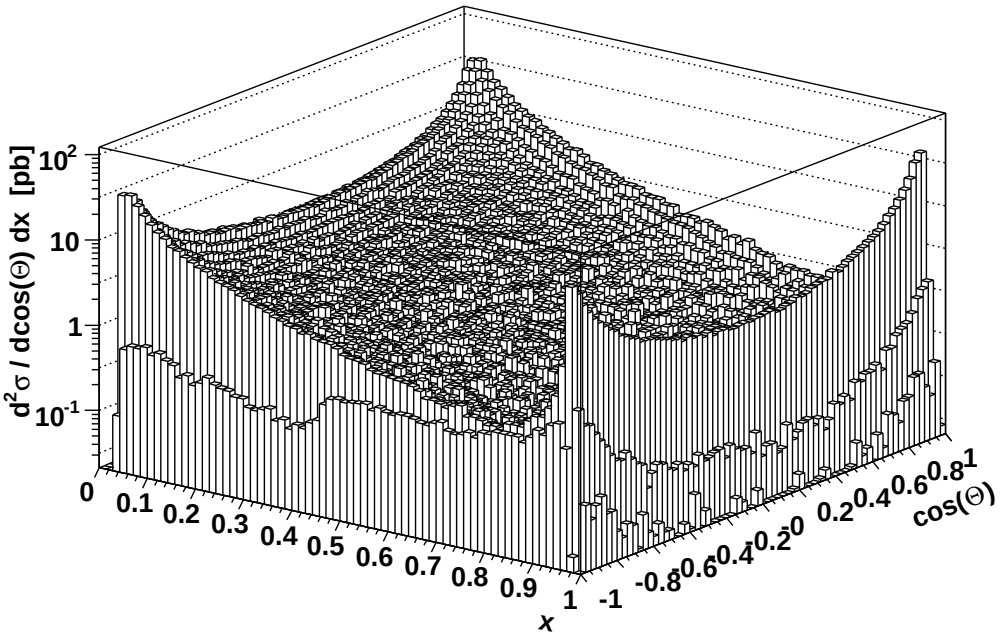


Figure 5.2: Differential cross section for the emission of the hard scattering photon in the process $e^+e^- \to \nu\bar{\nu}\gamma(\gamma\gamma)$. The variables $x = 2E_\gamma/\sqrt{s}$ and $\cos\Theta$ are evaluated in the centre of mass frame of the intermediate electrons and positrons.

After the detector simulation and event reconstruction some selection cuts are performed. From each event one combined and calibrated photon candidate is selected. The set of photon candidates which pass this selection is the basis for the further analysis. The selection cuts are:

1. The first cut is a cut on the energy of the photon candidates. The reconstructed energy is demanded to be higher than 10 GeV.

$$10\,\mathrm{GeV} < E_\gamma.$$

2. After the cut on the photon energy, the photon candidates' angles with the beam line is cut on. The angles have to comply with:

$$20^\circ < \Theta < 160^\circ.$$

   As described in section 3.2.1, the track reconstruction efficiency is 92% in this angular region. Thus discrimination between charged an neutral candidates is possible, and backgrounds from e.g. Bhabha scattering (sec. 2.5) would be reduced efficiently.

3. The photon candidate with maximal energy is selected.

Additional cuts are applied before the sensitivity calculation. For technical reasons they are not applied in the calculation of the mass resolution (see sec. 5.5). The cross section derived in

section 2.4 is only valid for non-relativistic WIMPs. To assure this, a lower cut is applied on the photon candidate's energy. This cut depends on the WIMP mass $M_\chi$:

$$E_{\text{cut}} = \frac{E_{\text{beam}}^2 - 2M_\chi^2}{E_{\text{beam}}}, \tag{5.13}$$

where $E_{\text{beam}}$ is the beam energy and $E_{\text{cut}}$ the minimum ISR photon energy. Table 5.1 lists the generator and selection cuts applied and the number of remaining background events. In Table 5.2 the number $N_{\text{bg}}$ of background events after the mass dependent relativistic cut is listed for some selected WIMP masses. Also listed is the number of signal events after these cuts. The numbers are valid for unpolarised beams, $J = 1$, $S = 1$ and $\kappa_e = 1$. In case of polarisation these numbers scale approximately with $\kappa_{\text{bg}} = (1 - P_{e^-})(1 - P_{e^+})$ (background) and $\kappa_e^{\text{pol}}$ of Eq. (2.27) (signal).

| cuts | Number of events |
|---|---|
| generator cuts | $1.21 \times 10^6$ |
| selection cuts | $1.07 \times 10^6$ |

Table 5.1: Cut-flow table for generator and selection cuts for unpolarised beams.

| WIMP mass [GeV] | 30 | 90 | 150 | 160 | 170 | 180 | 210 | 240 |
|---|---|---|---|---|---|---|---|---|
| $E_{\text{cut}}$ [GeV] | 242.8 | 185.2 | 70 | 45.2 | 18.8 | 0 | 0 | 0 |
| $N_{\text{bg}}$ [$\times 10^3$] | 64 | 131 | 315 | 438 | 729 | 1066 | 1066 | 1066 |
| $N_{\text{sig}}$ [$\times 10^3$] | 1.6 | 1.6 | 31.7 | 38.3 | 51.9 | 65.5 | 18.6 | 0.4 |

Table 5.2: Number of events after some selected mass dependent cuts. The numbers are for unpolarised beams, $J = 1$, $S = 1$ and $\kappa_e = 1$. In case of polarisation these numbers scale with $\kappa_{bg} = (1 - P_{e^-})(1 - P_{e^+})$ (background) and $\kappa_e^{\text{pol}}$ of Eq. (2.27) (signal).

## 5.3 Effects of Signal Migration

WIMPs with masses of e.g. 50 GeV, produced at the ILC's centre of mass energy of 500 GeV will be mostly relativistic and the emitted photon energies small. So to ensure $\beta_\chi = v_\chi/c \ll 1$ the energy of the reconstructed photon events has to comply with the relativistic cut (5.13):

$$E_{\text{cut}} < E_\gamma \tag{5.14}$$

The sensitivity to a signal depends on the ratio of signal events $S$ to background events $B$. After reconstruction some events with generated energies from below the cut may have migrated to above the cut. This leads not only to a higher background rate, but also to more signal events, depending on the weight of the events. To quantify migration effects the relative amounts of accepted, expected and migrated signals are looked at. A signal is accepted by the cut, when the reconstructed energy of the weighted photon candidate is higher than $E_{\text{cut}}$. It is migrated (expected) when it is accepted and the generated photon energy of the reconstructed photon candidate holds $E_{\gamma,\text{gen}} < E_{\text{cut}}$ ($E_{\gamma,\text{gen}} > E_{\text{cut}}$ respectively). Figure 5.3 shows on the left-hand side the ratio of signal events accepted by the cut to the signal events expected as a function of the WIMP mass. At masses below 80 GeV the accepted signal rate is higher than the expected rate by a factor between 3 (at 80 GeV) and 18 (at 30 GeV). Above $M_\chi = 80$ the

ratio drops below 2 with an fluctuation at about 140 GeV. Whether the migrated signal events influence the sensitivity calculation can be derived from the plot on the right. Displayed are the ratio of signal events $S$ to the square root of background events $\sqrt{B}$ (the poisson standard deviation) for the migrated signal (dashed line) and expected signal (solid line). The expected ratio exceeds the migrated ratio at masses above $\approx 130$ GeV. Below that mass any test on the sensitivity is strongly improved by migration. Above 130 GeV the expected signal dominates the ratio $S/\sqrt{B}$ by at least a factor of 10. Here the effects of migration are minor, especially the spike at 140 GeV in the left plot has not much influence on the sensitivity calculations. Strong migration extends the observability to relativistic WIMPs, but a comparison with the cosmological restraints on the annihilation cross section $\sigma_{\mathrm{an}}$ is not possible any more.

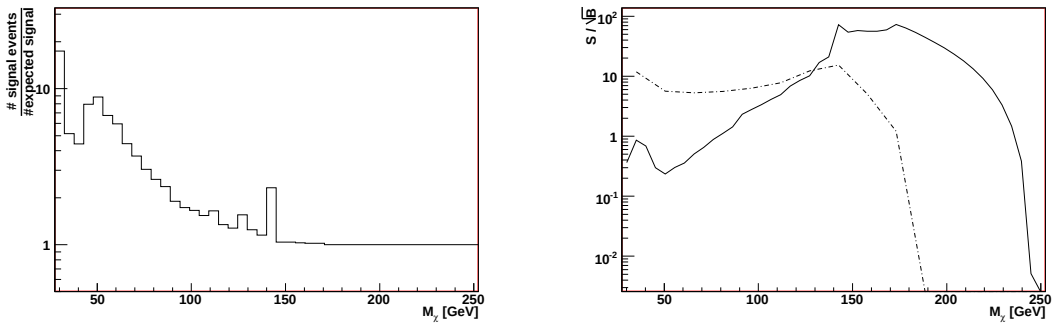


Figure 5.3: Left: ratio of accepted signal events to expected signal events as a function of WIMP mass. Right: ratio of expected (solid line) and migrated (dashed line) signal events $S$ to $\sqrt{B}$ of background events $B$.

## 5.4 Sensitivity

The following paragraphs present the results of the calculations of the sensitivity on the observation of a signal. They are based on a sample of background events corresponding to an integrated luminosity of 500 fb$^{-1}$. The sensitivity curves are calculated on $3\sigma$ level and only statistical errors are taken into account. The input to the calculations are the energy and $\cos(\Theta)$ distributions of the photon candidates for signal and background. They serve as the expected signal and background rates. The plots in Figure 5.4 show the input histograms for signal and background for WIMP masses of 150 and 200 GeV. In both cases the annihilation fraction $\kappa_e$ is set to one[1]. The relativistic cut is visible at photon energies of 70 GeV in the 150 GeV histograms. The statistical errors are plotted. Close to the cut the signal amounts to about 30 to 40% of the background. This large value is due to the choice of $\kappa_e$. Strong signal fluctuations caused by large event weights can be seen over the full signal range, especially in the $\cos\Theta$ plot. The exact reason is not known, although the stronger fluctuations in the case of 150 GeV WIMPs compared to the 200 GeV WIMPs indicate that they are due to the loss of statistics caused by the relativistic cut (Eq. (5.13) and Table 5.2). Next to this explanation, migrations effects might contribute, and the large weights might come from the center of the

[1] i.e. the WIMPs couple only to electrons and positrons.

$x$-$\Theta$ region, where statistical fluctuations can be seen in the background cross section (Fig. 5.2). Overall a further understanding of the systematical errors is needed.
All WIMP candidates are assumed to be $p$-annihilators ($J = 1$) with spin 1 or $\frac{1}{2}$. The value of the annihilation cross section $\sigma_{\mathrm{an}}$ is set from Fig. 2.3 to 6 pb throughout the analysis.

### 5.4.1 Helicity Conserving, SM Charged Weak Interaction-like Couplings

When the WIMP couplings conserve helicity but not parity, only one of the spin-dependent annihilation fractions $\kappa(e^R_- e^L_+)$ and $\kappa(e^L_- e^R_+)$ is non-zero (sec. 2.6). The other two parameters $\kappa(e^R_- e^R_+)$ and $\kappa(e^L_- e^L_+)$ describe couplings that do not conserve helicity, so $\kappa(e^R_- e^R_+) = \kappa(e^L_- e^L_+) \equiv 0$.

**p-annihilator, $S_\chi = 1$, $\kappa(e^R_- e^L_+) = 0$, $\kappa(e^L_- e^R_+) = 4\kappa_e$**

With $\kappa(e^R_- e^L_+) = 0$ and $\kappa(e^L_- e^R_+) = 4\kappa_e$ the WIMP couplings to the leptons are the same as for the standard model neutrinos. Figure 5.5 shows the sensitivity curves on the spin averaged $\kappa_e$ as a function of the WIMP mass $M_\chi$. The curves are calculated for unpolarised beams (solid line), 80 % electron polarisation only (dotted line) and for 80% electron polarisation with additional 60% positron polarisation (dashed line). The left plot with a decimal scale in $\kappa_e$ covers a range of masses from 30 to 250 GeV. For unpolarised beams the sensitivity on $\kappa_e$ is at 0.3 for a mass of 30 GeV and rises to about 0.8 at 50 GeV. The higher sensitivity on $\kappa_e$ at 30 GeV compared to 50 GeV is a result of the migration effects described in the previous chapter. Between 120 and 210 GeV the limits for a $3\sigma$ observation are below 0.1, down to about 0.02 at 150 GeV. As described, the migration is expected to increase the sensitivity for WIMP masses up to 130 GeV. Therefore in the right plot in Figure 5.5 the x-axis covers only masses between 100 and 250 GeV and a logarithmic scale is chosen for a better comparison between the different polarisation configurations. Beam polarisation reduces the signal by roughly the same factor as the background rate. The ratio $S/\sqrt{B}$ of signal to the square root of the background thus decreases and the sensitivity is lowered. Electron polarisation decreases the reach by a factor of about 2.2 over the full range of masses. Additional positron polarisation reduces the reach again by a factor of $\approx 1.6$.

**p-annihilator, $S_\chi = \frac{1}{2}$, $\kappa(e^R_- e^L_+) = 0$, $\kappa(e^L_- e^R_+) = 4\kappa_e$**

Figures 5.6 are again sensitivity plots for a $p$-annihilator WIMP, but now with a spin of $S = \frac{1}{2}$. The WIMP couplings are the same as in the previous case. The plot axises and line codings (solid, dotted and dashed) are as in Figure 5.5. The accessible region for a spin $\frac{1}{2}$ WIMP is considerably smaller as in the spin 1 case. Between 120 and 210 GeV the limit lies below 0.3 with a minimum of 0.05 at 150 GeV. Below 75 GeV no observation is possible on a $3\sigma$ level. This is probably also true for masses higher than 75 GeV where migration still is influential. The effects of beam polarisation are at the same order and direction as for a spin 1 WIMP.

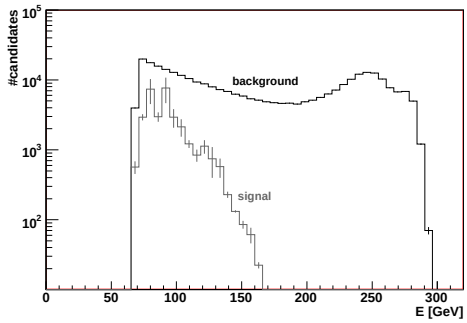


(a) Input histogram to the sensitivity algorithm. Energy distributions of signal (grey) and background (black) for a 150 GeV WIMP with $\kappa_e = 1$.

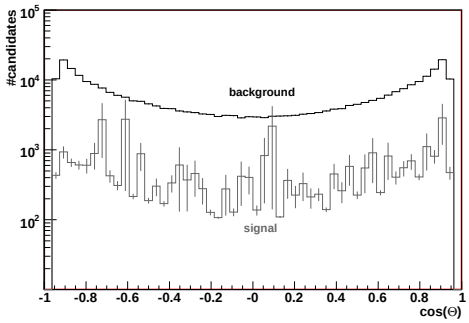


(b) Input histogram to the sensitivity algorithm. $\cos\Theta$ of signal (grey) and background (black) for a 150 GeV WIMP with $\kappa_e = 1$.

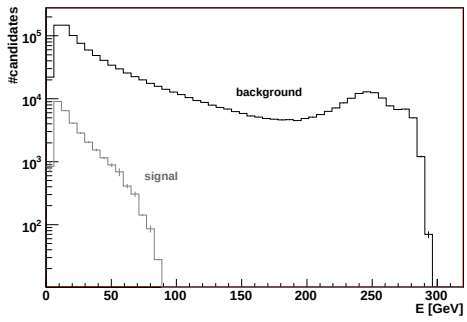


(c) Input histogram to the sensitivity algorithm. Energy distributions of signal (grey) and background (black) for a 200 GeV WIMP with $\kappa_e = 1$.

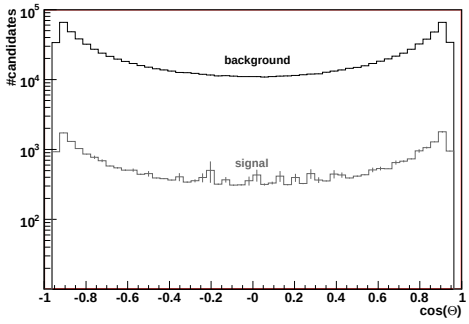


(d) Input histogram to the sensitivity algorithm. $\cos\Theta$ of signal (grey) and background (black) for a 200 GeV WIMP with $\kappa_e = 1$.

Figure 5.4: Input histograms for the sensitivity calculation. The WIMP candidates are 150 and 200 Gev, spin 1 $p$-annihilators. The remaining parameters are set to $\kappa_e = 1$ and $\sigma_{\text{an}} = 6$ pb.

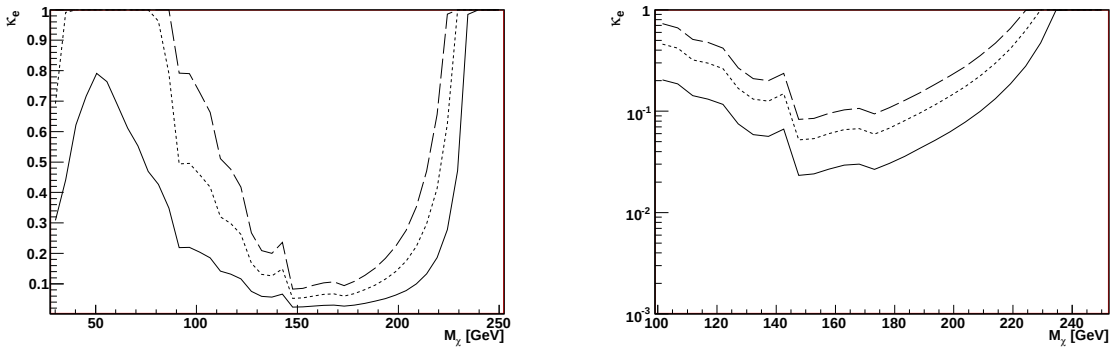


Figure 5.5: Reach on $3\sigma$ level on the parameter $\kappa_e$ as a function of the WIMP mass $M_\chi$. The limits are calculated for 500 fb$^{-1}$ experiment. The WIMP couplings have the same helicity dependency as the SM charged weak interaction. The WIMP candidates are spin 1 $p$-annihilators. The limits are for unpolarised beams (solid), 80% $e^-$ polarisation (dotted) and additional 60% $e^+$ polarisation. Left: decimal scale. Right: cutout with logarithmic scale.

### 5.4.2 Helicity Conserving Couplings, Opposite to SM Charged Weak Interaction

**p-annihilator,** $S_\chi = 1$**,** $\kappa(e^R_- e^L_+) = 4\kappa_e$**,** $\kappa(e^L_- e^R_+) = 0$

This and the next WIMP candidate differ from the previous two in the couplings to the leptons. In opposition to the standard model neutrinos they couple to right-handed electrons and left-handed positrons. Sensitivity curves for a spin 1 WIMP candidate are plotted in Figure 5.7. The limits for unpolarised beams are the same as for the spin 1 WIMP with the neutrino-like couplings. But here beam polarisation increases the $S/B$ ratio allowing for smaller limits to be set. Polarised electrons limit the $\kappa_e$ on $3\sigma$ level to 0.006 (factor 3.5) at 150 GeV. Polarisation of both electrons and positrons lowers this limit to 0.002 (factor 3).

**p-annihilator,** $S_\chi = \frac{1}{2}$**,** $\kappa(e^R_- e^L_+) = 4\kappa_e$**,** $\kappa(e^L_- e^R_+) = 0$

With the spin set to $\frac{1}{2}$ the accessible region becomes smaller in comparison to the spin 1 case (Fig. 5.8). The positive effects of beam polarisation manifest again in a successive lowering of the limits by factors of 4 and 2.3.

### 5.4.3 Parity and Helicity Conserving Couplings

Parity and helicity conserving couplings are characterised with the spin-dependent annihilation fractions $\kappa(e^R_- e^L_+) = \kappa(e^L_- e^R_+) = 2\kappa_e$ and $\kappa(e^R_- e^R_+) = \kappa(e^L_- e^L_+) = 0$ (see sec. 2.6).

**p-annihilator,** $S_\chi = 1$**,** $\kappa(e^R_- e^L_+) = \kappa(e^L_- e^R_+) = 2\kappa_e$

Figure 5.9 is the $3\sigma$ plot for a spin 1 WIMP. Although the neutrino-like part of the couplings reduces the $S/B$ ratio, the net effect is an increase of the signal to background ratio as one can see from

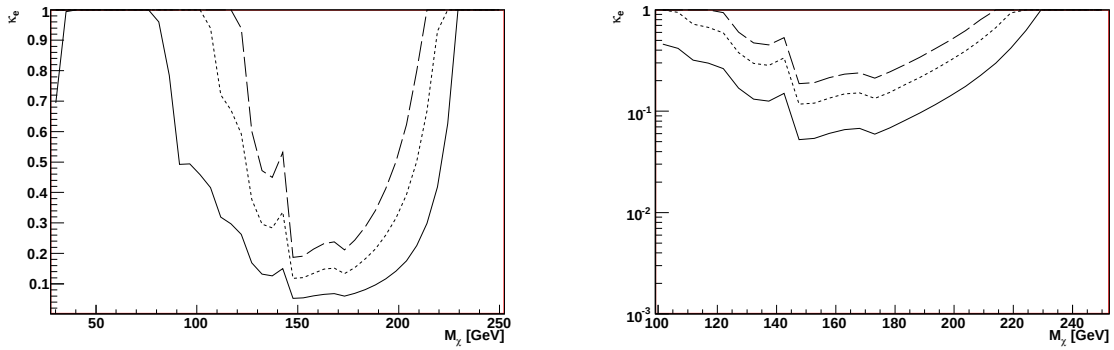


Figure 5.6: Reach on $3\sigma$ level on the parameter $\kappa_e$ as a function of the WIMP mass $M_\chi$. The limits are calculated for 500 fb$^{-1}$ experiment. The WIMP couplings have the same helicity dependency as the SM charged weak interaction. The WIMP candidates are spin $\frac{1}{2}$ $p$-annihilators. The limits are for unpolarised beams (solid), 80% $e^-$ polarisation (dotted) and additional 60% $e^+$ polarisation. Left: decimal scale. Right: cutout with logarithmic scale.

$$\frac{(S/B)_{\text{pol}}}{(S/B)_{\text{unpol}}} = \frac{1}{2}\left(\frac{(1+P_{e^-})(1+P_{e^+})}{(1-P_{e^-})(1-P_{e^+})}+1\right), \tag{5.15}$$

using Equation (2.27) and the scaling factor $\kappa_{\text{bg}}$ of the background. Fully polarised beams ($P_{e^-}=0.8, P_{e^+}=0.6$) enhance the ratio by a factor of 18.5. For masses between 120 and 210 GeV and unpolarised beams the accessible region goes down to below 0.1. The sensitivity is increased by a factor of $\approx 5$ by full electron and positron polarisation.

**p-annihilator, $S_\chi = \frac{1}{2}$, $\kappa(e^R_- e^L_+) = \kappa(e^L_- e^R_+) = 2\kappa_e$**

Figure 5.10 is again an sensitivity plot for helicity and parity conserving couplings. The spin of the WIMP candidate is $\frac{1}{2}$. The scaling factor $\kappa_e$ can be probed down to 0.05 for unpolarised beams at a mass of 150 GeV. The increase in sensitivity through beam polarisation is indicated by the dotted and dashed lines.

Given a typical MSSM value of 0.3 for $\kappa_e$ [13] a $3\sigma$ observation of p-annihilator WIMPs with spin 1 should be possible for all investigated couplings and unpolarised beams between $M_\chi = 90$ GeV and $M_\chi = 225$ GeV ($M_\chi = 120$ GeV to $M_\chi = 215$ GeV for spin $\frac{1}{2}$). The increase in sensitivity with fully polarised beams is especially noticeable for couplings opposite to the SM weak interaction. Here an overall increase by a factor of $\approx 10$ is observed. For helicity and parity conserving couplings the effect is a factor of 5 in increase.

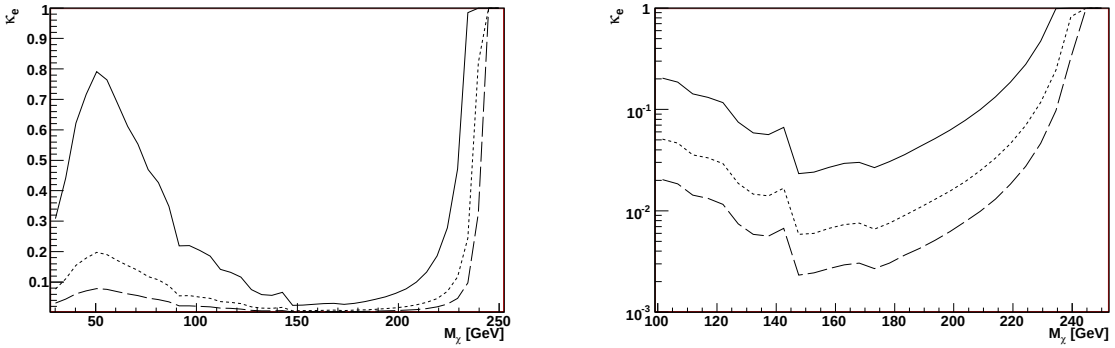


Figure 5.7: Reach on $3\sigma$ level on the parameter $\kappa_e$ as a function of the WIMP mass $M_\chi$. The limits are calculated for 500 fb$^{-1}$ experiment. The WIMP couplings have the opposite helicity dependency as the SM charged weak interaction. The WIMP candidates are spin 1 $p$-annihilators. The limits are for unpolarised beams (solid), 80% $e^-$ polarisation (dotted) and additional 60% $e^+$ polarisation. Left: decimal scale. Right: cutout with logarithmic scale.

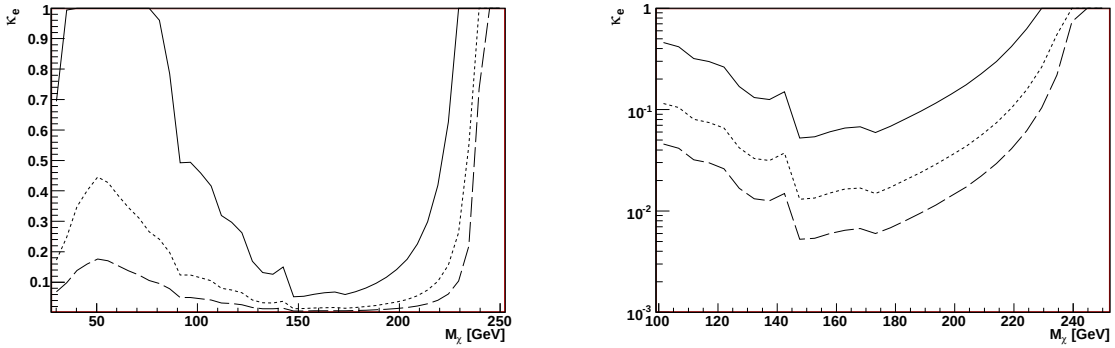


Figure 5.8: Reach on $3\sigma$ level on the parameter $\kappa_e$ as a function of the WIMP mass $M_\chi$. The limits are calculated for 500 fb$^{-1}$ experiment. The WIMP couplings have the opposite helicity dependency as the SM charged weak interaction. The WIMP candidates are spin $\frac{1}{2}$ $p$-annihilators. The limits are for unpolarised beams (solid), 80% $e^-$ polarisation (dotted) and additional 60% $e^+$ polarisation. Left: decimal scale. Right: cutout with logarithmic scale.

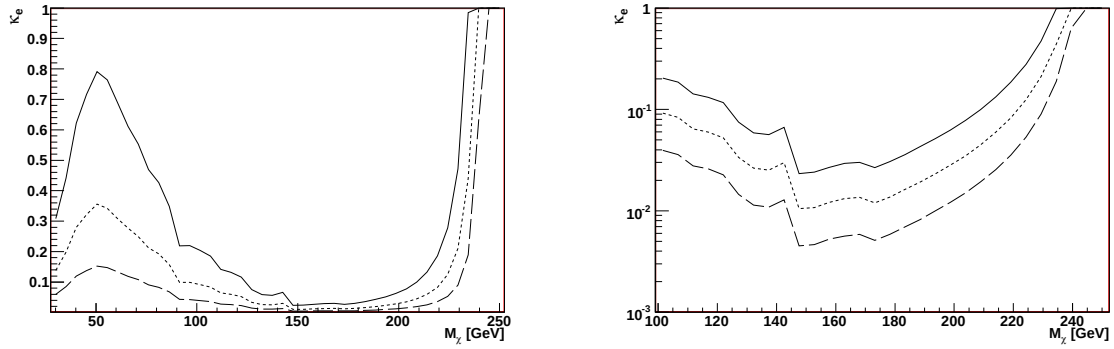


Figure 5.9: Reach on $3\sigma$ level on the parameter $\kappa_e$ as a function of the WIMP mass $M_\chi$. The limits are calculated for 500 fb$^{-1}$ experiment. The WIMP couplings conserve both helicity and parity. The WIMP candidates are spin 1 $p$-annihilators. The limits are for unpolarised beams (solid), 80% $e^-$ polarisation (dotted) and additional 60% $e^+$ polarisation. Left: decimal scale. Right: cutout with logarithmic scale.

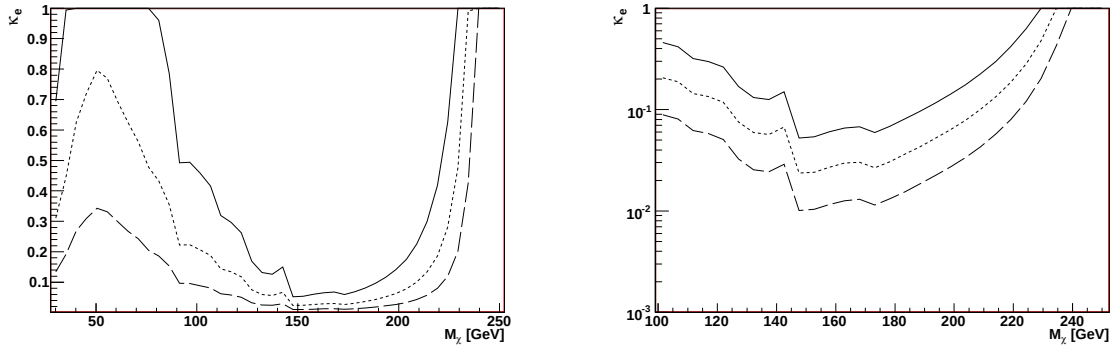


Figure 5.10: Reach on $3\sigma$ level on the parameter $\kappa_e$ as a function of the WIMP mass $M_\chi$. The limits are calculated for 500 fb$^{-1}$ experiment. The WIMP couplings conserve both helicity and parity. The WIMP candidates are spin $\frac{1}{2}$ $p$-annihilators. The limits are for unpolarised beams (solid), 80% $e^-$ polarisation (dotted) and additional 60% $e^+$ polarisation. Left: decimal scale. Right: cutout with logarithmic scale.

## 5.5 Mass Resolution

Once a signal is observed, one of the first questions to arise is, if and how well the mass of the WIMP candidate can be determined. The mass resolution is investigated by comparing the recoil mass spectrum of signal plus background for a given WIMP with the expected spectra of different signal hypotheses. As in the sensitivity calculations only statistical errors are taken into account. A good figure of merit is the value of the $\chi^2$ test statistics (sec. 2.7.2). The smaller the value, the better the agreement between "measurement" and hypothesis. For the following results the event sample of a corresponding luminosity of 500 $\mathrm{fb}^{-1}$ is split up into two blocks with sizes of 1/3 and 2/3 of the full sample. The larger block is used as the weighting basis of the hypotheses, the other one serves for the "data". Due to the splitting, the effective luminosity is lowered to $\mathcal{L} = 167\,\mathrm{fb}^{-1}$, or about one year of data taking with the ILC. The recoil mass calculates from

$$M_{\mathrm{recoil}} = \sqrt{s - 2\sqrt{s}E_\gamma}$$

where $\sqrt{s}$ is the centre of mass energy and $E_\gamma$ the energy of the photon candidate. Each candidate is again weighted with the hard scattering photon on generator level. In Figures 5.11(a) and 5.11(b) the recoil spectrum for a $p$-annihilator, spin 1 WIMP signal of 150 GeV is shown, with $\kappa_e = 0.3$ and $\sigma_{\mathrm{an}} = 6$ pb. The couplings are helicity and parity conserving, beams are unpolarised. At $\approx 300$ GeV the signal (white) kicks in, corresponding to the maximal kinetically allowed photon energy of 160 GeV. Figures 5.11(c) and 5.11(d) display the recoil distributions for fully polarised $e^-$ and $e^+$ beams for the 150 GeV DM candidate and additionally for a 100 GeV WIMP with the same remaining parameters. The 100 GeV signal starts at $\approx 200$ GeV. The relativistic lower cut of sec. 5.3 is an upper cut in the recoil distribution, depending on the WIMP mass. To make possible a comparison between different mass hypotheses the cut is not applied in this test. Observed resolutions are however not strongly influenced therefrom, because the main criterion for the mass determination is not the absolute norm, but the "kick in" point of the signal. The mass resolution is then determined by the values of the hypothesised WIMP masses for which the difference between the value of $\chi^2$ test and the minimal value of this test is 1. The fluctuations of the signal are boosted strongly through polarisation. Their position however is independent of the tested WIMP masses, since it only depends on the differences between $x$ and $\Theta$ of the generated hard scattering photon (from which the event weight is calculated) and the selected reconstructed photon (whom the weight is assigned to). The obtained mass resolutions are not heavily affected by the increased weights, because they cancel out in the $\chi^2$ function (Eq. (2.53)) with the large statistical errors (see Fig. 5.11(c) and 5.11(d)).

### 5.5.1 Helicity Conserving, SM Charged Weak Interaction-like Couplings

In the following the results of the tests on the mass resolution for spin $\frac{1}{2}$ and spin 1 WIMP candidates with neutrino-like couplings are given. Each WIMP is assumed to be a $p$-annihilator and the value of the annihilation cross section is chosen to $\sigma_{\mathrm{an}} = 6$ pb. The annihilation fraction $\kappa_e$ is fixed to 0.3

**p-annihilator,** $S_\chi = 1$**,** $\kappa(e^R_- e^L_+) = 0$**,** $\kappa(e^L_- e^R_+) = 4\kappa_e$

In Figure 5.12 the value of $\chi^2 - \chi^2_{\mathrm{min}}$ is displayed as a function of the hypothesised WIMP mass. For the signal a WIMP with a mass of 150 GeV is chosen. The test has been calculated for

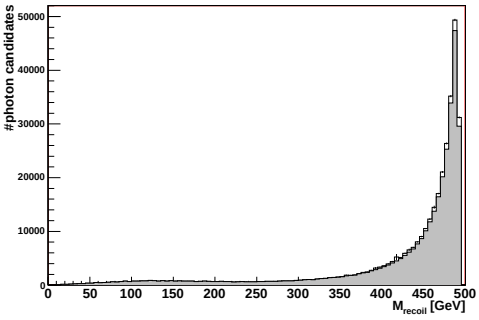


(a) Recoil mass spectrum for a 150 GeV, spin 1, $p$-annihilator WIMP with $k_e = 0.3$. The couplings are parity and helicity conserving. The beams are unpolarised. The "data" is plotted with errors, the (grey) area is the background contribution.

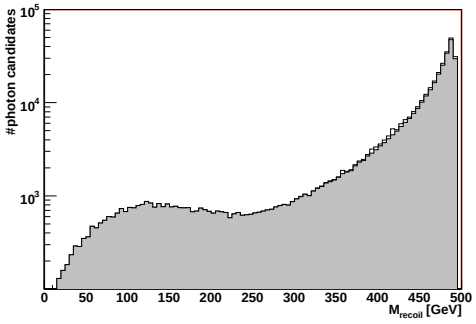


(b) Same as Fig 5.11(a), logarithmic scale.

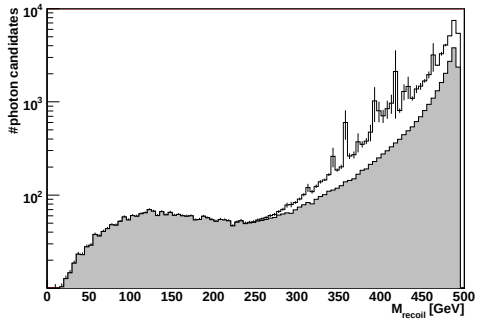


(c) Recoil mass spectrum for a 150 GeV, spin 1, $p$-annihilator WIMP with $k_e = 0.3$. The couplings are parity and helicity conserving. The beams are fully polarised. The "data" is plotted with errors, the (grey) area is the background contribution.

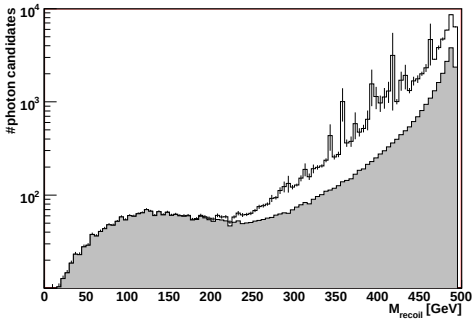


(d) Recoil mass spectrum for a 100 GeV, spin 1, $p$-annihilator WIMP with $k_e = 0.3$. The couplings are parity and helicity conserving. The beams are fully polarised. The "data" is plotted with errors, the (grey) area is the background contribution.

Figure 5.11: Input histograms for the calculation of the mass resolution.

unpolarised, partially ($P_{e^-} = 0.8; P_{e^+} = 0.0$) and fully ($P_{e^-} = 0.8; P_{e^+} = 0.6$) polarised beams. Because of the choice of the couplings, being the same as for the neutrino background, no change in the mass resolution is observed for different polarisation configurations. The horizontal line in Figure 5.12 intersects the curve at distances of one standard deviation from the minimum. The test returned as best fit $152 \pm 4$ GeV. The shift of the minimum to higher masses is due to low statistics.

**p-annihilator,** $S_\chi = \frac{1}{2}$**,** $\kappa(e^R_- e^L_+) = 0$**,** $\kappa(e^L_- e^R_+) = 4\kappa_e$

Figure 5.13 shows the mass resolution for a 150 GeV spin $\frac{1}{2}$ WIMP. The resolution for this candidate is with $158 \pm 8$ GeV by a factor of two worse than in the previous case. Again the fitted mass is higher than the signal mass. Here the shift is of the order of one standard deviation. Table 5.3 summarises the findings for the standard model like couplings.

| | $S = 1$ | $S = \frac{1}{2}$ |
|---|---|---|
| $M_\chi = 150$ GeV | | |
| $P_{e^-} = 0.0; P_{e^+} = 0.0$ | $152.1 \pm 4.0$ GeV | $157.6 \pm 8.2$ GeV |
| $P_{e^-} = 0.8; P_{e^+} = 0.0$ | $152.1 \pm 4.0$ GeV | $157.6 \pm 8.2$ GeV |
| $P_{e^-} = 0.8; P_{e^+} = 0.6$ | $152.1 \pm 4.0$ GeV | $157.6 \pm 8.2$ GeV |

Table 5.3: Mass resolution for spin 1 and $\frac{1}{2}$ WIMPs with SM charged weak interaction like couplings.

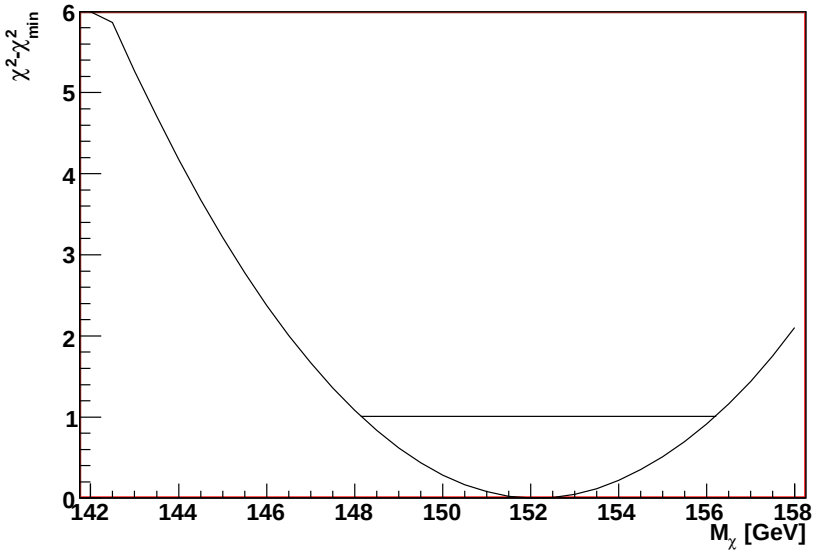


Figure 5.12: Value of the $\chi^2 - \chi^2_{\text{min}}$ test statistics as function of the fit parameter $M_\chi$. The signal is assumed to be a $p$-annihilator, 150 GeV, spin 1 WIMP. The WIMPs couple to $e^+$ and $e^-$ like SM neutrinos. The spin averaged annihilation fraction is set to 0.3. The horizontal line intersects the curve at distances of one standard deviation from the minimum.

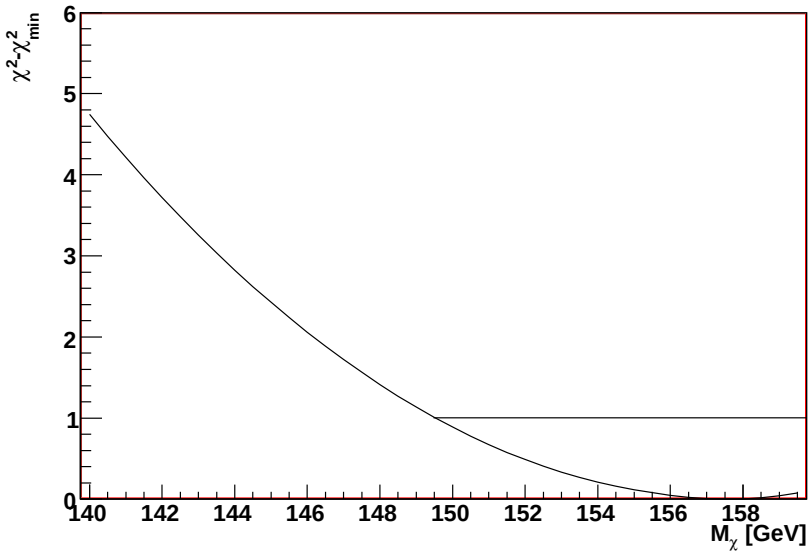


Figure 5.13: Value of the $\chi^2 - \chi^2_{\text{min}}$ test statistics as function of the fit parameter $M_\chi$. The signal is assumed to be a $p$-annihilator, 150 GeV, spin $\frac{1}{2}$ WIMP. The WIMPs couple to $e^+$ and $e^-$ like SM neutrinos. The spin averaged annihilation fraction is set to 0.3. The horizontal line intersects the curve at distances of one standard deviation from the minimum.

### 5.5.2 Helicity Conserving Couplings, Opposite to SM Charged Weak Interaction

The spin 1 and $\frac{1}{2}$ WIMPs tested for here couple to the initial leptons in the opposite way as SM neutrinos.

**p-annihilator,** $S_\chi = 1$**,** $\kappa(e^R_- e^L_+) = 0$**,** $\kappa(e^L_- e^R_+) = 4\kappa_e$

With the couplings chosen here beam polarisation increases the mass resolution. In Figures 5.14, 5.15 and 5.16 the values of the $\chi^2 - \chi^2_{\text{min}}$ test statistic are shown as a function of the fit parameter $M_\chi$ for WIMP signals with 100, 150 and 180 GeV. The solid lines are for unpolarised beams, the dotted lines for partially and the dashed lines for fully polarised beams. 80% $e^-$ polarisation enhances the mass resolution on average by a factor of $\approx 3.6$. Further enhancement with a factor of about 1.6 is obtained by additional $e^+$ polarisation. Table 5.4 lists the results.

**p-annihilator,** $S_\chi = \frac{1}{2}$**,** $\kappa(e^R_- e^L_+) = 0$**,** $\kappa(e^L_- e^R_+) = 4\kappa_e$

Figures 5.17, 5.18 and 5.19 shows the mass resolution spin $\frac{1}{2}$ WIMPs with masses of 100, 150 and 180 GeV. The line codings (solid, dotted and dashed) are the same as in the previous paragraph. In Table 5.4 the results are listed alongside the spin 1 case. The mass resolutions degrade with a factor of very roughly 1.5 compared to the calculations with spin 1 WIMPs. The influence of beam polarisation is of the same order.

| | $S = 1$ | $S = \frac{1}{2}$ |
|---|---|---|
| $M_\chi = 100$ GeV | | |
| $P_{e^-} = 0.0; P_{e^+} = 0.0$ | $103.3 \pm 4.3$ GeV | $106.2 \pm 7.7$ GeV |
| $P_{e^-} = 0.8; P_{e^+} = 0.0$ | $101.3 \pm 1.4$ GeV | $101.5 \pm 1.9$ GeV |
| $P_{e^-} = 0.8; P_{e^+} = 0.6$ | $101.0 \pm 0.9$ GeV | $101.3 \pm 1.2$ GeV |
| $M_\chi = 150$ GeV | | |
| $P_{e^-} = 0.0; P_{e^+} = 0.0$ | $152.2 \pm 4.0$ GeV | $157.5 \pm 7.9$ GeV |
| $P_{e^-} = 0.8; P_{e^+} = 0.0$ | $150.5 \pm 1.0$ GeV | $150.7 \pm 1.5$ GeV |
| $P_{e^-} = 0.8; P_{e^+} = 0.6$ | $150.3 \pm 0.6$ GeV | $150.4 \pm 0.8$ GeV |
| $M_\chi = 180$ GeV | | |
| $P_{e^-} = 0.0; P_{e^+} = 0.0$ | $181.5 \pm 3.0$ GeV | $180.6 \pm 5.6$ GeV |
| $P_{e^-} = 0.8; P_{e^+} = 0.0$ | $180.7 \pm 0.8$ GeV | $180.7 \pm 1.3$ GeV |
| $P_{e^-} = 0.8; P_{e^+} = 0.6$ | $180.5 \pm 0.5$ GeV | $180.5 \pm 0.6$ GeV |

Table 5.4: Mass resolution for spin 1 and $\frac{1}{2}$ WIMPs with couplings opposite to SM charged weak interaction.

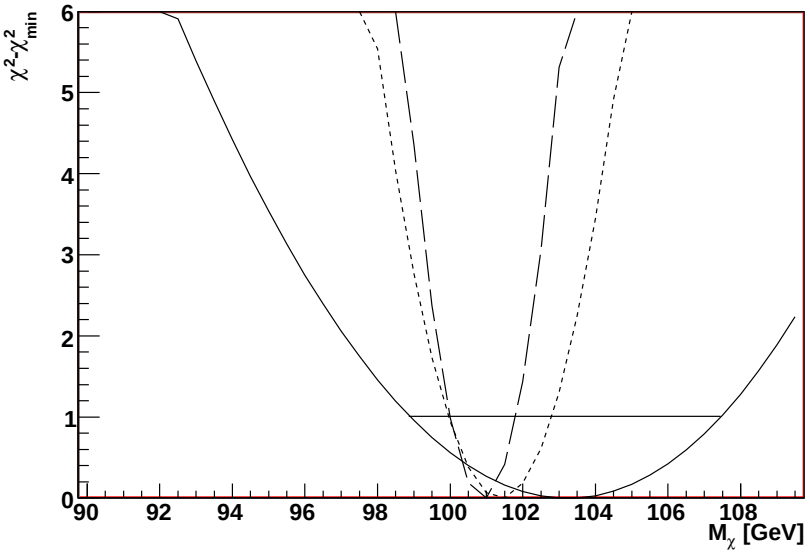


Figure 5.14: Value of the $\chi^2 - \chi^2_{\text{min}}$ test statistics as function of the fit parameter $M_\chi$. The signal is assumed to be a $p$-annihilator, 100 GeV, spin 1 WIMP. The WIMPs couple to $e^+$ and $e^-$ opposite to SM neutrinos. The spin averaged annihilation fraction is set to 0.3. The horizontal line intersects the curve at distances of one standard deviation from the minimum.

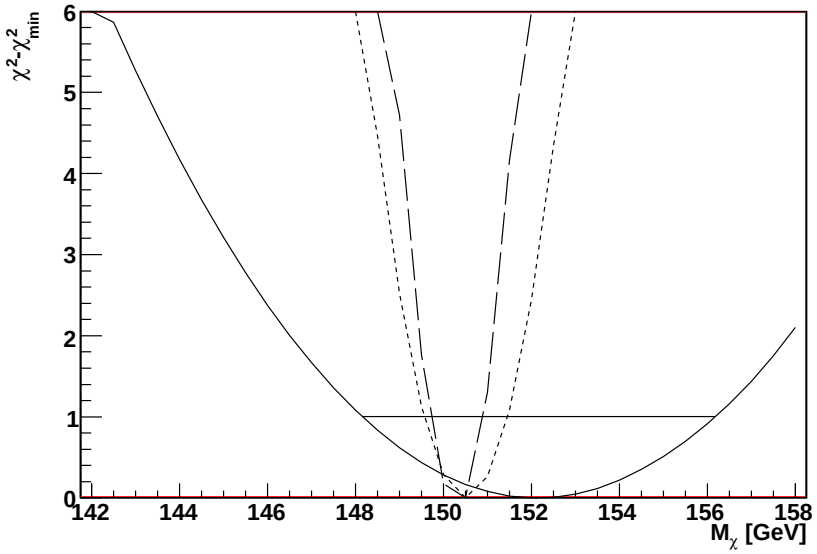


Figure 5.15: Value of the $\chi^2 - \chi^2_{\text{min}}$ test statistics as function of the fit parameter $M_\chi$. The signal is assumed to be a $p$-annihilator, 150 GeV, spin 1 WIMP. The WIMPs couple to $e^+$ and $e^-$ opposite to SM neutrinos. The spin averaged annihilation fraction is set to 0.3. The horizontal line intersects the curves at distances of one standard deviation from the minimum.

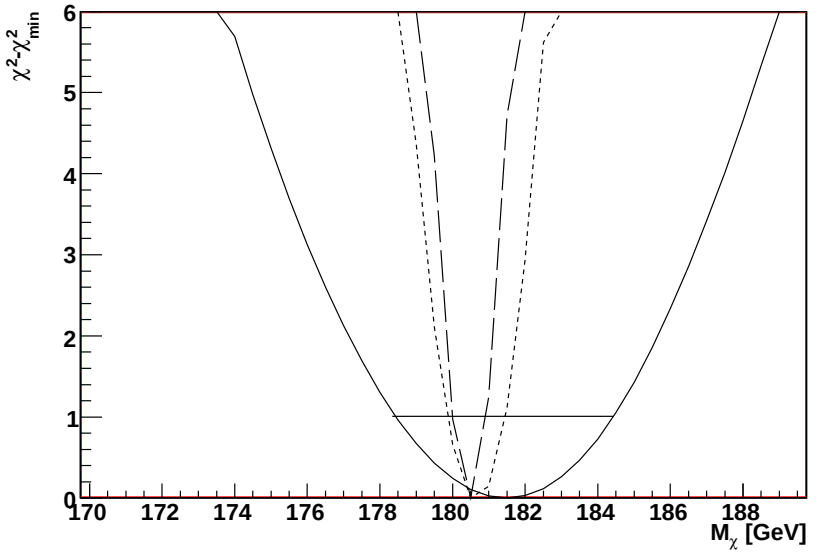


Figure 5.16: Value of the $\chi^2 - \chi^2_{\text{min}}$ test statistics as function of the fit parameter $M_\chi$. The signal is assumed to be a $p$-annihilator, 180 GeV, spin 1 WIMP. The WIMPs couple to $e^+$ and $e^-$ opposite to SM neutrinos. The spin averaged annihilation fraction is set to 0.3. The horizontal line intersects the curves at distances of one standard deviation from the minimum.

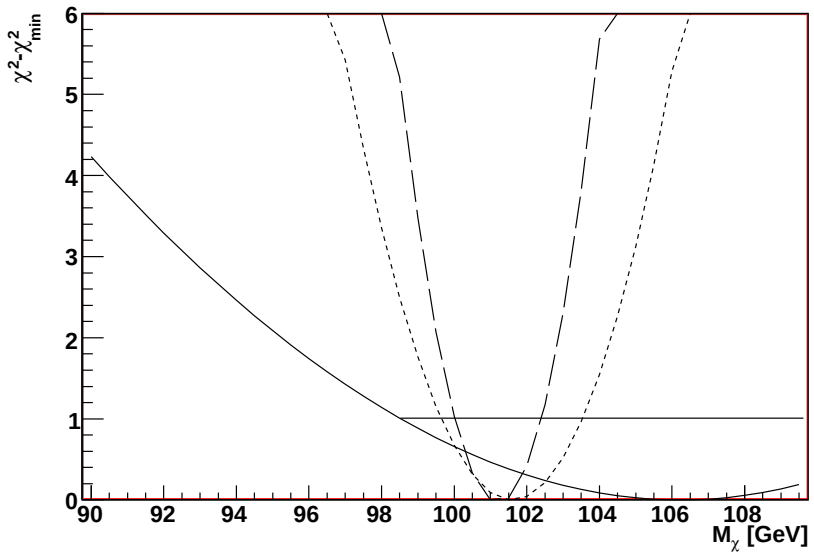


Figure 5.17: Value of the $\chi^2 - \chi^2_{\text{min}}$ test statistics as function of the fit parameter $M_\chi$. The signal is assumed to be a $p$-annihilator, 100 GeV, spin $\frac{1}{2}$ WIMP. The WIMPs couple to $e^+$ and $e^-$ opposite to SM neutrinos. The spin averaged annihilation fraction is set to 0.3. The horizontal line intersects the curves at distances of one standard deviation from the minimum.

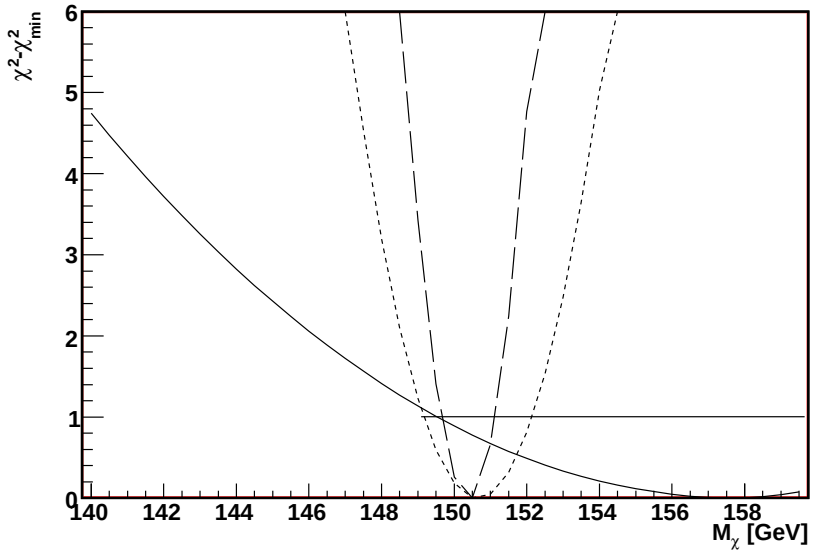


Figure 5.18: Value of the $\chi^2 - \chi^2_{\text{min}}$ test statistics as function of the fit parameter $M_\chi$. The signal is assumed to be a $p$-annihilator, 150 GeV, spin $\frac{1}{2}$ WIMP. The WIMPs couple to $e^+$ and $e^-$ opposite to SM neutrinos. The spin averaged annihilation fraction is set to 0.3. The horizontal line intersects the curves at distances of one standard deviation from the minimum.

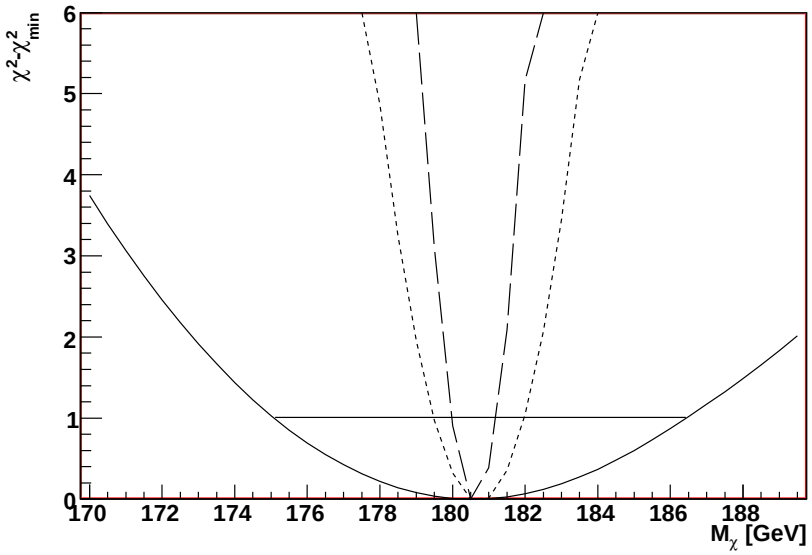


Figure 5.19: Value of the $\chi^2 - \chi^2_{\text{min}}$ test statistics as function of the fit parameter $M_\chi$. The signal is assumed to be a $p$-annihilator, 180 GeV, spin $\frac{1}{2}$ WIMP. The WIMPs couple to $e^+$ and $e^-$ opposite to SM neutrinos. The spin averaged annihilation fraction is set to 0.3. The horizontal line intersects the curves at distances of one standard deviation from the minimum.

### 5.5.3 Helicity and Parity Conserving Couplings

Finally, like for the calculation of exclusion limits helicity and parity conserving couplings are investigated.

**p-annihilator,** $S_\chi = 1$**,** $\kappa(e^R_- e^L_+) = \kappa(e^L_- e^R_+) = 2\kappa_e$

Figures 5.20, 5.21 and 5.22 give the results for spin 1 WIMPs with masses of 100, 150 and 180 GeV. The results are listed in Table 5.5 together with the results for spin $\frac{1}{2}$ WIMPs with helicity and parity conserving couplings. Overall, the achievable resolution with these couplings is slightly worse (with a factor of $\approx 1.3$) as with couplings opposite to the SM weak interaction, but is still on the percentage level.

**p-annihilator,** $S_\chi = \frac{1}{2}$**,** $\kappa(e^R_- e^L_+) = \kappa(e^L_- e^R_+) = 2\kappa_e$

The obtained mass resolutions for helicity and parity conserving WIMPs with spin $\frac{1}{2}$ are also listed in Table 5.5. Furthermore Tables 5.6 and 5.7 list all results of the tests on the mass resolution for spin 1 and $\frac{1}{2}$ separately.

In summary an 80% electron polarisation increases the mass resolution by a factor of about 4 for couplings opposite to the SM charged weak interaction, and by a factor of about 2.9 for helicity and parity conserving couplings. These numbers are averaged over all investigated masses and spins. Additional 60% positron polarisation gives factors of about 1.8 in both cases, resulting in an overall increase in resolution of about 7 (couplings opposite to SM) and 5 (helicity and

parity conserving) respectively. Resolutions for spin $\frac{1}{2}$ WIMPs decrease by factors between roughly 1.3 to 1.9 compared to spin 1 WIMPs, where the lower number is for fully polarised beams and the higher number for unpolarised beams.

| | $S = 1$ | $S = \frac{1}{2}$ |
|---|---|---|
| $M_\chi = 100$ GeV | | |
| $P_{e^-} = 0.0; P_{e^+} = 0.0$ | $103.7 \pm 4.0$ GeV | $106.3 \pm 7.7$ GeV |
| $P_{e^-} = 0.8; P_{e^+} = 0.0$ | $101.9 \pm 1.8$ GeV | $101.8 \pm 2.6$ GeV |
| $P_{e^-} = 0.8; P_{e^+} = 0.6$ | $101.4 \pm 1.1$ GeV | $101.3 \pm 1.4$ GeV |
| $M_\chi = 150$ GeV | | |
| $P_{e^-} = 0.0; P_{e^+} = 0.0$ | $152.0 \pm 4.0$ GeV | $157.2 \pm 6.9$ GeV |
| $P_{e^-} = 0.8; P_{e^+} = 0.0$ | $150.5 \pm 1.3$ GeV | $151.0 \pm 2.3$ GeV |
| $P_{e^-} = 0.8; P_{e^+} = 0.6$ | $150.4 \pm 0.7$ GeV | $150.4 \pm 1.0$ GeV |
| $M_\chi = 180$ GeV | | |
| $P_{e^-} = 0.0; P_{e^+} = 0.0$ | $181.4 \pm 3.0$ GeV | $180.7 \pm 5.7$ GeV |
| $P_{e^-} = 0.8; P_{e^+} = 0.0$ | $180.6 \pm 1.1$ GeV | $181.0 \pm 1.7$ GeV |
| $P_{e^-} = 0.8; P_{e^+} = 0.6$ | $180.5 \pm 0.6$ GeV | $180.7 \pm 0.9$ GeV |

Table 5.5: Mass resolution for spin 1 and $\frac{1}{2}$ WIMPs with helicity and parity conserving couplings.

| $S = 1$ | SM-like | Opposite to SM | Parity and helicity |
|---|---|---|---|
| $M_\chi = 100$ GeV | | | |
| $P_{e^-} = 0.0; P_{e^+} = 0.0$ | | $103.3 \pm 4.3$ GeV | $103.7 \pm 4.0$ GeV |
| $P_{e^-} = 0.8; P_{e^+} = 0.0$ | | $101.3 \pm 1.4$ GeV | $101.9 \pm 1.8$ GeV |
| $P_{e^-} = 0.8; P_{e^+} = 0.6$ | | $101.0 \pm 0.9$ GeV | $101.4 \pm 1.1$ GeV |
| $M_\chi = 150$ GeV | | | |
| $P_{e^-} = 0.0; P_{e^+} = 0.0$ | $152.1 \pm 4.0$ GeV | $152.2 \pm 4.0$ GeV | $152.0 \pm 4.0$ GeV |
| $P_{e^-} = 0.8; P_{e^+} = 0.0$ | $152.1 \pm 4.0$ GeV | $150.5 \pm 1.0$ GeV | $150.5 \pm 1.3$ GeV |
| $P_{e^-} = 0.8; P_{e^+} = 0.6$ | $152.1 \pm 4.0$ GeV | $150.3 \pm 0.6$ GeV | $150.4 \pm 0.7$ GeV |
| $M_\chi = 180$ GeV | | | |
| $P_{e^-} = 0.0; P_{e^+} = 0.0$ | | $181.5 \pm 3.0$ GeV | $181.4 \pm 3.0$ GeV |
| $P_{e^-} = 0.8; P_{e^+} = 0.0$ | | $180.7 \pm 0.8$ GeV | $180.6 \pm 1.1$ GeV |
| $P_{e^-} = 0.8; P_{e^+} = 0.6$ | | $180.0 \pm 0.5$ GeV | $180.5 \pm 0.6$ GeV |

Table 5.6: Mass Resolutions for $S = 1$ WIMPs

| $S = \frac{1}{2}$ | SM-like | Opposite to SM | Parity and helicity |
|---|---|---|---|
| $M_\chi = 100$ GeV | | | |
| $P_{e^-} = 0.0; P_{e^+} = 0.0$ | | $106.2 \pm 7.7$ GeV | $106.3 \pm 7.7$ GeV |
| $P_{e^-} = 0.8; P_{e^+} = 0.0$ | | $101.5 \pm 1.9$ GeV | $101.8 \pm 2.6$ GeV |
| $P_{e^-} = 0.8; P_{e^+} = 0.6$ | | $101.2 \pm 1.2$ GeV | $101.3 \pm 1.4$ GeV |
| $M_\chi = 150$ GeV | | | |
| $P_{e^-} = 0.0; P_{e^+} = 0.0$ | $157.6 \pm 8.1$ GeV | $157.5 \pm 7.9$ GeV | $157.2 \pm 6.9$ GeV |
| $P_{e^-} = 0.8; P_{e^+} = 0.0$ | $157.6 \pm 8.1$ GeV | $150.7 \pm 1.5$ GeV | $151.0 \pm 2.3$ GeV |
| $P_{e^-} = 0.8; P_{e^+} = 0.6$ | $157.6 \pm 8.1$ GeV | $150.4 \pm 0.8$ GeV | $150.4 \pm 1.0$ GeV |
| $M_\chi = 180$ GeV | | | |
| $P_{e^-} = 0.0; P_{e^+} = 0.0$ | | $180.6 \pm 5.6$ GeV | $180.7 \pm 5.7$ GeV |
| $P_{e^-} = 0.8; P_{e^+} = 0.0$ | | $180.7 \pm 1.3$ GeV | $181.0 \pm 1.7$ GeV |
| $P_{e^-} = 0.8; P_{e^+} = 0.6$ | | $180.5 \pm 0.6$ GeV | $180.5 \pm 0.9$ GeV |

Table 5.7: Mass Resolutions for $S = \frac{1}{2}$ WIMPs

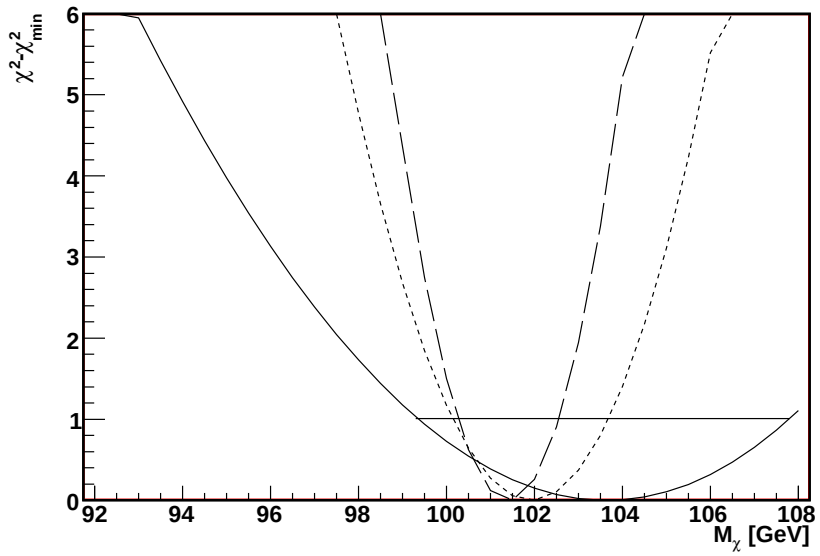


Figure 5.20: Value of the $\chi^2 - \chi^2_{\text{min}}$ test statistics as function of the fit parameter $M_\chi$. The signal is assumed to be a $p$-annihilator, 100 GeV, spin 1 WIMP. The couplings conserve helicity and parity. The spin averaged annihilation fraction is set to 0.3. The horizontal line intersects the curves at distances of one standard deviation from the minimum.

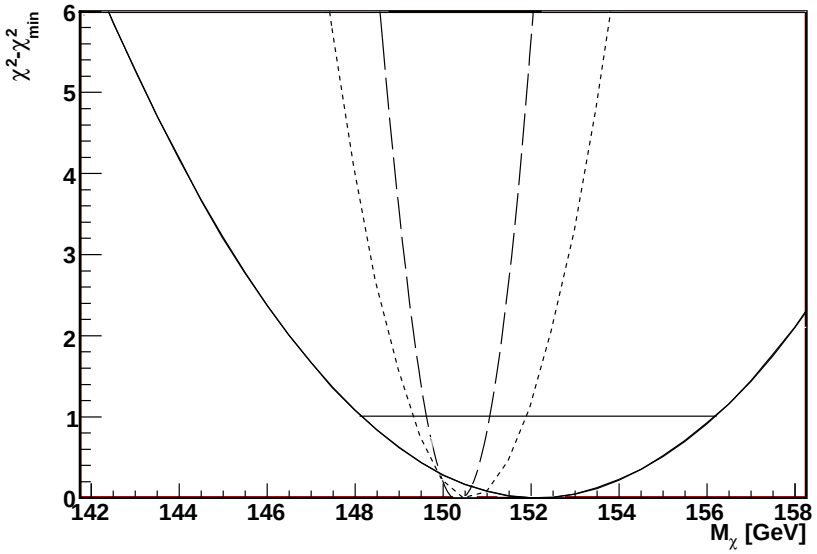


Figure 5.21: Value of the $\chi^2 - \chi^2_{\text{min}}$ test statistics as function of the fit parameter $M_\chi$. The signal is assumed to be a $p$-annihilator, 150 GeV, spin 1 WIMP. The couplings conserve helicity and parity. The spin averaged annihilation fraction is set to 0.3. The horizontal line intersects the curves at distances of one standard deviation from the minimum.

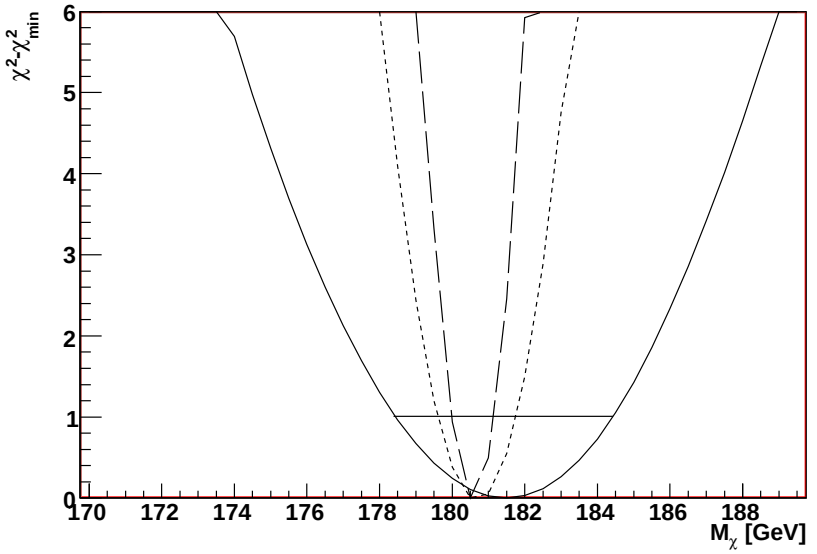


Figure 5.22: Value of the $\chi^2 - \chi^2_{\text{min}}$ test statistics as function of the fit parameter $M_\chi$. The signal is assumed to be a $p$-annihilator, 180 GeV, spin 1 WIMP. The couplings conserve helicity and parity. The spin averaged annihilation fraction is set to 0.3. The horizontal line intersects the curves at distances of one standard deviation from the minimum.

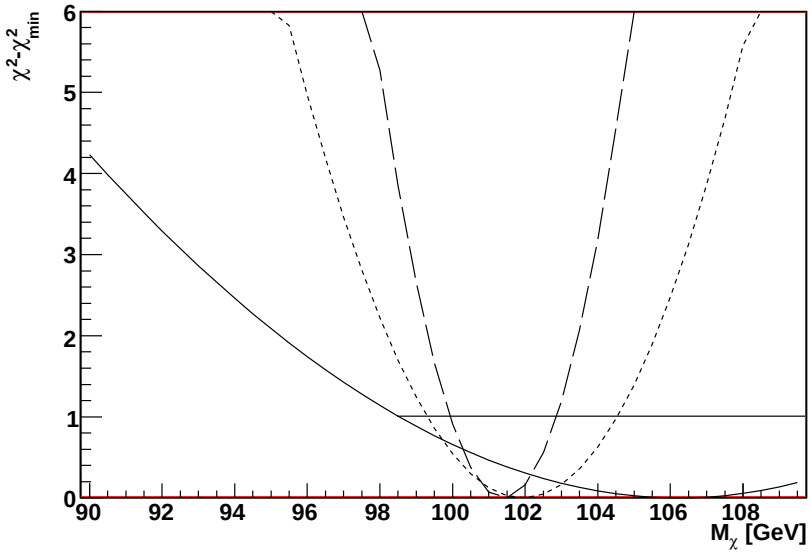


Figure 5.23: Value of the $\chi^2 - \chi^2_{\text{min}}$ test statistics as function of the fit parameter $M_\chi$. The signal is assumed to be a $p$-annihilator, 100 GeV, spin $\frac{1}{2}$ WIMP. The couplings conserve helicity and parity. The spin averaged annihilation fraction is set to 0.3. The horizontal line intersects the curves at distances of one standard deviation from the minimum.

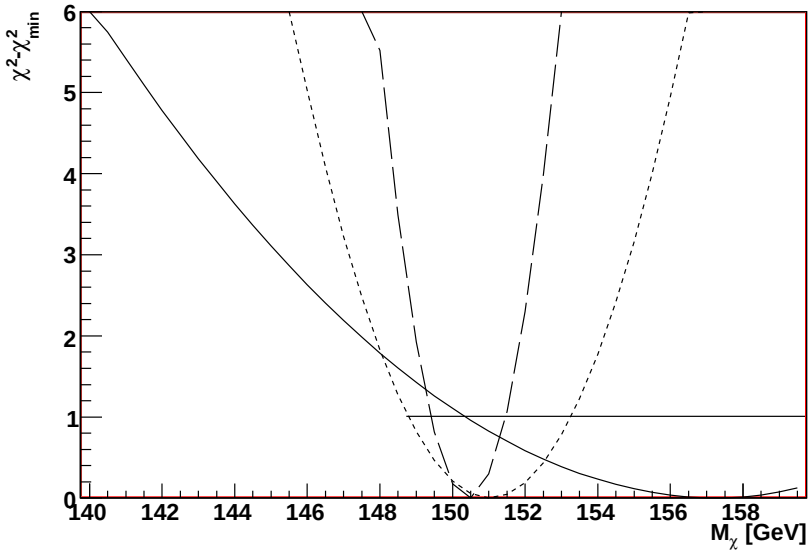


Figure 5.24: Value of the $\chi^2 - \chi^2_{\text{min}}$ test statistics as function of the fit parameter $M_\chi$. The signal is assumed to be a $p$-annihilator, 150 GeV, spin $\frac{1}{2}$ WIMP. The couplings conserve helicity and parity. The spin averaged annihilation fraction is set to 0.3. The horizontal line intersects the curves at distances of one standard deviation from the minimum.

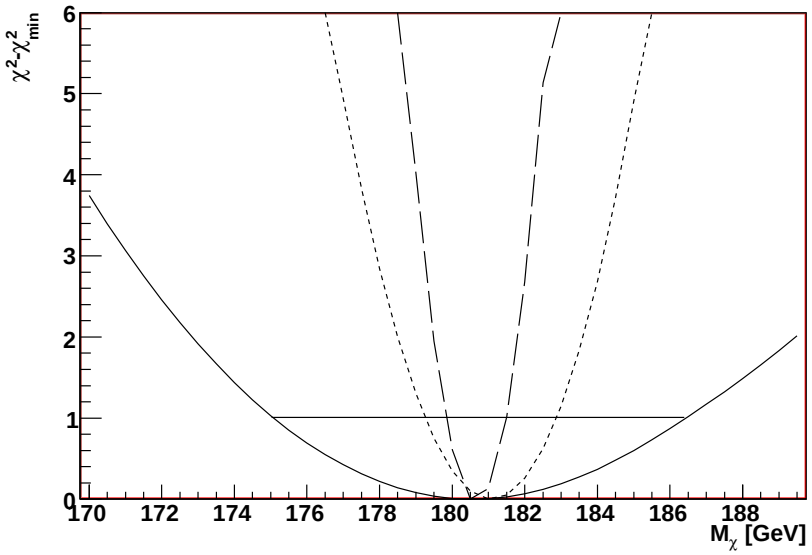


Figure 5.25: Value of the $\chi^2 - \chi^2_{\rm min}$ test statistics as function of the fit parameter $M_\chi$. The signal is assumed to be a $p$-annihilator, 180 GeV, spin $\frac{1}{2}$ WIMP. The couplings conserve helicity and parity. The spin averaged annihilation fraction is set to 0.3. The horizontal line intersects the curves at distances of one standard deviation from the minimum.

# Chapter 6

# Conclusions and Outlook

Given the validity of the model-independent WIMP production cross section of sec. 2.4, the obtained sensitivity limits of sec. 5.4 show that the annihilation fraction $\kappa_e$ can be probed down to at least 0.3 for spin 1 WIMP candidates with masses between 90 and 225 GeV and unpolarised beams. For spin $\frac{1}{2}$ WIMPs the corresponding masses lie between 120 and 215 GeV. Typical values for $\kappa_e$ in MSSM models are between 0.2 and 0.3 [13]. Thus the results presented indicate the great potential of the ILC for discovery of Dark Matter. The range of scanable values of the parameter $\kappa_e$ is even extended by a factor of about 10 when the spin 1 DM candidates couplings to the initial electrons and positrons are opposite to the SM weak interaction (sec. 5.4.2) and beam polarisation is maximal, so $P_{e^-} = 0.8$ and $P_{e^+} = 0.6$. Electron polarisation by itself provides a factor of about 4 to the lowering of observation limits. With couplings conserving parity and helicity, electron polarisation gives a factor of $\approx 2.3$ and additional positron polarisation another factor of 2.2. For spin $\frac{1}{2}$ DM candidates the impacts of beam polarisation on the sensitivity are of the same order. The absolute limits are about two times higher than for spin 1 WIMPs because of the smaller production cross section.
The masses of a potential DM candidate with spin 1 can be resolved on the percentage level to 4% for 100 GeV WIMPs and 2% for 180 GeV candidates (sec. 5.5). If beam polarisation is applied, the resolution is enhanced to the permille level by a factor up to 7 for couplings opposite to the SM and up to 5 for helicity and parity conserving couplings. If spin $\frac{1}{2}$ candidates are assumed, the resolution is with 3 to 7% for unpolarised beams 1.5 times worse than for spin 1 WIMPs. The effects of beam polarisation are however the same.
In this analysis several problems occurred during detector simulation and event reconstruction. To mention are the invalid calibration constants (sec. 4.2) and the worse than expected energy resolution of the reconstruction (sec. 4.4.4). The influences of these problems on the results presented are not evaluated in this thesis and have to be kept in mind when reviewing the analysis. Another source of irritation to the sensitivity calculation is due to the strong signal migration (sec. 5.3) that is basically a consequence of both the calibration and the energy resolution. The extend of its influence on the limits given is not scrutinised either. Finally the conclusions on the mass resolutions are rather unfirm because of the strong fluctuations in the signal recoil mass distributions, the extension to relativistic WIMPs (the relativistic cut is not applied) and the method itself, since only two event samples are compared for compatibility, rather than comparing a sample to an expectation.

Further research on model-independent DM searches with simulation studies is a promising possibility of evaluating the potential of the ILC for BSM physics. Statements on this po-

tential should be however the result of an interplay with physics studies on specific models containing DM candidates like e.g. supersymmetry. The next steps in this direction should be the improvement of the detector simulation software and reconstruction utilities, and a more thorough event simulation by using valid calibration constants. The urgent need for a deeper understanding of systematical errors is suggested by the large fluctuations observed in the input histograms to the sensitivity and mass resolution calculations. To come closer to a real life experiment the inclusion of typical backgrounds, reducible and irreducible, should be taken into account, and as a consequence a more sophisticated event selection has to be performed. One important irreducible background is the process $e^+e^- \to \nu\bar{\nu}\nu\bar{\nu}\gamma$ of section 2.5. As mentioned in the foregoing paragraph, the application of the methods used have to be revised. In addition to sensitivity limits on $\kappa_e$, limits on the cross section itself are needed to complete the picture. The sensitivity curves were calculated with $\langle CL_s \rangle_b$ (section 2.7). Although the difference to the appropriate confidence level $\langle CL_b \rangle_{sb}$ should be rather small in view of the problems encountered with the detector simulation and the unknown systematic uncertainties, this approximation has to be dropped. Another approximation to be abandoned is the scaling behaviour due to polarisation of the background. The definition of $\kappa_{\mathrm{bg}}$ should include the $Z^0$ exchange contribution in a further analysis. On the theoretical side, lifting the restraint on non-relativistic final state WIMPs seems to be an important issue.

# Bibliography


[1] F. J. Hasert *et al.*, "Observation of neutrino like interactions without muon or electron in the Gargamelle neutrino experiment", Nucl. Phys. B73 (1974) 1

[2] F. Abe *et al.*, "Observation of Top Quark Production in $\bar{p}p$ Collisions", Phys. Rev. Lett. 74 (1995) 2626-2631 , hep-ex/9503002

[3] D. Clowe *et al.*, "A direct empirical proof of of the existence of Dark Matter", ApJL 648 L109, astro-ph/0608407 v1

[4] D. S. Akerib *et al.*, "Exclusion Limits on the WIMP-Nucleon Cross-Section from the First Run of the Cryogenic Dark Matter Search in the Soudan Underground Lab", Phys. Rev. D72 (2005) 052009, astro-ph/0507190

[5] B. Ryden, "Introduction to Cosmology", Addison Wesley 2003

[6] J. C. Mather *et al.*, "Calibrator Design for the COBE Far Infrared Absolute Spectrophotometer (FIRAS)", Astrophys. J 512 511 (1999)

[7] D. N. Spergel *et al.*, "Wilkinson Microwave Anisotropy Probe (WMAP) Three Year Results: Implication for Cosmology", astro-ph/0603449 v1

[8] Particle data group, "Particle Physics Booklet, July 2006", http://pdg.lbl.gov

[9] Y. Fukuda *et al.*, The Super-Kamiokande Collaboration, "Evidence for oscillation of atmospheric neutrinos", Phys. Rev. Lett. 93:101801,2004, hep-ex/0404034

[10] U. Seljak *et al.*, "Cosmological parameters from combining the Lyman-$\alpha$ forest with CMB, galaxy clustering and SN constraints", JCAP 0610:014 (2006). astro-ph/0604335 v4

[11] P. J. Peebles "Principles of Physical Cosmology", Princton University Press 1993

[12] S. Kraml, "LHC\ILC\Cosmology Interplay", Pramana 67:597-606 (2006), hep-ph/0607270 v1

[13] A. Birkedal *et al.*, "Dark Matter at Colliders: a Model-Independent Approach", Phys. Rev. D 70:077701 (2004), hep-ph/0403004.

[14] G. Montagna *et al.*, "`NUNUGPV` - A Monte Carlo event generator for $e^+e^- \to \nu\bar{\nu}\gamma(\gamma)$ events at LEP", Comput. Phys. Commun. 98 (1996) 206-214

[15] P. Bock, "Computation of confidence levels for exclusion or discovery of a signal with the method of fractional event counting",JHEP 0701 080, hep-ex/0405072 v3

[16] http://root.cern.ch

[17] T. Junk, "Confidence Level Computation for Combining Searches with Small Statistics", Nucl. Instrum. Meth. A 434:435, hep-ex/9902006 v1

[18] G. Zech, "Einfürung in Statistik und Messwertanalyse"

[19] N. D. Gagunashvili, "Comparison of weighted and unweighted histograms", physics/0605123 v1

[20] The International Linear Collider Global Design Effort Baseline Configuration Document, Nov. 5 2006

[21] "TESLA Technical Design Report Part II The Accelerator, March 2001"

[22] P. Cheo, "Disruption effects from the interaction of round $e^+e^-$ beams", Phys. Rev. D38:987 (1988)

[23] Detector Outline Document For The Large Detector Concept, July 2006

[24] http://geant4.web.cern.ch/geant4

[25] http://polywww.in2p3.fr/activites/physique/geant4/tesla/www/mokka/mokka.html

[26] http://lcg.web.cern.ch/LCG

[27] MarlinReco, http://ilcsoft.desy.de/marlin

[28] A. Raspereza, "Clustering Algorithm for Highly Granular Calorimeter", Talk at International Linear Collider Workshop, Snowmass Colorado, August 2005

# List of Figures

# List of Tables

# Acknowledgements

I would like to express my gratitude to Dr. Jenny List for giving me the opportunity to work in this interesting field and her very good mentoring during the last year. Furthermore I want to thank Dr. Vasiliy Morgunov, Predrag Krstonosic and Andreas Imhof for their kind help and detailed explanations, whenever I had a question.
I wish to specially thank my parents and grandparents for their constant support during the past years.

# Erklärung

Hiermit versichere ich, dass ich die vorliegende Arbeit selbstständig und nur unter Verwendung der angegebenen Quellen und Hilfsmittel angefertigt habe. Nach der Begutachtung verbleibt ein Exemplar der vorliegenden Arbeit in der Bibliothek. Mit der zukünftigen Ausleihe der Diplomarbeit bin ich einverstanden.

Hamburg, 28. Februar 2007

Christoph Bartels